AD-A037 354 ILLINOIS UNIV AT URBANA-CHAMPAIGN CHARGED PARTICLE RE--ETC F/G 20/9
X-RAY EMISSION FROM THE INTERACTION OF A MACROSCOPIC PARTICLE W--ETC(U)
OCT 76 K F YEUNG, C D HENDRICKS AF-AFOSR-2643-74
UNCLASSIFIED CPRL-1-76 AFOSR-TR-77-0130 NL

1 OF 2
AD A037354

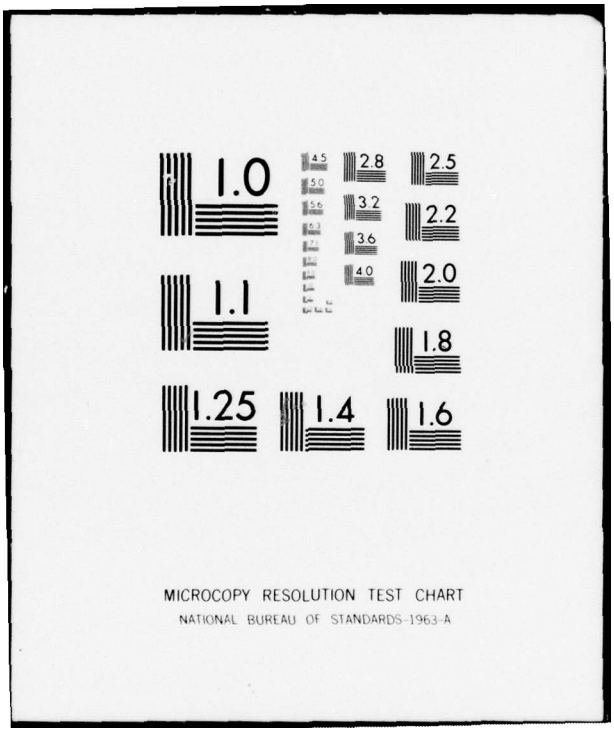
1.0
1.1
1.25
1.4
1.6
1.8
2.0
2.2
2.5
2.8
3.2
3.6
4.0
4.5
5.0
5.6
MICROCOPY RESOLUTION TEST CHART
NATIONAL BUREAU OF STANDARDS-1963-A

AFOSR ~~Interim~~ Final Report - Part II

CHARGED PARTICLE LABORATORY REPORT NO. 1-76

X-RAY EMISSION FROM THE INTERACTION OF A MACROSCOPIC PARTICLE WITH A DENSE PLASMA FOCUS

BY

KAM FOOK YEUNG

CHARLES D. HENDRICKS

CHARGED PARTICLE RESEARCH LABORATORY
DEPARTMENT OF ELECTRICAL ENGINEERING
UNIVERSITY OF ILLINOIS
URBANA, ILLINOIS 61801

~~Contract No. AFOSR-73-2481~~
~~Project Task No. 9752-01~~
AFOSR-74-2643
Project Task No. 9751-03

October 1976

Distribution Statement

"Approved for public release; distribution unlimited."

Research Sponsored By

THE AIR FORCE OFFICE OF SCIENTIFIC RESEARCH
OFFICE OF AEROSPACE RESEARCH
UNITED STATES AIR FORCE

Qualified requestors may obtain additional copies from the Defense Documentation Center. All others should apply to the Clearinghouse for Federal Scientific and Technical Information.

AIR FORCE OFFICE OF SCIENTIFIC RESEARCH (AFSC)
NOTICE OF TRANSMITTAL TO DDC
This technical report has been reviewed and is approved for public release IAW AFR 190-12 (7b).
Distribution is unlimited.
A. D. BLOSE
Technical Information Officer

UNCLASSIFIED

SECURITY CLASSIFICATION OF THIS PAGE (When Data Entered)

REPORT DOCUMENTATION PAGE	READ INSTRUCTIONS BEFORE COMPLETING FORM
1. REPORT NUMBER (18) AFOSR - TR - 77 - 0130 (19)	2. GOVT ACCESSION NO. (9)	3. RECIPIENT'S CATALOG NUMBER Final rept.
4. TITLE (and Subtitle) (6) X-RAY EMISSION FROM THE INTERACTION OF A MACROSCOPIC PARTICLE WITH A DENSE PLASMA FOCUS.	5. TYPE OF REPORT & PERIOD COVERED FINAL - Part II
	6. PERFORMING ORG. REPORT NUMBER (14) CPRL-1-76, UILU-ENG-76-2556
7. AUTHOR(s) (10) Kam Fook Yeung, Charles D. Hendricks	8. CONTRACT OR GRANT NUMBER(s) AFOSR-74-2643
9. PERFORMING ORGANIZATION NAME AND ADDRESS University of Illinois-Dept. of Electrical Eng. Charged Particle Laboratory Urbana, Illinois	10. PROGRAM ELEMENT, PROJECT, TASK & WORK UNIT NUMBERS 61102F 9751-03
11. CONTROLLING OFFICE NAME AND ADDRESS AF Office of Scientific Research /NP Bolling AFB DC 20332 (11)	12. REPORT DATE October 1976
	13. NUMBER OF PAGES 149
14. MONITORING AGENCY NAME & ADDRESS (if different from Controlling Office) (12) 147 p.	15. SECURITY CLASS. (of this report) UNCLASSIFIED
	15a. DECLASSIFICATION/DOWNGRADING SCHEDULE

16. DISTRIBUTION STATEMENT (of this Report)

Approved for public release; distribution unlimited.

(15) AF-AFOSR-2643-74

17. DISTRIBUTION STATEMENT (of the abstract entered in Block 20, if different from Report)

(16) 9751 (17) 03

18. SUPPLEMENTARY NOTES

19. KEY WORDS (Continue on reverse side if necessary and identify by block number)

Plasma Particle Interaction
Dense Plasma Focus
X-ray

20. ABSTRACT (Continue on reverse side if necessary and identify by block number)

Recently the interest in dense plasma focus has greatly increased because of the possibility of developing the device into an intense, pulsed radiation source of X-rays and neutrons for test purposes. Various experimenters have tried to scale up their radiation intensities by using large capacitor banks. Yet experimental results show that besides the engineering problems associated with the machine as the bank voltage or capacitance goes up, the intensity cannot be scaled up indefinitely by increasing the bank energy. This work proposed a new,

DD FORM 1 JAN 73 1473 EDITION OF 1 NOV 65 IS OBSOLETE

UNCLASSIFIED

SECURITY CLASSIFICATION OF THIS PAGE (When Data Entered)

079620

20. alternative way to enhance the X-ray radiation by using a macroscopic particle to interact with a plasma focus.

A theoretical study was carried out to predict the relative amount of X-ray increase when a macroscopic particle was placed in the focus region. Two assumptions were made in this study: the particle essentially had the same physical dimensions throughout the lifetime of the focus because of enormous hydrodynamic pressure compressing any ablated neutral cloud onto the particle; and the electrons were thermalized to assume a Maxwellian distribution. Most of the X-ray radiation from a focus was due to the electron bombardment of the anode surface and was accounted for by the thick target Bremsstrahlung theory. According to this theory, the X-ray emission was proportional to the first power of the atomic number, Z, of the target material, but not to the square of Z as in the thermal Bremsstrahlung case. The percentage of X-ray enhancement expected was calculated for various particle materials and sizes.

An experiment was carried out to test this new approach. A dense plasma focus device was designed and built. However, because of budgetary and time limitations the device was not optimized as predicted by theoretical studies of electrical parameters. The capacitor bank did not deliver the maximum available current because of the limitation of the system's ringing frequency. The large inductance associated with the capacitors was critical to the current rise-time. In addition, transmission line and high voltage switch inductances proved to be limiting factors on current risetime and circuit ringing frequency. Yet the 400×10^3 ampere current at 19 kV was high enough to produce the plasma focus in the pressure range between 0.5 torr to 2 torr. The electron temperature of the focus is estimated to be 1.15 ± 0.3 keV by measuring the X-ray emissions through beryllium foils of different thicknesses. This value is in good agreement with that of other focus experiments.

The results of this work show that the total X-ray emission from this dense plasma focus is not enhanced by placing a macroscopic particle in the focus region. Based on the thick target Bremsstrahlung theory, theoretical study predicts the possibility of X-ray enhancement by such an arrangement. However, experimental results show no change in the total X-ray emissions from such plasma-particle interaction. An explanation is the low energy bank employed in this experiment, only 7.85 kJ at 19 kV. Not enough high energy electrons were generated by this small amount of energy. This "starvation" phenomenon provided no extra high energy electrons to bombard the additional target area. If a higher energy capacitor bank, and a higher ringing frequency system were used, more energetic electrons would be produced and enhancement of X-ray emissions due to focus-particle interaction should be observed.

UILU-ENG-76-2556

X-RAY EMISSION FROM THE INTERACTION OF A MACROSCOPIC PARTICLE WITH A DENSE PLASMA FOCUS

Final ~~Interim~~ Report – Part II

October 1976

~~Contract No. AFOSR-73-2481~~
~~Project Task No. 9752-01~~
AFOSR-74-2643
Project Task No. 9751-03

Submitted by

Kam Fook Yeung
Charles D. Hendricks
Charged Particle Laboratory
University of Illinois
Urbana, Illinois

ABSTRACT

Recently the interest in dense plasma focus has greatly increased because of the possibility of developing the device into an intense, pulsed radiation source of X-rays and neutrons for test purposes. Various experimenters have tried to scale up their radiation intensities by using large capacitor banks. Yet experimental results show that besides the engineering problems associated with the machine as the bank voltage or capacitance goes up, the intensity cannot be scaled up indefinitely by increasing the bank energy. This work proposed a new, alternative way to enhance the X-ray radiation by using a macroscopic particle to interact with a plasma focus.

A theoretical study was carried out to predict the relative amount of X-ray increase when a macroscopic particle was placed in the focus region. Two assumptions were made in this study: the particle essentially had the same physical dimensions throughout the lifetime of the focus because of enormous hydrodynamic pressure compressing any ablated neutral cloud onto the particle; and the electrons were thermalized to assume a Maxwellian distribution. Most of the X-ray radiation from a focus was due to the electron bombardment of the anode surface and was accounted for by the thick-target Bremsstrahlung theory. According to this theory, the X-ray emission was proportional to the first power of the atomic number, Z, of the target material, but not to the square of Z as in the thermal Bremsstrahlung case. The percentage of X-ray enhancement expected was calculated for various particle materials and sizes.

An experiment was carried out to test this new approach. A dense plasma focus device was designed and built. However, because of budgetary and time limitations the device was not optimized as predicted by theoretical studies of electrical parameters. The capacitor bank did not deliver the maximum available current because of the limitation of the system's ringing frequency. The large inductance associated with the capacitors was critical to the current risetime. In addition, transmission line and high voltage switch inductances proved to be limiting factors on current risetime and circuit ringing frequency. Yet the 400×10^3 A current at 19 kV was high enough to produce the plasma focus in a pressure range between 0.5 torr to 2 torr.

The electron temperature of the focus is estimated to be 1.15 ± 0.3 keV by measuring the X-ray emissions through beryllium foils of different thicknesses. This value is in good agreement with that of other focus experiments.

The results of this work show that the total X-ray emission from this dense plasma focus is not enhanced by placing a macroscopic particle in the focus region. Based on the thick target Bremsstrahlung theory, theoretical study predicts the possibility of X-ray enhancement by such an arrangement. However experimental results show no change in the total X-ray emissions from such plasma-particle interaction. An explanation is the low energy bank employed in this experiment, only 7.85 kJ at 19 kV. Not enough high-energy electrons were generated by this small amount of energy. This "starvation" phenomenon provided no extra high-energy electrons to bombard the additional target area. If a higher energy capacitor bank, and a higher ringing frequency system were used, more energetic electrons would be produced and enhancement of X-ray emissions due to focus-particle interaction should be observed.

ACKNOWLEDGEMENT

The research was supported by the Air Force Office of Scientific Research under Grants AFOSR 73-2481 and AFOSR 74-2643.

TABLE OF CONTENTS

Page

LIST OF FIGURES

LIST OF TABLES

1. INTRODUCTION

Since the success in exploding the hydrogen bomb in the fifties, scientists had hoped to tap nuclear energy through nuclear fusion in magnetic plasma containment systems. This early enthusiasm was first carried out in Project Sherwood. At the same time, dense plasma focus experiments (DPF) were also initiated by Mather [1], [2] in the United States and by Filippov [3], [4] in Russia as part of the controlled thermonuclear fusion program.

The interest in the dense plasma focus has increased rapidly in recent years because of the success in the overall fusion research. In Fig. 1.1, the electron densities and temperatures of various natural and laboratory plasmas are compared [5]. The plasma focus has a much higher density and temperature (density = $10^{19}/cm^3$; electron temperature = 10^7 °K) than other laboratory plasmas. In Table 1.1, the experimental parameters of various fusion machines are listed. At present, the plasma focus device has the highest value for the product of plasma density (n) and confinement time (τ), $n\tau = 5 \times 10^{12}$. This value is much closer to the Lawson's criterion ($n\tau = 10^{14}$ at a temperature of 10^8 °K for breakeven condition) than the other machines. However, as a pulsed device of relatively short life (confinement time is 100 ns), research results show that it is very unlikely for the focus device to achieve Lawson's criterion. Yet because of the simplicity of the machine and its low cost, as compared to the rest of the fusion machines, the focus device has been able to draw fusion researchers' attention to its unique characteristics.

Even though the plasma focus device is not likely to be the machine for future energy production, the focus research is carried out in the hope of developing it as a pulsed radiation source. When deuterium or

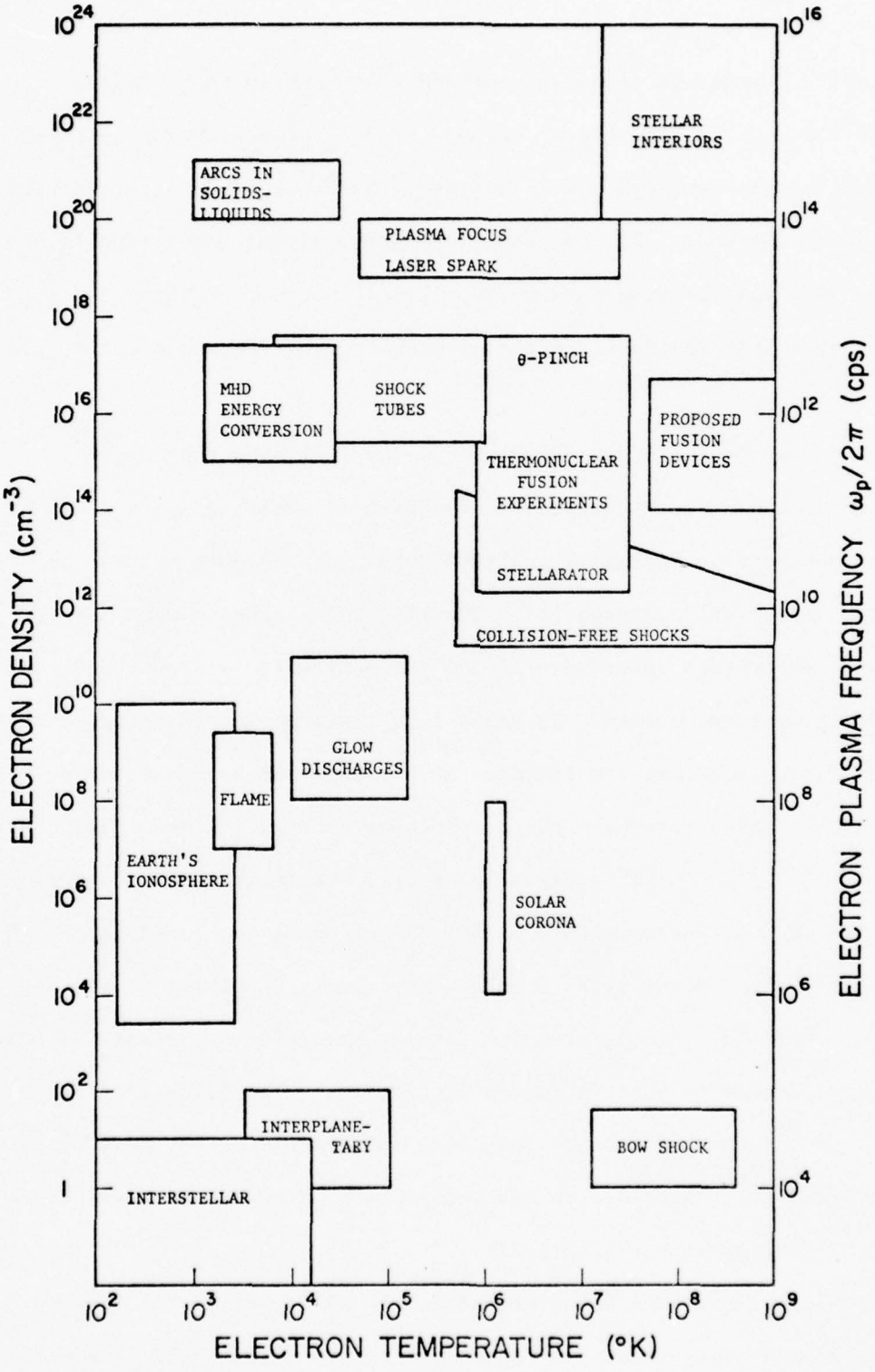

Fig. 1.1. Electron density and temperature diagram for natural and laboratory plasmas.

TABLE 1.1.

EXPERIMENTAL PARAMETERS OF FUSION DEVICES

Device	Density n ($particles/cm^3$)	Confinement Time τ(sec)	Ion Temperature T(keV)	$n\tau$
Tokamak	1.8×10^{13}	0.01 - 0.02	0.5	3.6×10^{11}
Baseball II	2.5×10^{9}	0.2 - 4.0	2	10^{10}
2X	5×10^{13}	0.0005	6 to 8	2.5×10^{10}
θ-pinch	3×10^{16}	3×10^{-6}	0.3	10^{11}
Plasma Focus	5×10^{19}	10^{-7}	6 to 8	5×10^{12}

tritium gas is used in the focus experiment, neutrons (as high as 10^{11} per discharge) as well as X-rays are produced. A substantial fraction of this X-ray energy is concentrated in the 5 - 100 keV range which thus provides an efficient soft X-ray source for a variety of applications, including the calibration of rocket spectrographs and other electronic instrumentation. The machine also produces high-energy electrons and ions many times the charging voltage of the capacitor bank of the machine, thus providing a burst of energetic ions and electrons. With these X-rays, neutrons, electrons and ions, this device provides a realistic environment similar to that of other fusion reactors. This machine is considered as a device for testing the structural materials used for controlled thermonuclear fusion or laser-fusion reactors. The great interest in dense plasma focus research is further evidenced by the recent proposals of building megajoule devices at Lawrence Livermore Laboratory by ERDA and at Frascati in Europe by Euratom.

Mather's [2] experimental results show that the intensity of the radiation output from a DPF cannot be scaled up indefinitely by increasing the bank energy. Aside from the cost factor, the engineering problems of high voltage, energy storage, and switching that are associated with this pulsed device have no simple solutions as the bank energy increases. Scientists at the megajoule facility at Livermore [6] are looking into the possibility of using laser-triggered solid-state devices to switch the ten million ampere current and the cost is estimated in the neighborhood of two million dollars. In view of these engineering and financial factors, an alternative way is explored to increase the radiation output of the existing devices without scaling up their energies.

The interaction of solid particles with a hot fusion plasma is a central process both to the fusion torch concept [7] and to refueling a fusion reactor by injecting fuel pellets during operation [8]-[10]. In both cases, there has been concern about the lifetime of the solid pellets in the hot plasma. The vaporization and ionization of the pellets in the plasma have been studied.

In a dense plasma focus, the X-ray emission consists primarily of Bremsstrahlung from the free-free charged particle interaction and the radiation from the bombardment of the anode surface by energetic electrons. The latter part of the radiation is believed to be the result of a beam-target interaction. Based on this theory, a macroscopic particle placed in the focus region may provide additional target areas for X-ray production.

The research reported in this dissertation consists of the engineering design of a dense plasma focus device and an investigation of the possibility of enhancing X-ray radiation by the interaction of the high-temperature ions and electrons in a dense plasma focus with macroscopic particles placed in the focus. Both analytical and experimental results are presented.

2. DENSE PLASMA FOCUS THEORY

In the last decade, a number of articles [11]-[17] reported experimental results from dense plasma focus devices. Attempts [18]-[20] were made to set up a theoretical model to explain the physical principles governing the process. Because of the complexity of the problem, due to the coupling of shock wave theory and plasma dynamics, the basic physics of a dense plasma focus is not well-understood and no theoretical model has been successful in providing a complete interpretation of the experimental results. However, it is generally agreed by all investigators that certain physical processes do take place in the formation of a dense plasma focus.

2.1 Basic Physical Processes

A schematic diagram of a dense plasma focus device is shown in Fig. 2.1. A pair of coaxial cylinders separated by a dielectric spacer forms the plasma gun. Hydrogen gas at a pressure of several torr fills the glass chamber. A capacitor bank is charged to supply the energy for developing the shock wave and a high-voltage, high-power switch is used to apply the high voltage to the plasma gun.

The development of a dense plasma focus can be divided into three stages:

(a) Breakdown Stage

After the high voltage of the capacitor bank is applied to the coaxial electrodes of the plasma gun, within fractions of a microsecond, gas breakdown occurs from the center positive anode to the outside cathode along the dielectric insulator. The initial gas breakdown across the insulator and the development of the current sheath are not well-understood.

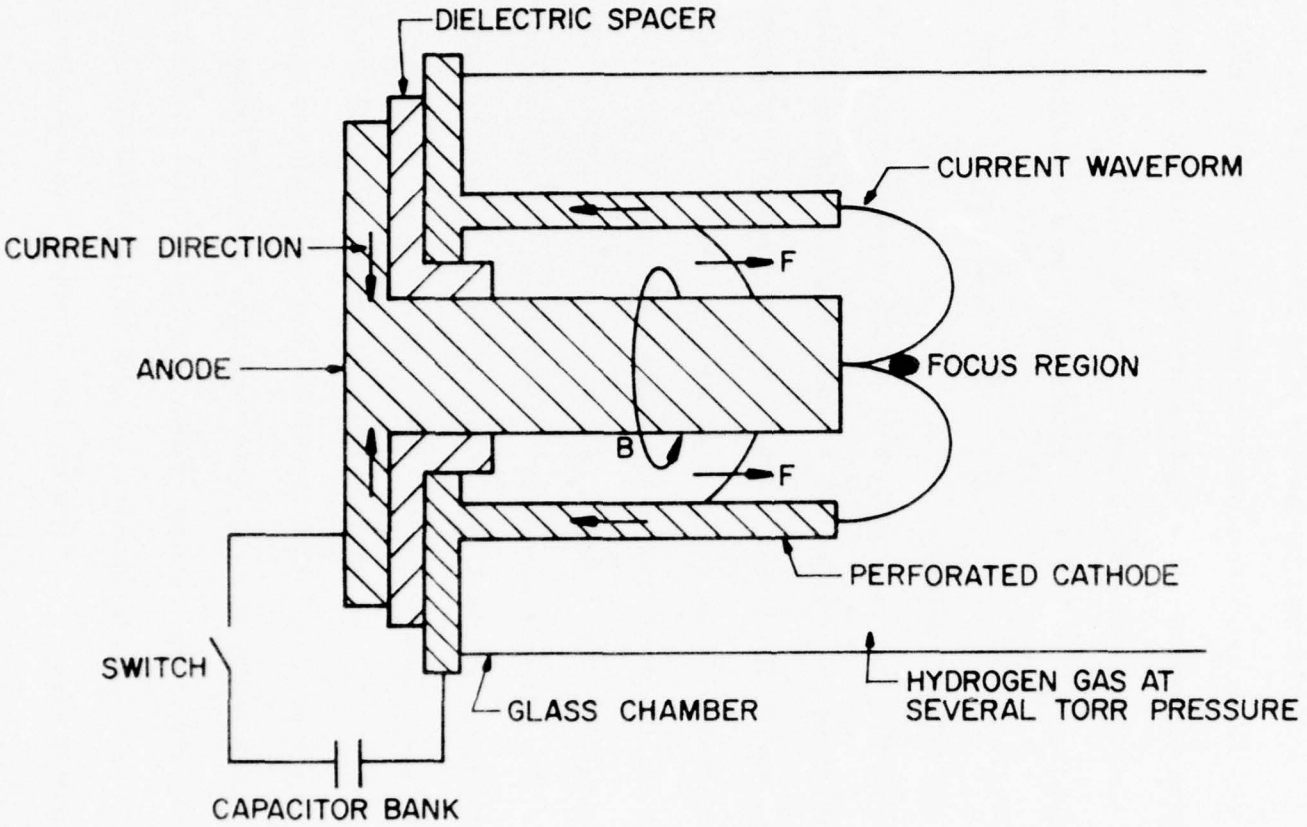

Fig. 2.1. Schematic diagram of a dense plasma focus device.

However, it is known that the success of the breakdown and the development of the current sheath depend very much on the geometry of the dielectric spacer. The initial current front shape is prescribed by the insulator. The shape is parabolic and its motion is an inverse pinch because the $(\vec{J} \times \vec{B})_r$ body force is exerted outward from the center electrode surface to the plasma current sheath. In this inverse pinch, the B_θ magnetic lines are convex and hence the pinch process is stable. This stage takes a period between 0.8 to 1.2 μsec depending on the gas loading and the applied electric field.

(b) Acceleration Stage

As shown in Fig. 2.1, the current sheath across the space between the two electrodes is not planar, but slanted backward from the anode to the cathode because of the radial dependence of the magnetic pressure gradient. The acceleration force on the current sheath is $\vec{J} \times \vec{B}$ contributing both radial and axial accelerations. The radial component of this force is outward pressing the current sheath against the inner surface of the outer electrode. The axial force component depends on $1/r^2$ across the annulus thus resulting in a higher current sheath velocity near the surface of the center electrode. The perforated outer electrode allows some of the plasma gas to escape so as to prevent any plasma pileup at the outer electrode surface. Any such accumulation may slow down the current sheath.

Rosenbluth and Garwin [13] developed the "snowplow" model to account for the velocity of the current sheath in a dynamically pinched plasma. As shown in Fig. 2.2, the current is confined in a thin sheath of thickness δ at the plasma edge. The magnetic flux strength just outside the sheath of radius r, carrying a current I, is

$$B_\theta = \frac{\mu_0 I}{2\pi r} \quad .$$

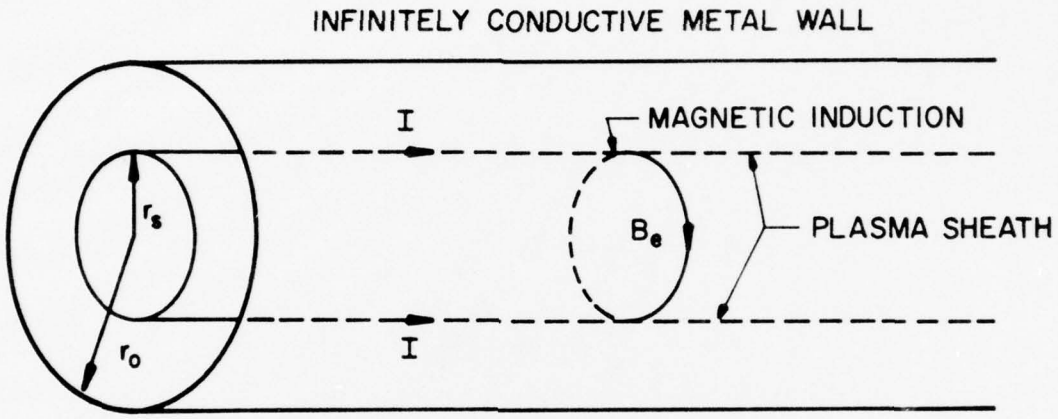

Fig. 2.2. Model of perfectly conducting pinched plasma.

The magnetic pressure is

$$p = \frac{B_\theta^2}{2\mu_0} = \frac{\mu_0 I^2}{8\pi^2 r^2} \quad . \tag{2.1}$$

The inductance of the cylindrical plasma column is

$$L = \left(\frac{\mu_0}{2\pi}\right) \ln\left(\frac{r_0}{r_s}\right) \text{ H/m} \quad . \tag{2.2}$$

Since the applied voltage between the ends of the cylindrical plasma is

$$V = -\frac{\partial}{\partial t}(LI)$$

$$V = -\frac{\partial}{\partial t}\left[\frac{\mu_0 I}{2\pi} \ln\left(\frac{r_0}{r_s}\right)\right] \quad . \tag{2.3}$$

For a perfectly conducting plasma, the material "plowed" up by the imploding surface is compressed into a thin layer at the surface r_s and the material inside r_s is not affected. Hence, equating the rate of change of momentum with the magnetic pressure, Newton's second law gives

$$\frac{d}{dt}\left[\pi\rho_0\left(r_0^2 - r_s^2\right)\frac{dr_s}{dt}\right] = -2\pi r_s\left(\frac{B_\theta^2}{2\mu_0}\right) \tag{2.4}$$

where ρ_0 = initial mass density of the gas.

From Eqs. (2.1) and (2.3) integrated with time, and by substitution, Eq. (2.4) becomes

$$\frac{d}{dt}\left[\left(r_0^2 - r_s^2\right)\frac{dr_s}{dt}\right] = -\frac{\left(\int_0^t V dt\right)^2}{\mu_0\rho_0 r_s\left[\ln\left(\frac{r_0}{r_s}\right)\right]^2} \quad . \tag{2.5}$$

Define the dimensionless variables

$$K = \frac{r_s}{r_0} \text{ and } \tau = \left(\frac{V^2}{\mu_0 \rho_0}\right)^{1/4} t \quad .$$

Equation (2.5) is reduced to

$$\frac{d}{d\tau}\left[(1 - K^2)\frac{dK}{d\tau}\right] = -\frac{K}{(\ln K)^2} \quad . \tag{2.6}$$

Numerical solution of Eq. (2.6) shows that

$$\frac{dr_s}{dt} \propto \left(\frac{V^2}{\rho_0}\right)^{1/4} \quad . \tag{2.7}$$

This solution shows that the implosion velocity of the current sheath depends on the applied voltage and the initial gas pressure in the chamber. A more exact form of the solution should be

$$v_s = \frac{dr_s}{dt} = \left(\frac{E^2}{\mu_0 \rho_0}\right)^{1/4} \tag{2.8}$$

where E = electric field applied across the electrodes.

For a plasma gun of length ℓ, the time of arrival of the current sheath at the end of the gun can be approximated as

$$t_p = \frac{\ell}{v_s} = \ell \Big/ \left(\frac{E^2}{\mu_0 \rho_0}\right)^{1/4} \quad . \tag{2.9}$$

This pinch time, t_p, is the time to the current singularity. Mather [11] compared his experimental results with Rosenbluth's theory as shown in Fig. 2.3a and b.

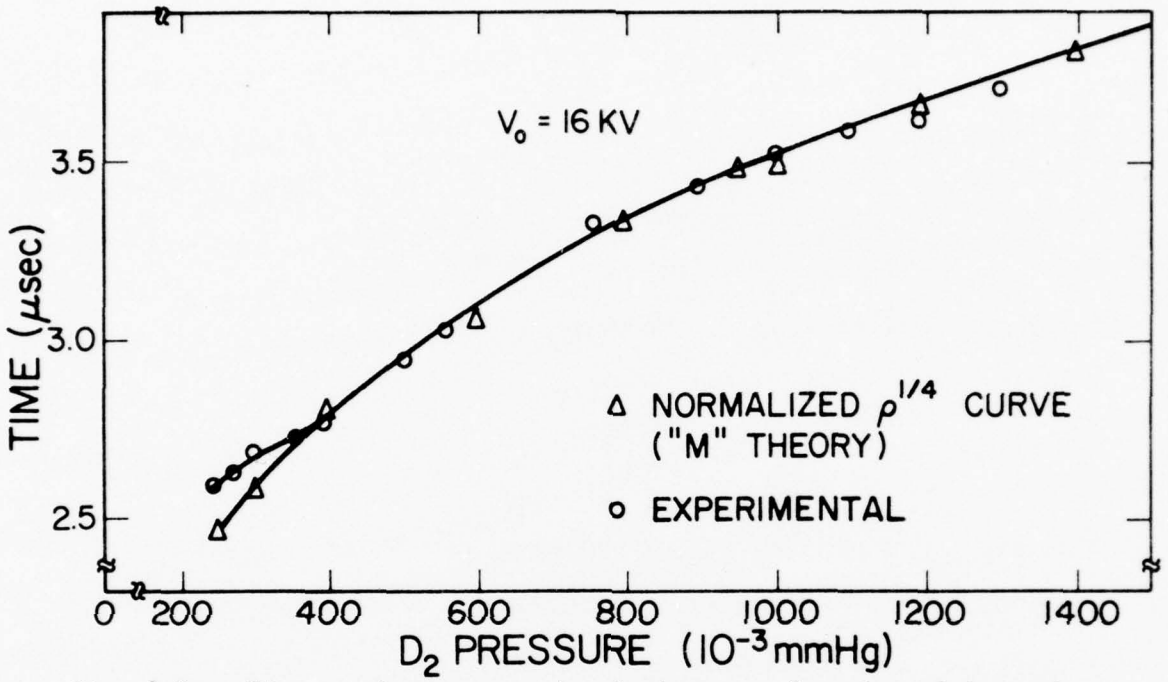

Fig. 2.3a. Time to the current singularity as a function of deuterium pressure (voltage constant).

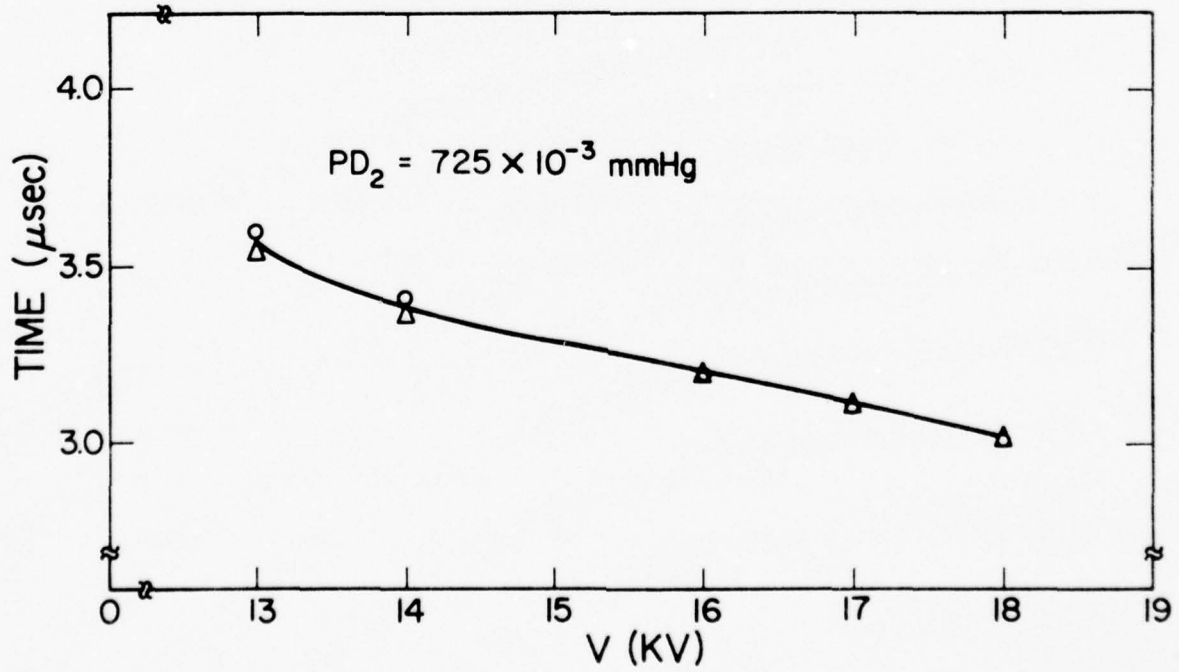

Fig. 2.3b. Time to the current singularity as a function of applied voltage (pressure constant).

(c) Collapse Stage

When the current sheath arrives at the end of the center electrode, the axisymmetric current wave collapses converting the stored magnetic energy to plasma energy in the focus region. The two dimensional r, z convergence is due to the $\vec{J} \times \vec{B}$ pinch force. At this stage, the pinching process is now a normal pinch which is opposite to the previous inverse pinch in the acceleration stage, Fig. 2.4. The plasma is compressed to high temperature and heated additionally by the hydromagnetic oscillations of the plasma column. At this stage, equilibrium no longer exists along the axis and the plasma escapes axially in either direction. Because of the shape of the convergence of the wavefront, much of the gas swept by the sheath during collapse is ejected downstream. Filippov [14] estimated that only 10 percent of the original gas is trapped in the focus region. The implosion velocity of the current sheath is estimated at $\sim 10^7$ cm/sec. This shock wave impacts the same velocity to both ions and electrons and, thus, the ions are preferentially heated because of the mass difference between electrons and ions. Hence, most of the plasma energy is in the form of kinetic energy carried by the ions.

2.2 Characteristics of a Dense Plasma Focus

The formation of a dense plasma focus is accompanied by the emission of radiation ranging from infrared to very hard X-rays. In the case of a deuterium or tritium plasma, intense neutron pulses of 10^{10}/discharge are also observed.

The properties of the dense plasma focus have been measured by using various diagnostic instruments [15]-[17],[21]. Image converter cameras and streak cameras are used to record the shape and position of the plasma shock wave at various stages. X-ray pinhole cameras, together with

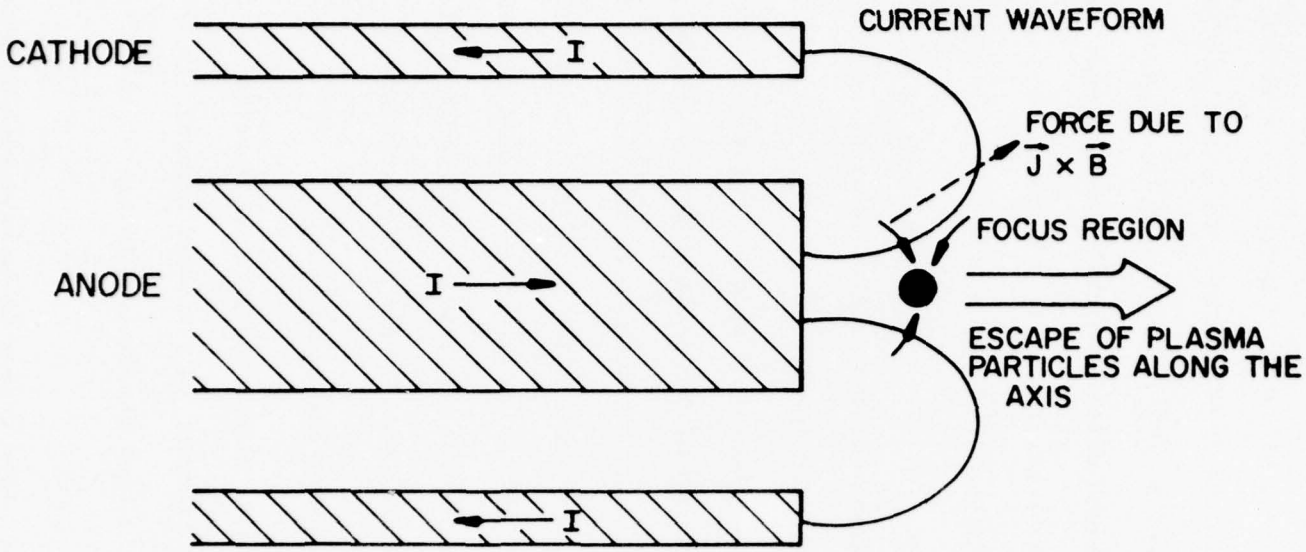

Fig. 2.4. The formation of a dense plasma focus.

different combinations of metallic filters, are employed to record the time-integrated X-ray radiation and to measure the plasma electron temperature. Arrays of solid state silicon detectors are set up to detect and display the time-resolved X-ray pulses on the oscilloscope. Plastic scintillators and photomultipliers are used to measure the time-resolved neutron pulses while arrays of activated-silver Geiger counters are utilized to obtain the absolute time-integrated neutron measurements.

A typical dense plasma focus device is operated at the following parameters: bank voltage $\sim$ 20kV, bank energy $\sim$ 10 kJ, plasma gas of deuterium and a few percent of argon at several torr pressure. Experimental results suggest the presence of certain physical processes during the focus formation.

When the current sheath collapses, the plasma column is compressed and emits very soft X-rays, (the energy is less than a few keV). This pulse is not correlated with any neutron production and lasts about 10 - 40 ns. Then there is harder radiation from the anode surface. This X-ray emission has a wide spectral range from a few keV up to above 300 keV, many times the bank voltage. Onset of this emission from the anode surface is accompanied by a noticeable fading of the plasma luminosity. This pulse lasts about 100 nsec, which is the life time of the focus, and the neutron emission pulse does correlate with this hard X-ray radiation. As the focus decays, considerable amount of radiation in the range of a few keV to about 20 keV is observed from the plasma region, which is attributed to the metallic cloud evaporated away from the anode surface.

Beckner [17] had observed the correlation of the current waveform with the X-ray pulse. His experimental results are shown in Fig. 2.5. The diagram shows that the negative swing of the time rate of change of the current occurs when the plasma focus forms which in turn emits X-rays.

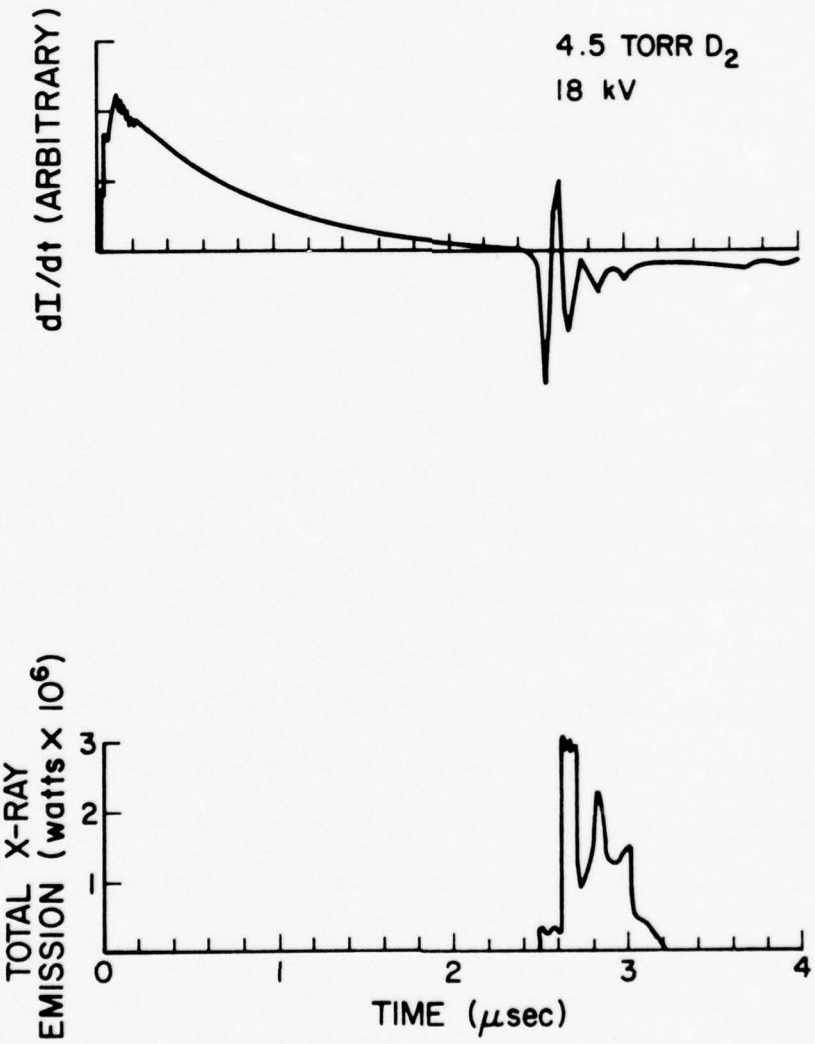

Fig. 2.5. Time-correlated waveforms of discharge tube di/dt and X-ray emission pulse.

At the time when $\frac{dI}{dt}$ reaches its maximum negative value, the pinched current column is fully developed, and X-rays are also emitted at a maximum rate.

2.3 Theoretical Models for the Radiation Process

Experimental results [11], [15]-[17] show that for a dense plasma focus formed by discharging a 20 kV capacitor bank, the energies of the emitted X-rays and neutrons can be as much as 500 keV. This indicates the existence of an acceleration mechanism for the electrons and ions which are responsible for the generation of such energetic X-rays and neutrons. Several explanations have been proposed to account for such an acceleration mechanism.

(a) Lehner and Pohl [22] proposed the beam-target model which describes that at the collapse of the current sheath, an electric field is generated by the m = 0 sausage magnetohydrodynamic instability. The charged particles are accelerated by this intense electric field into high velocities and collide with stationary targets. However, the theoretical calculations cannot fit with the anisotropic distribution of the experimental data. The flux anisotropy is much smaller than that expected for a single beam-target model.

(b) Johnson [23] suggested that the X-ray emission can best be interpreted in terms of a thermal plasma and electron beam radiation at different times of the radiation process. The thermal radiation is of very low energy and, at later stages, is obscured by those due to electron beams with continuous distribution functions. The sources of these beams are thermal electrons which attain sufficiently long mean free paths to attain the electron runaway phenomenon. These electrons are accelerated by induced electric fields to superthermal velocities and impinge upon the plasma and anode surface to generate the hard X-ray.

(c) The "moving boiler" model suggests that the ion velocity is

isotropic in the center of mass of the system, but this center of mass moves in the laboratory frame. This model gives the axial velocity of the ions averaging 2×10^8 cm/sec which is an order of magnitude higher than the maximum velocity (10^7 cm/sec) of the radially collapsing plasma. In the case of a thermonuclear plasma, this average velocity would indicate an ion temperature of 20 keV which is much higher than the estimates of several keV based on other observations.

(d) Bernstein [18] proposed an acceleration model based on computing the individual ion trajectory in the crossed electric-magnetic field of a pinched plasma discharge. His calculation, which is only in the r-z plane, predicts that certain percentages of the ions gain high energies and have large average axial velocities. Gary and Hohl [20] extended Bernstein's work into a three-dimensional case. Their result suggests that strong ion acceleration away from the anode occurs not during the collapse stage but during the focus phase. Also the electrons are accelerated during the focus phase but move toward the anode.

2.4 Electrical Parameters of a DPF System

In most of the plasma gun experiments, the plasma focus is intended to be a radiation source. Since the physical process is an electrical gaseous discharge, it is essential to optimize the electrical parameters of the experiment so as to achieve maximum radiation yield.

In a deuterium or tritium plasma, neutrons are generated at a fusion reaction rate [24] of

$$R = 1/2\ n^2\ \overline{\sigma v} \qquad (2.10)$$

and $Y \propto R$

where Y = neutron yield

R = reaction rate of ions

n = plasma ion density

$\overline{\sigma v}$ = averaged product of the cross section and the ion velocity.

Bennett's relation for a steady-state pinch is

$$I^2 = 200\ NkT \tag{2.11}$$

where I = plasma current

N = total number of particles per cm length of the pinched column

kT = kinetic temperature of the plasma.

Since $n \propto N$ and $Y \propto R$,

$$\therefore Y \propto n^2 \propto I^4 \quad . \tag{2.12}$$

However, Imshennik et al. [25] claim that the correct functional relationship should be $n \propto I^{4.9}$. There is no explicit relationship between the X-ray yield and the current in the plasma. Yet in the case of deuterium or tritium gas experimental results do suggest that the X-ray yield is proportional to that of neutrons. This suggests the importance of maximizing the plasma current in the experiment.

The electrical parameters of the plasma system can be represented by the electrical circuit in Fig. 2.6. The voltage equation is

$$\frac{Q}{C} - L_b \frac{dI}{dt} - R_b I = V(t) = \left[R_g(t) + \frac{dL_g(t)}{dt} \right] I + L_g(t) \frac{dI}{dt}$$

or, in terms of charge, Q,

$$\frac{Q}{C} = \underbrace{\left[R_g(t) + R_b \right]}_{R} + \underbrace{\frac{dL_g(t)}{dt}}_{\frac{dL}{dt}} \frac{dQ}{dt} + \underbrace{\left[L_g(t) + L_b \right]}_{L} \frac{d^2Q}{dt^2}$$

$$\therefore \frac{d^2Q}{dt^2} + \frac{R + \dot{L}}{L} \frac{dQ}{dt} - \frac{Q}{LC} = 0 \quad . \tag{2.13}$$

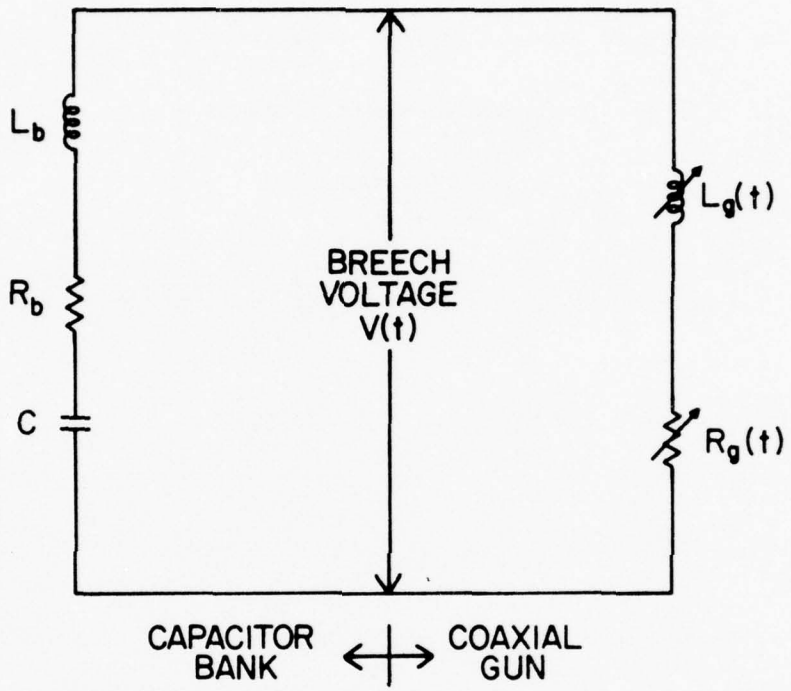

C = total capacitance of the bank

R_b = total resistance on the bank side

L_b = total inductance due to capacitors, transmission lines and electrical connections

$L_g(t)$ = time-varying inductance of the plasma gun during discharge

$R_g(t)$ = time-varying resistance of the plasma gun during discharge

Fig. 2.6. An equivalent electric circuit for the system.

Gates [26] solved this equation for $\dot{L} \neq 0$ (but assumed $\ddot{L} = 0$), and the optimal solution is

$$I = \frac{0.8\ V}{\dot{L}} \quad . \tag{2.14}$$

Therefore, in order to increase the plasma current, the system must be operated at higher voltage and the $\dot{L}$ of the plasma gun be reduced. In Appendix A, the inductance of a plasma gun is estimated.

$$\dot{L}_{gun} = \left[\frac{E^2}{\mu_0 \rho_0}\right]^{1/4} \frac{\mu_0}{2\pi} \ln\left\{\frac{b}{a}\right\} \quad .$$

This shows that in order to reduce the value of $\dot{L}_{gun}$, the gas pressure has to be increased and the radii of the inner and outer electrodes have the same dimension.

Previous experimental results also show that operation of the dense plasma focus device is optimized if the focus occurs at time $\tau/4$, i.e., at the end of the first quarter cycle of the current (τ = period of the plasma current). At this moment, the focus is formed when the current reaches its peak value. This quarter cycle time must be as close to t_p, the arrival time of the current sheath at the end of the gun, as possible. Experimental data show that the value of t_p is on the order of microseconds and as

$$\tau = 2\pi\sqrt{LC} \tag{2.15}$$

both inductance and capacitance of the system must be low enough to meet this condition. For a given bank energy, it is desirable to have high-voltage and low-capacitance capacitors.

2.5 X-ray Emission

2.5.1 Basic X-ray theory

When energetic particles interact with matter, electromagnetic radiations are emitted. In a dense plasma focus, the energetic electrons and ions interact with each other as well as with the electrodes. Copious radiations are emitted and most of them are in the X-ray region. Compton and Allison [27] gave a detailed account of the origin of these X-rays. In general, X-rays can be divided into two types: (1) the line spectrum, or characteristic spectrum, and (2) the continuous spectrum, or Bremsstrahlung.

(1) Line spectrum

Characteristic X-ray radiation can only be produced when the bombarding particle has sufficient energy to remove an electron from the K, L, or M shell of the target atom. If the bombarding particle has an energy greater than the critical absorption energy of, e.g., the K shell, then a K electron may be removed and all the lines of the characteristic K shell may result. These K lines arise from the transitions of the electrons from the higher shells to the vacancy in the K shell and are monoenergetic. However, not all transitions from one shell to another are possible and only some are permitted by the quantum-mechanical selection rules. Because of their lower energies, the intensities of the L lines and the others are very small as compared with those due to K lines.

(2) Continuous spectrum

According to classical electromagnetic theory, when a charged particle of charge q_1 and mass m experiences an acceleration due to another charge q_2, it emits electromagnetic radiation with amplitude proportional to the acceleration, i.e., $q_1 q_2/m$. The intensity will then be proportional to $\left(q_1^2 q_2^2/m^2\right) q_1^2$, which indicates a strong mass dependence. Because the total

intensity of the Bremsstrahlung process varies inversely with the square of the mass of the incident particle, the radiation intensity from a proton will only be one-millionth of that due to an electron of the same velocity. Therefore, in plasma theory, Bremsstrahlung due to ion-ion interaction is negligible as compared to that of ion-electron interaction. Also collisions between electrons produce no radiation in lowest order because the acceleration of one electron is equal and opposite to that of the other, i.e., the incipient electromagnetic waves of the two electrons destructively interfere. Hence only the Bremsstrahlung due to electron-ion interaction is significant. For a Maxwell-Boltzmann distribution of particles, the Bremsstrahlung radiation from a plasma is [24]

$$w_x = 4.8 \times 10^{-37} Z^2 n_i n_e T_e^{1/2} \ W/m^3 \qquad (2.16)$$

where w_x = electromagnetic power radiated from plasma per unit volume

Z = atomic number of the ions

n_i = ion density

n_e = electron density

T_e = electron temperature in keV.

A dense plasma focus has an X-ray spectrum as shown in Fig. 2.7 [28]. A typical spectrum has the line spectra superimposed on the continuous spectrum. In Fig. 2.7, the lines are due to copper and tungsten atoms in the gun electrodes. A large fraction of this X-ray emission is due to energetic electrons bombarding the gun anode, as observed in previous work [11], [12], [17], [23]. The physical process for such an interaction is known as thick-target Bremsstrahlung.

2.5.2 Thick-target Bremsstrahlung theory

The radiation pattern from the interaction of electrons with thick targets is different from that due to thin-target interaction. A target

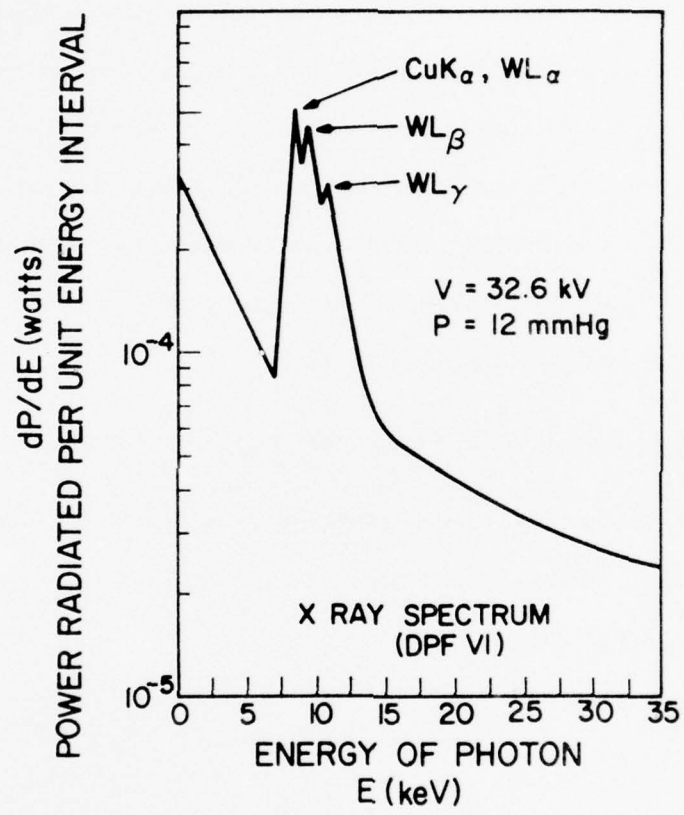

Fig. 2.7. A typical X-ray spectral distribution, $\frac{dP(E)}{dE}$ vs. E (graph obtained from Reference [28]).

is considered to be thin when it consists of only a few layers of atoms. In the limiting case, free atoms are the thinnest targets. The radiation from such thin targets follows Eq. (2.16); the radiation intensity is proportional to the square of the atomic number of the target atoms.

However, in a thick target, all the bombarding electrons are slowed down to a very small residual speed by numerious impacts with target atoms and all the kinetic energy is dissipated into heat and ionization of the target atoms. Later, when those ionized atoms return to their normal states, characteristic X-ray lines are emitted which contribute a substantial portion of the radiation in a DPF. The emission from such a thick target is also complicated by various secondary effects. For instance, the line radiation produced at depth within the target may be absorbed or scattered on its way out of the target. Webster's [29] experimental results are shown in Figs. 2.8a,b. He proposed that a thick-target spectrum can be simply represented by a superposition of a series of thin-target spectra.

Wagner [30] suggested that the spectral distribution from a thick target is

$$\frac{dP}{dv} = \text{constant } Z(\nu_{max} - \nu) \tag{2.17}$$

where $\frac{dP}{dv}$ = differential X-ray radiation intensity per unit frequency interval of the photon

ν = frequency of photon

ν_{max} = highest frequency = E/h

$= \frac{\text{kinetic energy of electron}}{\text{Planck's constant}}$

Z = atomic number of the target.

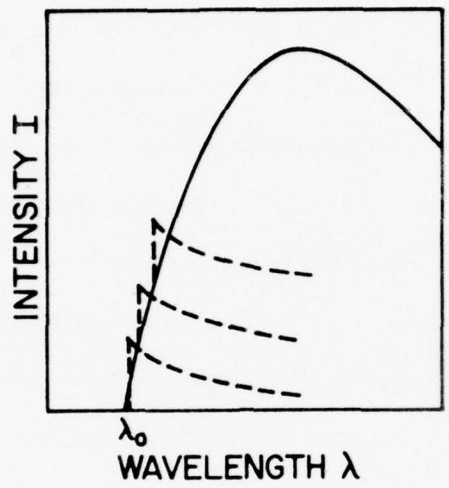

Fig. 2.8a. Analysis of a thick target spectrum into a series of thin target spectra.

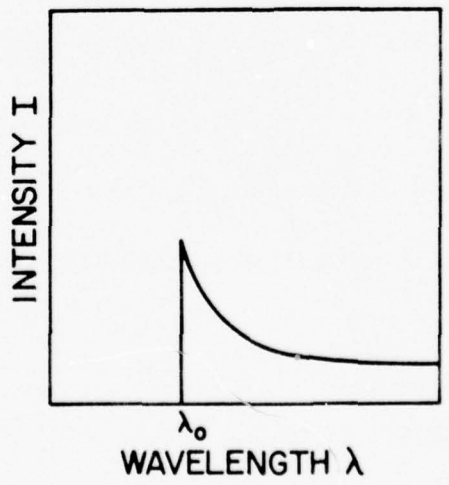

Fig. 2.8b. Energy distribution from a thin target.

Integrating (2.17) over all frequencies, i.e., from $\nu = 0$ to $\nu = \nu_{max}$, the total Bremsstrahlung energy per absorbed electron is

$$P = KZE^2 \tag{2.18}$$

where P = energy in MeV

E = kinetic energy of the incident electron in MeV

K = constant

Z = atomic number of target atom.

In the case of $E << 0.5$ MeV, the experimental value of K[27] is 1.1×10^{-3} MeV^{-1}.

Thick-target Bremsstrahlung theory predicts that X-ray emission is proportional to the first power of the target atomic number, while in Eq. (2.16), ordinary Bremsstrahlung depends on the square of the atomic number.

3. PLASMA-PARTICLE INTERACTION

The problem of plasma-particle interaction has been of great interest in the controlled thermonuclear fusion research. In 1968, Rose [8] initiated this problem for refueling a fusion reactor. Grainick [10] was the first to make a detailed calculation to predict the lifetime of a pellet in a fusion plasma. In his calculation, the vapor cloud from the pellet was assumed to be completely ionized. His result projected a pessimistic view on the feasibility of using pellets to refuel fusion reactors. Foster [31] did the first hydrogen pellet injection into the ORMAK machine in Oak Ridge and Nunnally [32] dropped polystyrene pellets into a theta pinch plasma. Both experiments prove that the assumption of complete ionization of the vapor cloud surrounding the pellet is wrong. In fact the ablated atoms from the pellet still stay in neutral state and provide shielding to the pellet by scattering and slowing down the incoming electrons. Thus the energy flux to the pellet is greatly reduced and the lifetime of a pellet in a fusion plasma is prolonged.

Particle in DPF

In analyzing the interaction of a macroscopic particle with a dense plasma focus, two assumptions are made:

(1) The particle essentially has the same size throughout the lifetime of a plasma focus. Nunnally [32] showed that in his experiment the pellets were ablated by the theta pinch plasma, which had a density of $5 \times 10^{16}/cm^3$ at 300 eV and the interaction time was 1 μsec. Yet a plasma focus has a density of at least $10^{19}/cm^3$ at 1 keV and a lifetime of 100 nsec. Therefore, the interaction time in a focus is only a tenth and the temperature increases by a factor of three. However, the enormous hydrodynamic pressure developed at the collapse of the current sheath compresses the

neutral cloud ablated from the pellet, thus keeping the ablated material right at the surface of the pellet. This compressed cloud essentially has nearly the same density as the solid pellet.

(2) The electron distribution function is Maxwellian, i.e., the electrons are in thermal equilibrium. Bernstein [18] argued that the ions and electrons were nonthermal. But Beckner [19] suggested that the ions and electrons assumed thermal equilibrium. On the other hand, experimental results from different machines have not been able to agree on a particular distribution function.

So, in this analysis, electrons in a focus are assumed to be in thermal equilibrium. The Maxwellian distribution function of electrons is

$$f(v) = n_0\left\{\frac{m}{2\pi kT}\right\}^{3/2} exp\left\{-\frac{mv^2}{2kT}\right\}$$

where n_0 = density of electrons

m = mass of particle

T = temperature

k = Boltzmann's constant

v = velocity of electron.

From the thick-target Bremsstrahlung theory, the Bremsstrahlung radiation emitted by electrons bombarding a solid particle is

$$W_T = \int_0^\infty f(v)Av\tau P(v)4\pi v^2\, dv \qquad (3.1)$$

where W_T = total energy radiated

A = area of the particle

τ = lifetime of plasma focus

$P(v)$ = energy radiated by a bombarding electron with velocity v.

From Eq. (2.18),

$$P(v) = KZ\left(\frac{1}{2} mv^2\right)^2 \quad .$$

Integrating Eq. (3.1), we get

$$W_T = \frac{15}{4} Av\tau KZn_0(kT)^2 \quad . \tag{3.2}$$

Therefore,

$$W_T \propto AZ \quad . \tag{3.3}$$

When a copper anode is bombarded by electrons, and the area under bombardment is the same as the cross-sectional area of a focus, i.e., radius = 1 mm,

$$A_C Z_C = A \times \pi r^2 = 91.1 \text{ mm}^2 \quad .$$

When a spherical particle is bombarded by the electrons,

$$A_T Z_T = 4\pi r_T^2 Z_T \tag{3.4}$$

where r_T = radius of the spherical particle.

In accordance with Eq. (3.2), the relative X-ray output due to a spherical target as compared to that from the copper anode is tabulated in Table 3.1. In Fig. 3.1, the increase in the percentage of X-ray output due to a spherical particle of 1 mm diameter is plotted vs. the atomic number of the target particle.

TABLE 3.1 RELATIVE X-RAY OUTPUT FROM TARGET

PARTICLE MATERIAL	ATOMIC NUMBER	INCREASE OUTPUT % OF X-RAY				
		r=0.1mm	r=0.5mm	r=1mm	r=1.5mm	r=2mm
NITROGEN	7	0.97	24.14	96.55	217	386
ALUMINUM	13	1.79	44.83	179	403	717
ARGON	18	2.48	62.07	248	559	993
NICKEL	28	3.86	96.55	386	869	1,545
COPPER	29	4.00	100.00	400	900	1,600
SILVER	47	6.48	162.07	648	1,459	2,593
XENON	54	7.45	186.21	745	1,676	2,979
GOLD	79	10.90	272.41	1,090	2,452	4,359
LEAD	82	11.31	282.76	1,131	2,545	4,524

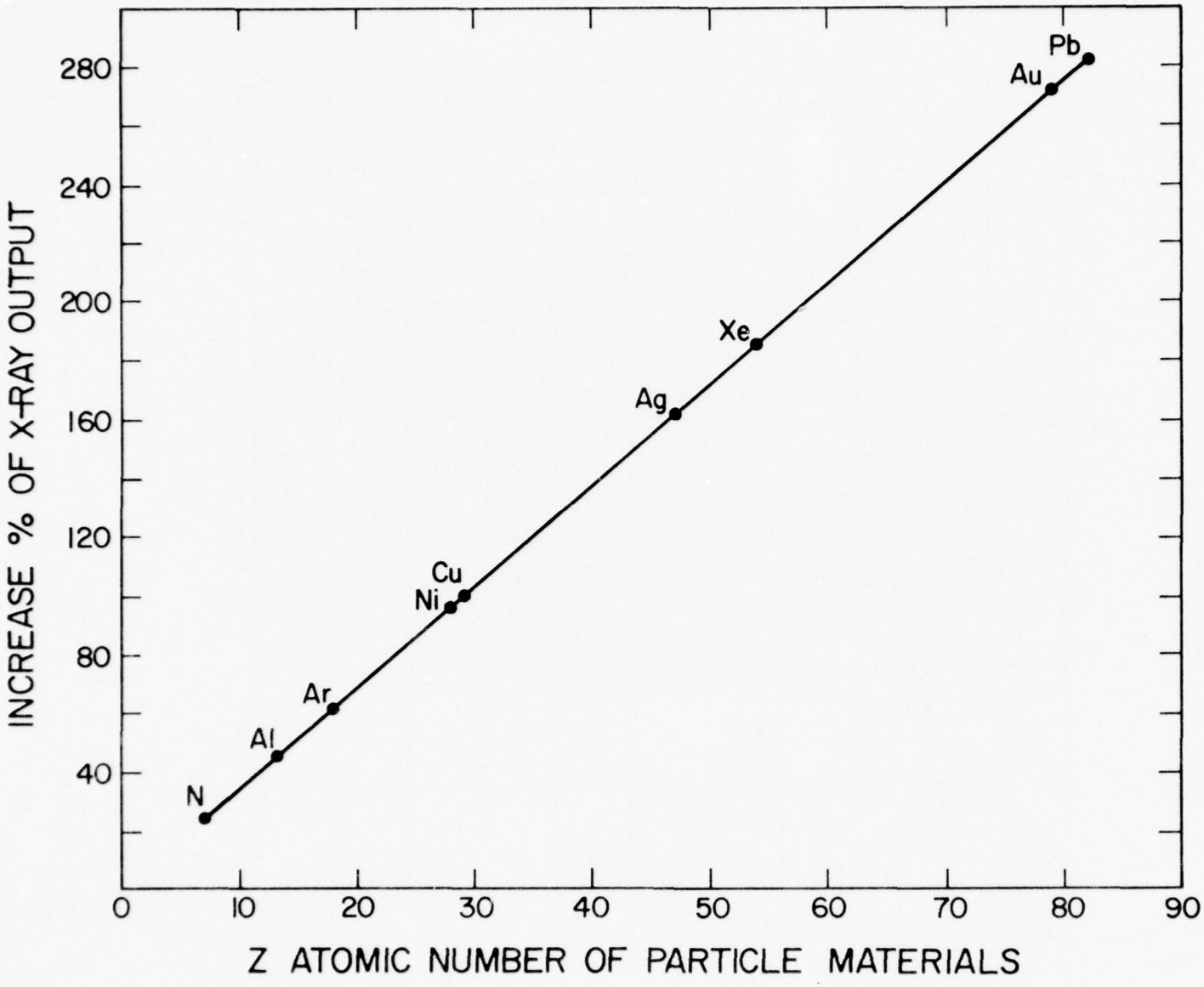

Fig. 3.1. Increase percent of X-ray output for particles with 1 mm diameter.

4. EXPERIMENTAL INSTRUMENTATION

A schematic diagram of the experimental arrangement is shown in Fig. 4.1. In general, the system could be divided into five parts: the hardware, which also included the vacuum system and the controls; the switching mechanism; the plasma gun; the diagnostic tools; and the target. The details of these parts are discussed in the following sections.

4.1 Hardware

The hardware of this experiment included a vacuum system, a pressure control unit, an automatic charging control circuit, a capacitor bank and the electrical connections of different parts. Gross' paper [33] has a very informative discussion on instrumentation for plasma shock wave experiments in general.

4.1.1 Vacuum system

A vacuum system was necessary to provide the environment in which the plasma experiment was performed. The vacuum system in this experiment was composed of Pyrex glass tubes, a gate valve and a Veeco vacuum station. The Pyrex glass tubes consisted of a 6" cross which provided the ports for the plasma gun and other instrumentations, a 6" to 4" reducing tee and some other 4" tubes. A 4" gate valve (Series 5010, by Airco Company, Berkeley, California) was used to connect the tee and the rest of the 4" glass pipes which were connected to the Veeco vacuum station. Closing this gate valve would isolate the plasma chamber from the vacuum station. The Veeco vacuum station used was Model VS-400, which included a mechanical forepump at 15 CFM, a water-cooled, three-stage oil diffusion pump at 400 L/sec, and a liquid nitrogen cold trap. This liquid nitrogen cold trap was needed to

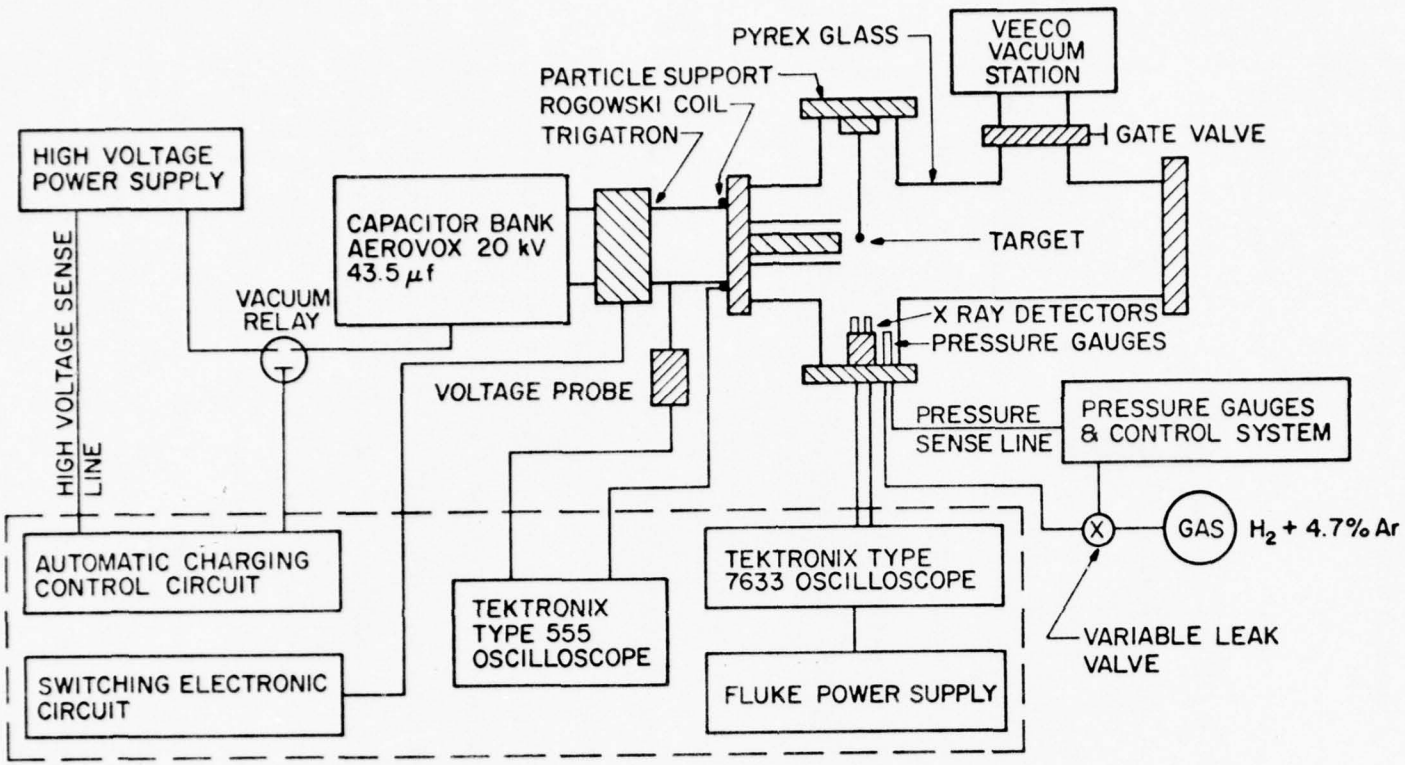

Fig. 4.1. Schematic diagram of the experimental instrumentation.

eliminate any hydrocarbon contaminants from the plasma chamber. By using these pumps, the chamber could be pumped down to 1×10^{-5} torr, which was good enough for this experiment which had a working pressure in the 1 torr range.

4.1.2 Pressure control unit

The pressure control unit consisted of a thermocouple gauge and vacuum control, an ionization gauge and control, a variable leak valve, and a power supply. A Veeco ionization gauge RG 75K and ionization gauge control Model RG-830 were used to measure the vacuum condition in the plasma chamber before the gas was added into it. After the chamber was pumped down to the desired vacuum level and the gate valve was closed, the plasma gas, a mixture of hydrogen plus 4.7 percent argon impurity (at analytic grade, supplied by Linde Division, Union Carbide Corporation, South Plainfield, New Jersey), was leaked into the chamber through a variable leak valve (Model PV-10 by Veeco Company). This leak valve had the leak rate determined by the voltage applied to it and was closed when the voltage was removed. A Hastings thermocouple gauge and vacuum control (Model CVH-23, Teledyne Hastings-Raydist, Hampton, Virginia) was used to monitor this leak valve such that the gas pressure in the chamber could be controlled precisely. A diagram of this control unit was shown in Fig. 4.2. The Hastings vacuum controller supplied the currents to the thermocouple gauge mounted in the vacuum system and measured the DC thermoelectric EMF which was displayed on the meter. A pressure set-pointer could be adjusted to the desired pressure level on the meter. When the pressure in the gas chamber was lower than the level set by the pointer, the relay in the controller unit was in the normally closed position and the AC input lines to the Lambda power supply would be completed. However, when the pressure in the gas chamber increased and the indicating needle passed the set-point,

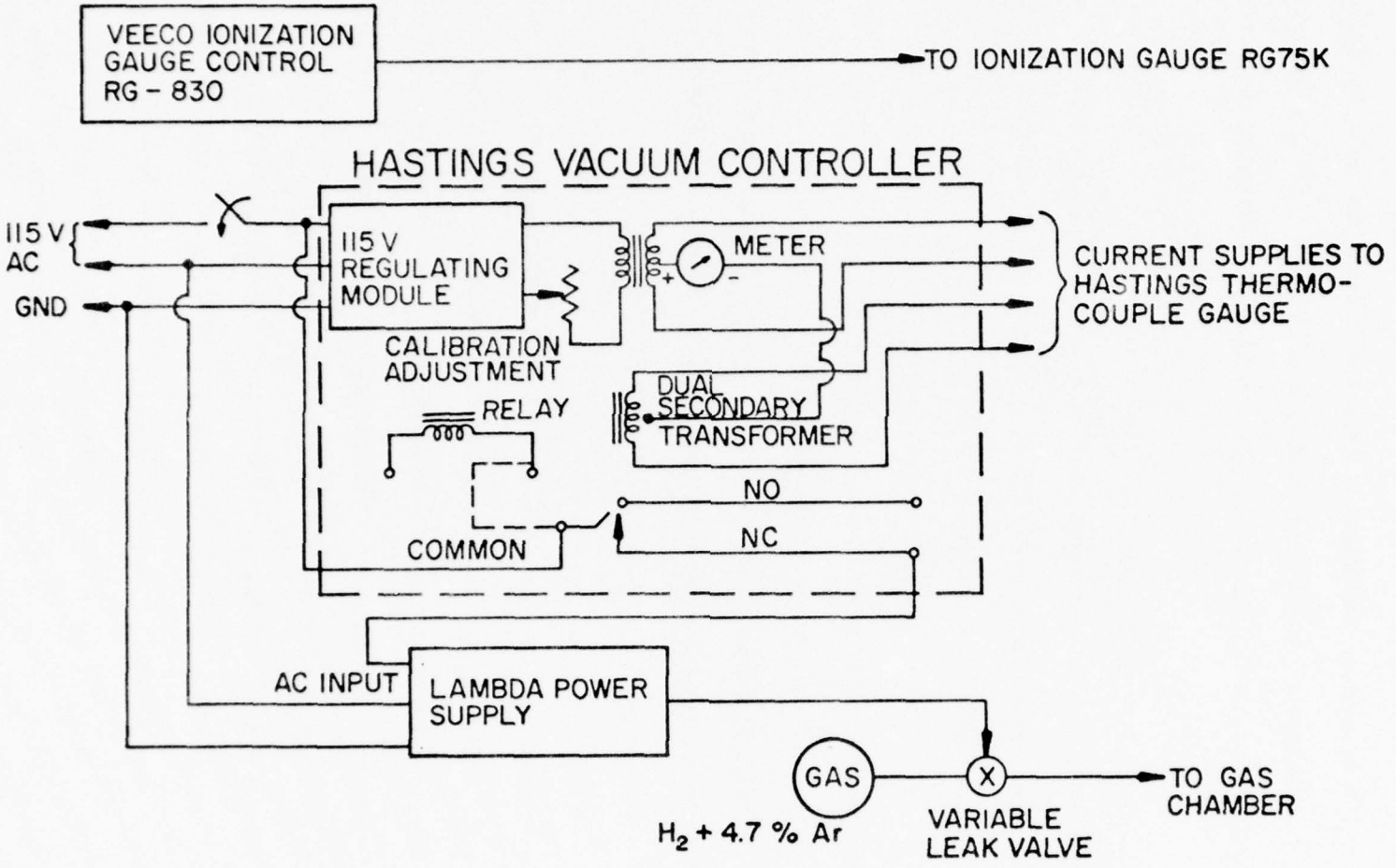

Fig. 4.2. Circuit diagram of the pressure control unit.

the relay would be activated and the AC power to the power supply was then cut off. In turn, the power supply also controlled the voltage applied on the variable leak valve. Thus the pressure of the plasma gas in the chamber could be controlled at the desired level.

In this experiment, the plasma gas was a mixture of hydrogen plus 4.7 percent argon. The addition of the small quantity of argon, or other high atomic impurities, into the gas would slow down the implosion velocity of the current sheath [refer to Eq. (2.8)], giving better thermalization of the ions' and electrons' kinetic energy. Consequently, this rendered the plasma volume and position more reproducible from shot to shot. The higher atomic number of the impurity gas would also enhance the X-ray emission from the plasma as predicted by the Bremsstrahlung theory.

4.1.3 Automatic charging control unit

For safety and convenience in experimental operation, remote control of the process in charging the capacitor bank was necessary. This circuit was shown in Fig. 4.3. A voltage divider was built inside the Universal Voltronics high-voltage power supply (rated at 30 kV, 50 mA) which was used to charge the capacitor bank in this experiment. The 100 kΩ potentiometer was set to a resistance value of 40 kΩ. Hence the resistors gave a voltage dividing ratio of $1:2 \times 10^{-4}$. When the high-voltage power supply was in operation, a small portion of its output voltage would be fed into the input of the automatic charging control circuit via the high-voltage sense line.

The basic principle of the automatic charging control circuit was to compare the high voltage at the capacitor bank with a preset reference voltage such that when the voltage on the capacitor bank was higher than the preset voltage, this control unit would send out a signal to cut off the electrical connection between the power supply and the capacitors.

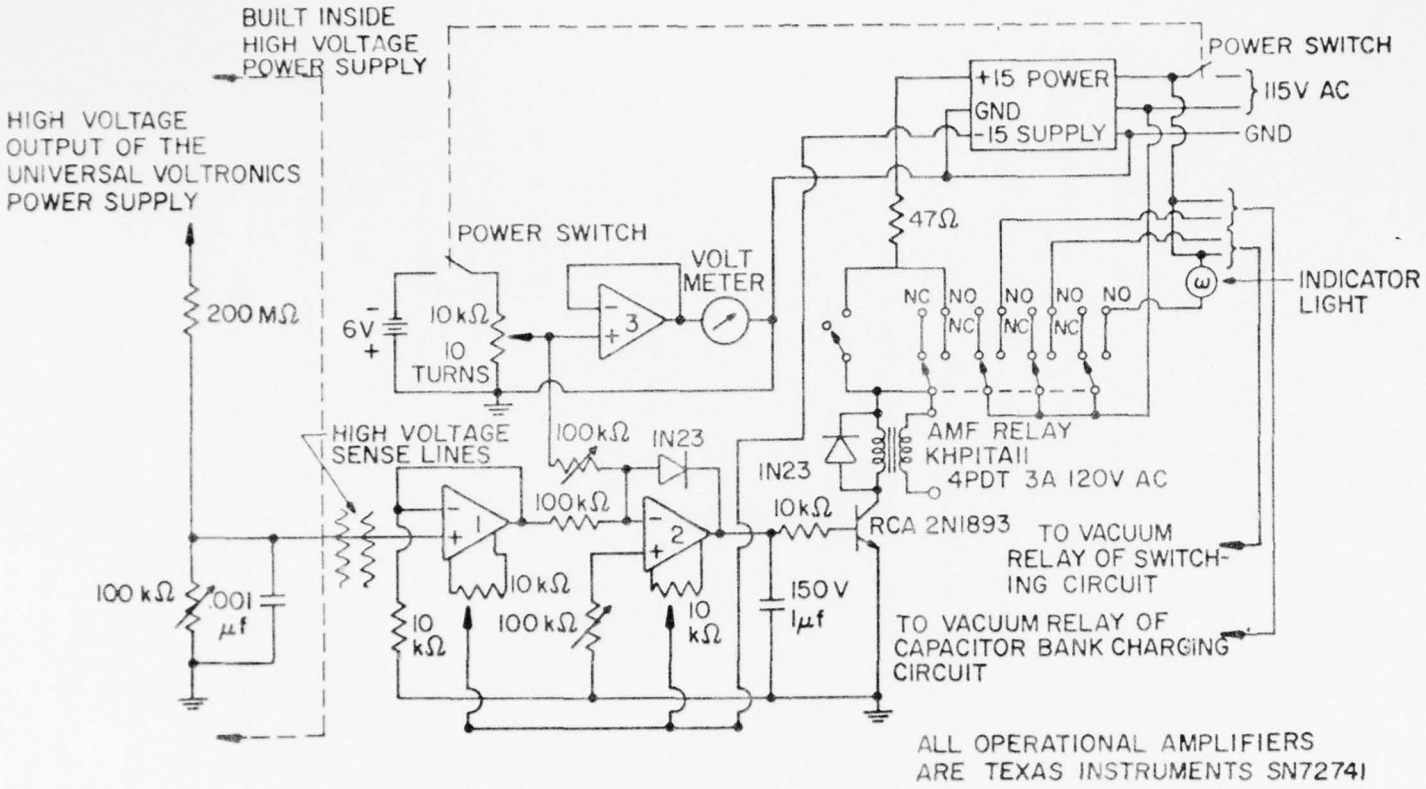

Fig. 4.3. Automatic charging control unit.

Operational amplifiers (Texas Instrument, SN 72741) were used to perform the logic function of comparison. Operational amplifier #1 functioned as a noninverting amplifier and also isolated the input from the rest of the electronic circuit. Operational amplifier #2 compared the reset reference voltage with the output voltage of amplifier #1. A set of nickel-cadmium batteries was employed as the reference voltage source. A ten-turn, 10 kΩ potentiometer was used to set the required reference voltage, which was displayed by a voltmeter. Operational amplifier #3 was wired as a voltage follower so as to isolate the loading effect of the voltmeter on the batteries.

When the power switch of the control circuit was closed, the preset reference voltage would be compared with the output of amplifier #1. If the preset voltage were larger, i.e., the summing voltage at the inverting input of amplifier #2 was negative, then the output of amplifier #2 would be at a positive level which in turn could turn on the transistor RCA 2N1893. When the momentary switch was pushed, the +15 V source was then connected to the solenoid of the AMF relay, Type KHP17A11, and to the collector of the transistor. As long as the base of the 2N1893 was positively biased, the transistor would be on and thus the relay was activated. By this time, even though the momentary switch was open again, the transistor still stayed on once the relay was activated. Under this condition, an indicator light was turned on indicating the completion of the power lines to the high-voltage vacuum relays which controlled the charging of the capacitors in the capacitor bank and in the switching electronic circuit. However, when the voltage at the capacitor bank was higher than the reference voltage, the output of amplifier #2 would be at the negative level, consequently turning off the transistor. Thus the current to the solenoid

of the relay was cut off and the relay was deactivated. In turn, the power to the vacuum relays was cut off. When these vacuum relays opened, the capacitors were electrically isolated from the power supplies. This precaution was necessary to protect the power supplies because it was highly undesirable to have the power supplies and the capacitors connected when the plasma gun was fired.

4.1.4 Capacitor bank and electrical connections

Capacitor bank

The capacitors used in this experiment were Aerovox capacitors rated at 20 kV, and 14.5 μF each. These capacitors were connected in parallel to form a bank which was covered by a wooden box during operation as a safety precaution.

In testing, each of these capacitors was charged to a few hundred volts and then the electrodes were shorted. The discharge current was measured by a Rogowski coil and displayed on an oscilloscope. From the ringing frequency relationship,

$$\omega_c^2 = \frac{1}{LC}$$

where ω_c = ringing frequency of the circuit

L = total inductance of the circuit

C = total inductance of the circuit,

the internal inductance of the capacitor was calculated with known capacitance and measured ringing frequency. The ringing period, $T_c = \frac{1}{f_c}$, was 7.14 μsec. Hence the internal inductance of each capacitor was ∿ 89 nH. This amount of inductance was high for capacitors used in pulsed discharge work. Other inductance measurements showed that the inductance of the spark gap was ∿ 40 nH and of the plasma gun ∿ 30 nH. From the equation,

$$\omega_s^2 = \frac{1}{\left(\frac{L_c}{n} + L_{sg} + L_{gun}\right) \times n \times C}$$

where ω_s = ringing frequency of the system

L_c = inductance of each capacitor in the bank

C = capacitance of each capacitor in the bank

L_{sg} = inductance of spark gap

L_{gun} = inductance of plasma gun

n = number of capacitors connected in parallel in the bank.

The calculated value of the ringing period T_s $\left(T_s = \frac{2\pi}{\omega_s}\right)$ was 13.08 μsec, and the measured value 13.1 μsec. Hence the quarter-cycle risetime would be $\sim$ 3.25 μsec. From Eq. (2.9), the pinching time of the current sheath for 10 kV at 1 torr of hydrogen + 4.7 percent argon was 1.4263×10^{-6} sec. As the current was discharged from the capacitor bank in sinusoidal form, the plasma current at pinching time was only 63.2 percent of the maximum available current. This indicated that the inductance of the system, especially the capacitors, was relatively high for the experiment.

The total capacitance of the bank was 43.5 μF and the bank energy was 7.85 kJ at 19 kV. The discharge current at 19 kV was $\sim 400 \times 10^3$ A, as measured by the Rogowski coil.

Transmission lines and electrical connections

Aluminum plates of 1/16" thickness were used as transmission lines to provide electrical connections from the capacitor bank to the trigatron and then to the plasma gun (Fig. 4.4). The plates were separated by 20-mil-thick mylar sheets. Brass bolts of 1/4 - 20 NC and washers were used to connect the plates to different parts. In order to provide better electrical contacts at these joints, #40 mesh copper screen plated with silver was used

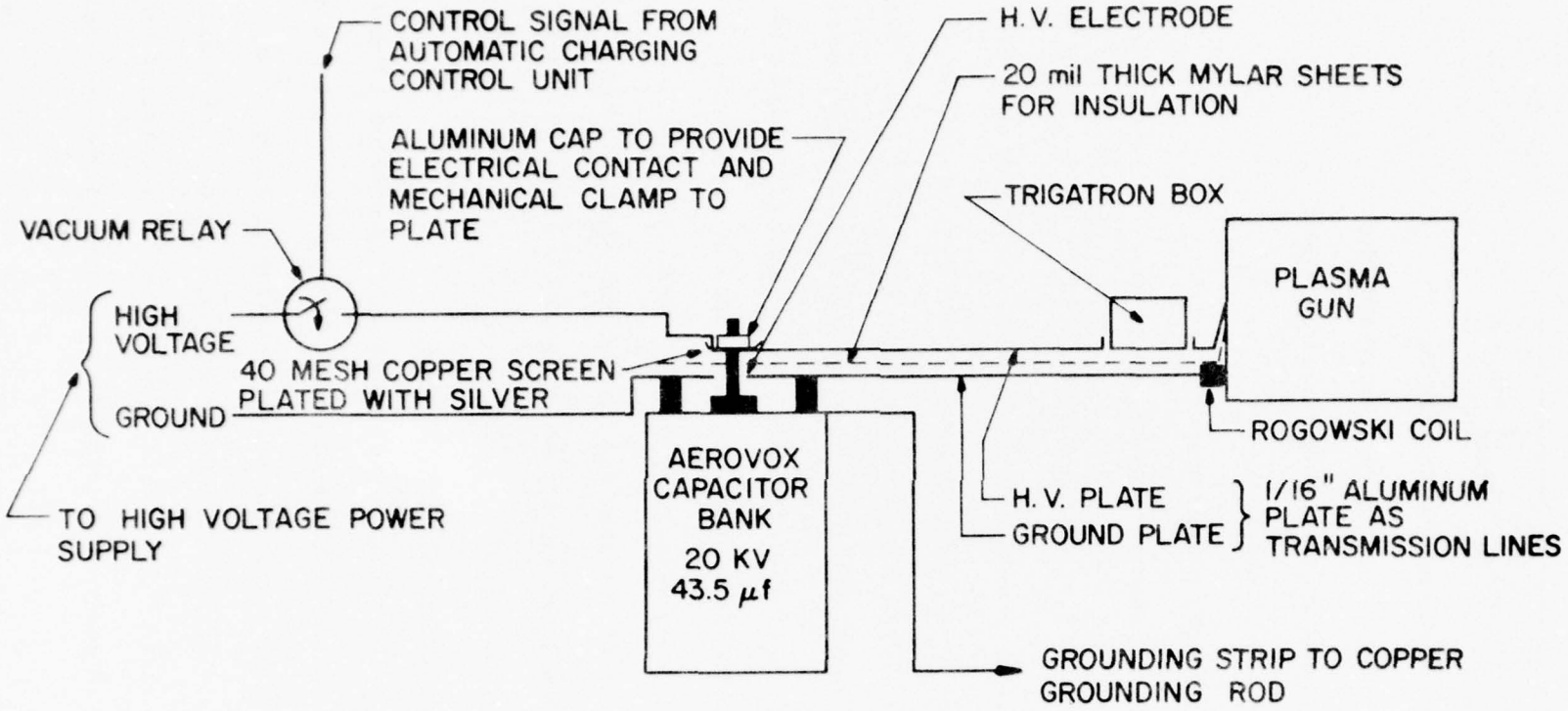

Fig. 4.4. Electrical connections of the capacitor bank.

to seam those joints. Aluminum caps were screwed down onto the nongrounded electrodes of the capacitors to provide electrical contacts as well as mechanical clamping to the high-voltage plate of the transmission line.

Noise shielding and grounding

Because of electromagnetic interference, which is a characteristic of pulsed gaseous discharge experiments, shielding was required to protect the instrumentation and diagnostic signals. A copper screen room was built to shield the electronic systems and the oscilloscopes. All the inputs and outputs to the screen room were also carefully shielded. N-type electrical feedthroughs were soldered at the screen room to provide the interface. The line filters we employed for AC power lines were EMI filters, Model 10R3, 10A, 115/250 V, 50 - 400 Hz (by CORCOM, Chicago, Illinois). Solid coaxial cables were used to provide the electrical connections between the diagnostic instruments near the plasma gun and the instrumentation inside the screen room. These cables were 1/2" foam dielectric heliax cables, RG-366/U, 50 Ω impedance, with solid inner copper conductor and solid corrugated outer copper conductor (available at Andrew Corporation, Orland Park, Illinois). These cables were satisfactory in shielding the signals from EMI noise in this experiment.

In this high-voltage experiment, safety precautions were an important consideration. Because of the high current delivered in a short time, $\frac{dI}{dt} \sim 10^{12}$ A/sec, stray inductance of a few nanohenries would produce stray voltage in kilovolts. With megamps, milliohm resistance would also give rise to kilovolts. Therefore, ground leads were made as short as possible. Single-point grounding was used to avoid ground loops because the stray inductance of any ground loop could generate a large spurious signal to

mask any low-level diagnostic signals. Also, for safety purposes, the grounding lead was connected to a 1" diameter copper rod hammered five-feet deep into the ground.

4.2 Switching Mechanism

This dense plasma focus system, like any other high-energy, high-power fusion experiment, needed a switching device to close the electrical circuit at a desired moment such that the stored electrical energy could be delivered to a load. This switching mechanism had two essential parts: a switch and a switching circuit which provided the signal.

4.2.1 Spark gap

There are many different types of switches available. But, in general, they can be classified into four categories [34]:

(1) Gas switches: These switches use gas as the dielectric medium and can handle high currents and multimegavolts using increased pressure and electronegative gases such as SF_6, sulfur hexafluoride. These switches have the advantage of a self-healing dielectric and are capable of repetitive operation with minimum maintenance. But care must be taken in handling the toxic decomposition products of some of the gases, like SF_6 and Freon.

(2) Liquid switches: These switches use liquid as the dielectric medium and also have the advantage of a self-healing dielectric. As compared to the gas switches, the liquid switches can have closer spacing of electrodes, resulting in lower inductance and faster risetime. The drawback of these switches is the occasional inconvenience in the experimental setup.

(3) Solid switches: These have solid dielectrics, can handle very large current, and have very low impedance. These switches are triggered either by electromechanical puncturing or by means of an exploding wire or foil. The biggest drawback is the lack of self-healing and thus it is necessary to replace the dielectric after each switching.

(4) Vacuum switches: These switches enjoy the advantages of high dielectric strength, rapid deionization time, wide voltage range, high current capability, low inductance and quiet operation. Yet care must be taken to shield the radiation resulting from the rapid acceleration of charged particles in the vacuum environment.

The nature of the electrical load determines the particular type of switch to be used. In this experiment, commercial units of a hydrogen thyratron tube, 5C22, and two vacuum relays were employed in the switching circuit while a custom spark gap was designed to handle the main switching of the plasma current.

Design criteria of switches

The main criteria for custom-designed switches are:

(i) the voltage holdoff which determines the maximum voltage that the switch can hold without self-breakdown,

(ii) the inductance which determines the rate of current rise and the current capability,

(iii) the delay which is the time that it takes a switch to close after the signal is applied,

(iv) the jittering which measures the accuracy of the delay repeated from closure to closure and is important in the synchronization of the whole system,

(v) the dielectric recovery time which determines the repetition rate that the switch can operate,

(vi) and the operating life which means the maximum number of times that the switch can function properly.

These criteria, together with the particular switching requirements of the experimental system, determine the geometry, the type, and the materials of the switch.

In this experiment, a solid-state switch is ruled out because its lifetime is limited to one shot. Yet this type of switch has the fastest closing rate because of the high electric field possible and dielectric density. Also, electrode erosion rate in liquid is extremely high. However, a gas switch seems to be favorable because it encounters much less electrode damage and has self-healing dielectric properties.

In order to have a gas switch with a long life, the choice of gas and electrode materials has to be considered. Decomposition of certain high-dielectric-strength gases such as SF_6 and Freon in enclosed switches may deposit conducting materials which ultimately limit the device lifetime by degrading its dielectric envelope. Other gases, such as nitrogen or air, do not have such a drawback.

The dielectric recovery time of a gas switch after discharge depends on the electrode materials and geometry, the gas composition and pressure, the arc length and the current. A switch is recovered when the charge carriers generated during the discharge are dispersed, the heat generated during the closed phase is lost through the electrode, and the dielectric strength exceeds the reapplied stress. Electrodes made of Elkonite have better voltage recovery than those with copper or tungsten. This particular material is a sintered composite which combines the high thermal conductivity of copper with the refractory properties of tungsten. Smirnov [35] suggested a way to enhance the recovery time by blowing air through the spark gap to cool it and remove discharge debris.

Electrode erosion is another important factor determining the lifetime of a switch. The products from erosion can be deposited on the surfaces of the insulators in the switch, thereby shortening its life. Basically, erosion of electrode material is due to heating, which is associated with

the bombardment of electrode surfaces by the charged particles. Usually because of such brief and powerful thermal fluxes, and the limited heat conduction of electrode material, these electrode surfaces can be heated to the melting temperature. For currents below ten kiloamperes, the erosion results mainly from vaporization of materials. However, larger currents will eject molten materials from the surface, resulting in much larger erosion.

Trigatron

Based on the aforementioned factors, a three-electrode spark gap, also known as a trigatron, was designed and built for this experiment. The basic arrangement of a trigatron is shown in Fig. 4.5. The high voltage is applied between electrodes 1 and 2 without exceeding the self-voltage breakdown limit. A third electrode, the trigger electrode, is in the form of a pin and is placed within the host electrode. When a pulse of several kilovolts is applied at the trigger and host electrodes, a discharge is initiated supplying charge carriers which under local field intensification rapidly cause the main gap to conduct. At this later stage, streamers are formed to develop a main stroke propagating at 10^8 - 10^9 cm/sec. Shkuropat [36] had investigated extensively a trigatron operation and a summary of his work on the electrode polarity and trigatron characteristics was listed in Table 4.1.

The complete design of the spark gap used in this experiment was illustrated in Fig. 4.6a,b. Half of an OFHC copper rod was silver-soldered onto a 1/2" thick brass plate. This was used as the "opposite" electrode. The host electrodes were two half-spheres made of copper with Elkonite (57 percent tungsten, 43 percent copper) inserts silver-soldered at the tips. Tungsten wires (0.020" diameter) were used as the trigger electrodes,

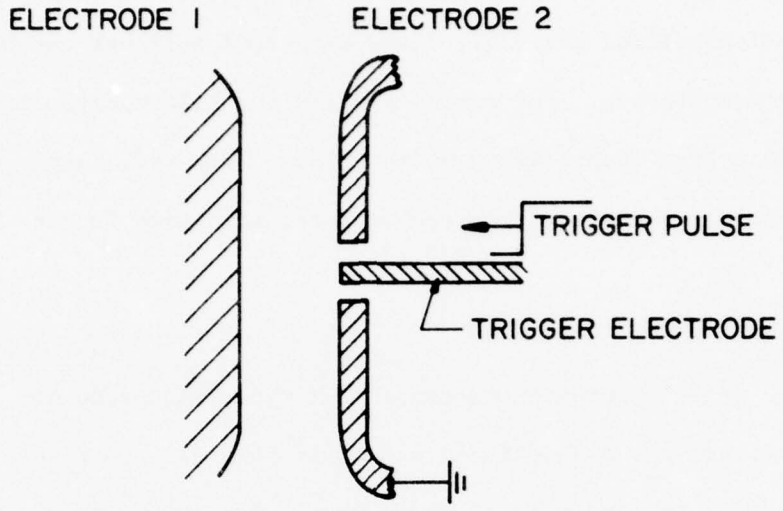

Fig. 4.5. A basic trigatron.

TABLE 4.1.

ELECTRODE POLARITY AND TRIGATRON CHARACTERISTICS

VOLTAGE RANGE	JITTER	TRIGGER ELECTRODE	OPPOSITE ELECTRODE	HOST ELECTRODE
↑ wider	↑ shorter	+	−	+
		−	−	+
		−	+	−
		+	+	−

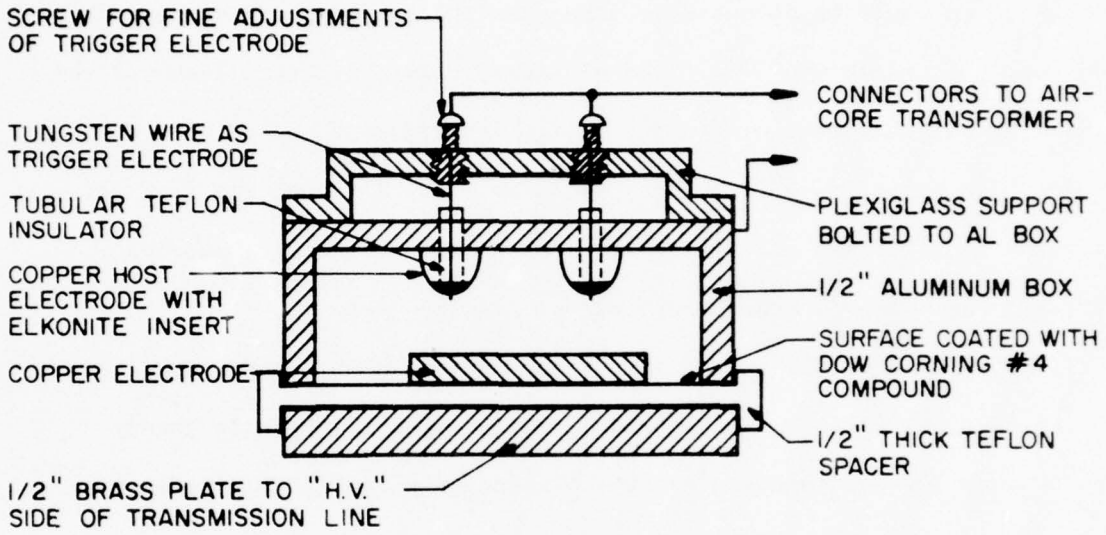

Fig. 4.6a. The front view of the spark gap box.

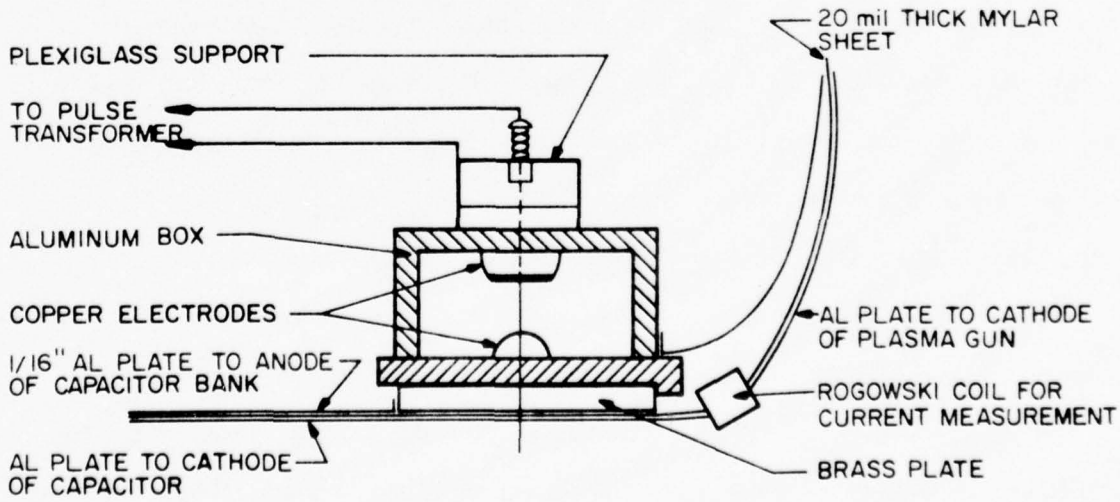

Fig. 4.6b. The side view of the spark gap and its connections.

which were inserted through the holes in the host electrodes and were isolated with tubular teflon spacers. These wires were soldered to two screws which could be adjusted to fine-tune the spark gaps such that the two host electrodes would be fired simultaneously. Figure 4.7 showed the firing of only one host electrode. All these adjustments and host electrodes were bolted to a 1/2" thick aluminum box. This box was isolated from the bottom brass plate by a 1/2" thick teflon spacer. The whole assembly was clamped together by four plexiglass bars.

The surface of the teflon spacer facing the host electrodes was coated with Dow Corning #4 compound (a high-voltage dielectric grease produced by Dow Corning Corporation, Midland, Michigan). The presence of this coating helped to minimize tracking and flashover between the bottom electrode and the edges of the aluminum box. Also, in the firing of the spark gap, metal vapors from electrode erosion were deposited inside the box. Without the grease coating, those vapors would be embedded into the teflon insulator and thus provide a conducting layer. This would require a new teflon spacer. Yet a grease layer could eliminate this problem. After about two-hundred shots, the grease and the metal debris were removed and the teflon surface was regreased. The dielectric grease helped to ease the maintenance problem.

The setup of the spark-gap box was shown in Fig. 4.6b. The bottom brass electrode was connected to the anode of the capacitor bank by an aluminum plate and the upper half of the box was connected to the anode of the plasma gun. The trigger electrodes and the host electrodes through the aluminum box were connected to an air-core pulse transformer. Air at atmospheric pressure was used for this spark gap for simplicity. After each firing, the gap was flushed with compressed air.

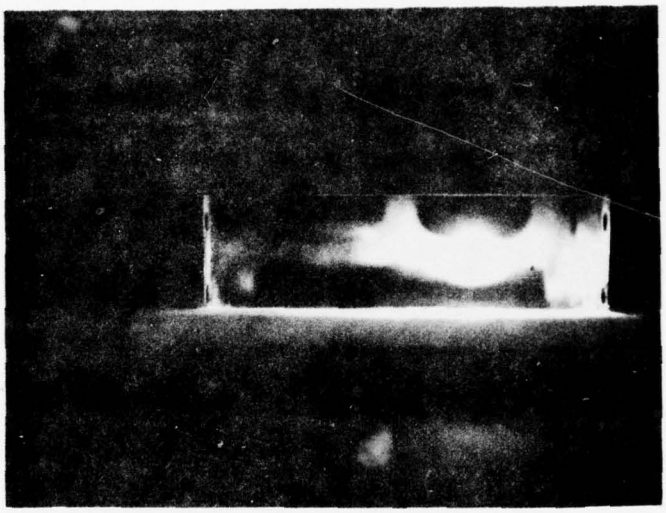

Fig. 4.7. Test firing of the spark gap. Only one host electrode was fired.

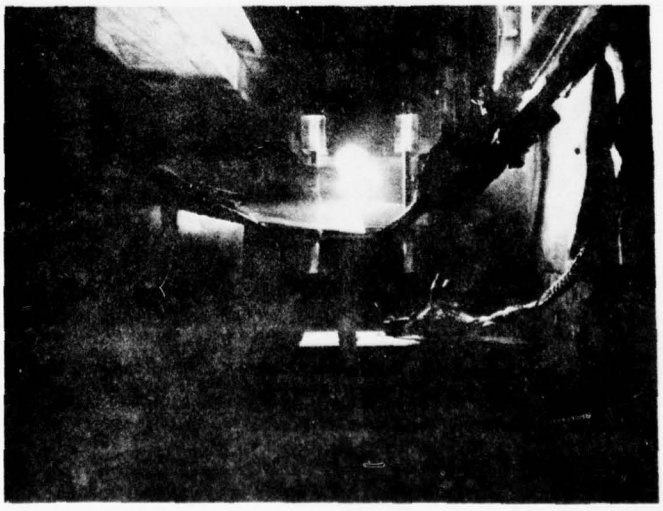

Fig. 4.8. Light emission from the spark gap when the system was in operation.

This spark gap was measured to have a risetime of ∿ 60 nsec, jittering of ∿ 15 nsec, and inductance of ∿ 40 nH.

Very bright light was emitted from a hole in the trigatron box when the plasma gun was fired (Fig. 4.8). There were also streaking lines shooting above the wooden cover. Two trigger electrodes were shown in Fig. 4.9. The left one was a new tungsten electrode with nickel plating. The right one had been tarnished and eroded after 50 shots. The end of the right electrode was sharpened due to erosion. Figure 4.10a showed the deposit of the electrode material within the aluminum housing. Figure 4.10b showed the erosion of the copper rail electrode.

4.2.2 Switching circuit

A switching circuit was needed to monitor the trigatron. In an early attempt, solid-state devices were used in the switching circuit to provide a fast-rising, high-voltage pulse to trigger the spark gap (Fig. 4.11). By closing the microswitch, a 2 μsec pulse was fed to the Schmidt trigger input of a Texas Instrument SN74121 monostable multivibrator, which in turn triggered the $Q_1 - Q_2$ Schmidt trigger to give a 300 V/μsec pulse to the grid of the hydrogen thyratron tube, 4C35. When the thyratron tube fired, it discharged the energy stored in capacitor C_1 through the 3 kΩ resistor producing a 70 kV/μsec pulse at the trigger electrodes of the spark gaps. A series of twenty HEP170 diodes was in line to safeguard the possibility of any backlash from the capacitor bank. This circuit performed satisfactorily in the trial runs. But under the real operation of the plasma gun, from time to time the solid-state electronic components were wiped out by the large electromagnetic pulse generated from the capacitor bank discharge. Efforts to improve impedance matching and pulse isolation turned out to be fruitless. The solid-state devices were susceptible to

Fig. 4.9. Difference between two trigger electrodes. The left one was new and the right one was eroded after 50 shots.

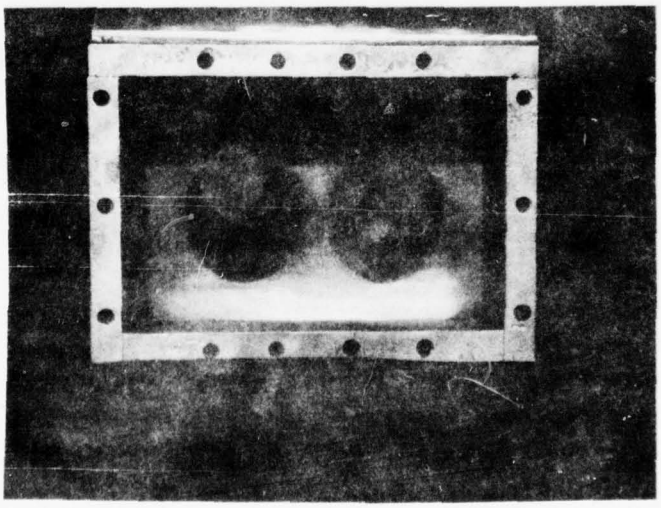

Fig. 4.10a. Deposit of the electrode material within the aluminum housing.

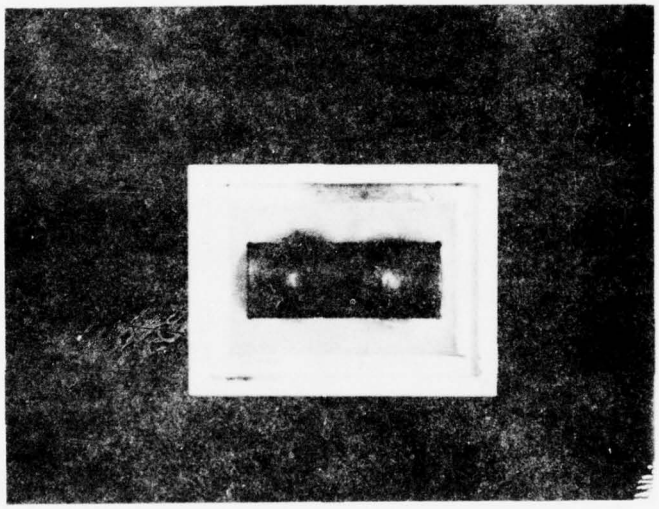

Fig. 4.10b. Erosion of the copper rail electrode.

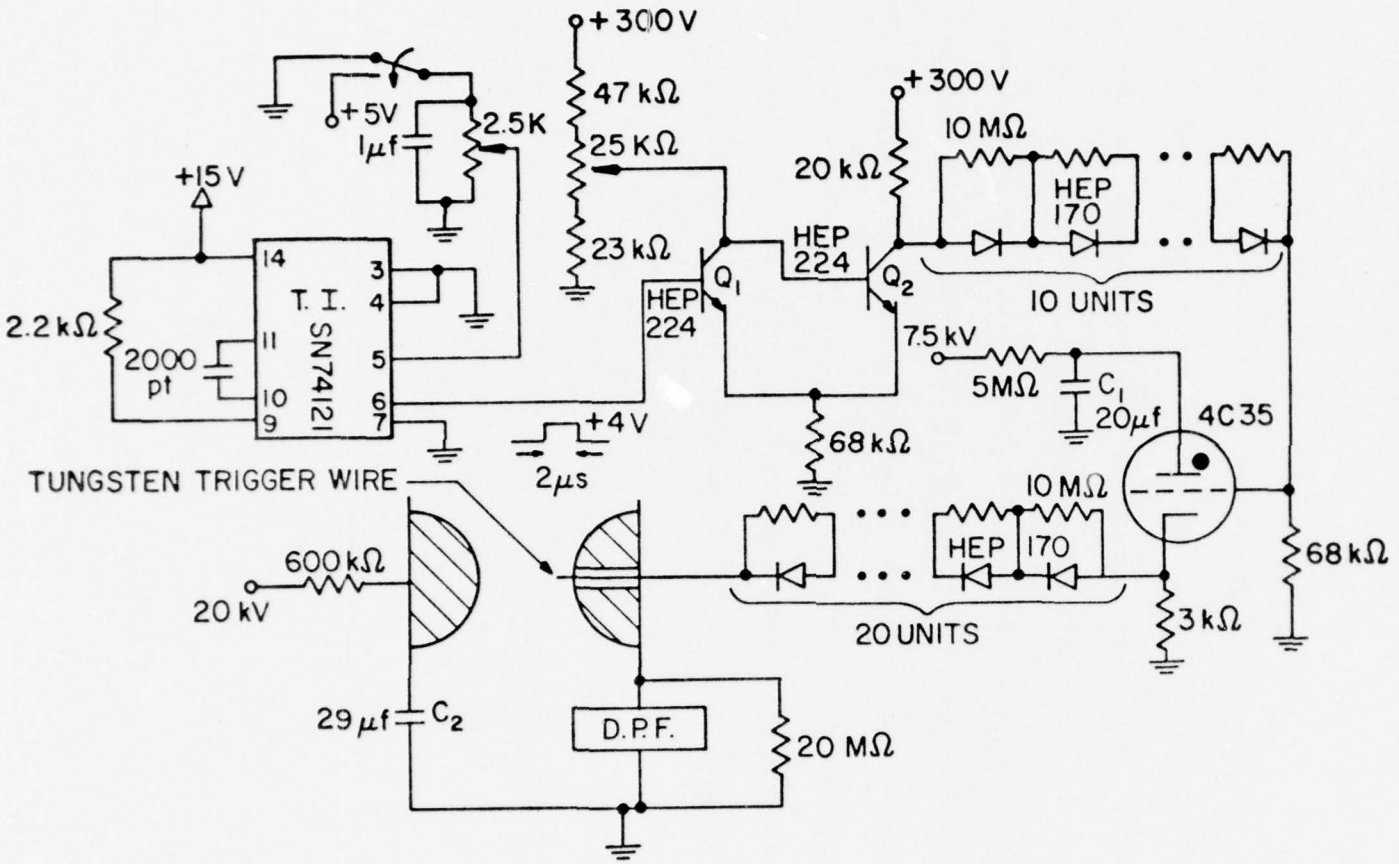

Fig. 4.11. The initial design of the solid-state switching circuit.

electromagnetic noise in the hundred volt range. On the other hand, the vacuum tube devices could stand this kind of noise without damage. Consequently, the switching circuit was redesigned as shown in the block diagram in Fig. 4.12.

In the block diagram of the switching circuit (Fig. 4.12), the manual switch, the Tektronix waveform generators, and the automatic control circuit were housed in the copper screen room to shield them from any RF noise. At the desired moment, the momentary manual switch was signaled to generate a 5 V pulse to the Tektronix Type 162 waveform generator which in turn triggered the Type 161 pulse generator to send out a pulse with an amplitude of 25 V and a pulse width of 100 μsec (see Fig. 4.13a). This pulse was further amplified by the triggering pulse amplifier to 385 V (Fig. 4.13b,c). The triggering pulse amplifier circuit (Fig. 4.14) consisted of an RCA 2D21 thyratron tube and the auxiliary power supplies. A negative bias of -7.5 V at the grid of the tube was needed to turn off the 2D21 tube when the pulse was over. The output pulse of this amplifier was then fed into the grid of the 5C22 hydrogen thyratron tube (Kuthe Laboratories, Incorporated, Newark, New Jersey) in the triggering circuit for the spark gap (Fig. 4.15). In this circuit, a vacuum relay controlled the charging of a 2 μF capacitor, up to 8 kV in operation. When the thyratron tube was fired, this capacitor would be discharged through the thyratron tube and the primary coil of an air-core pulse transformer. The secondary coil of this transformer, with a voltage step-up ratio of 1:2, transmitted this high-voltage pulse to the trigger electrodes of the trigatron switch. This transformer provided the isolation between the trigatron and the switching electronics when the plasma gun was fired. In order to safeguard the 5C22 tube against a possible reverse voltage pulse from the capacitor bank discharge, a series of diodes and resistors was used to clamp any negative pulses going to the anode of the thyratron tube.

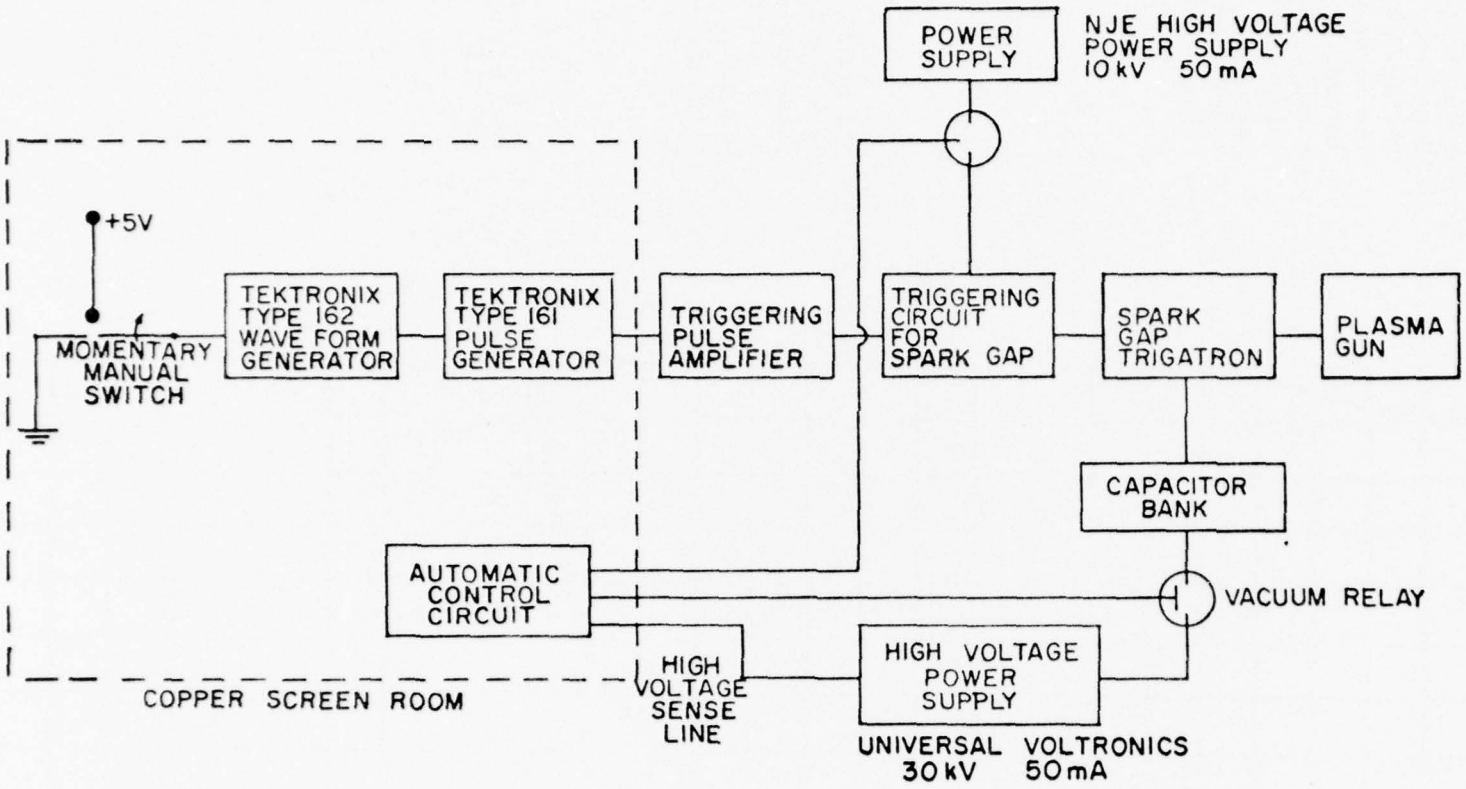

Fig. 4.12. The block diagram of the switching circuit.

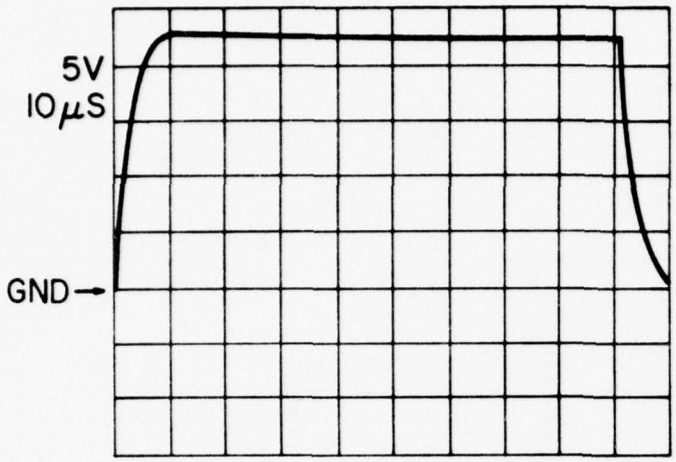

Fig. 4.13a. Output waveform from the pulse generator, Tektronix Type 161. The scope was internally triggered by this pulse. Pulse height 25 V; pulse width 100 μs.

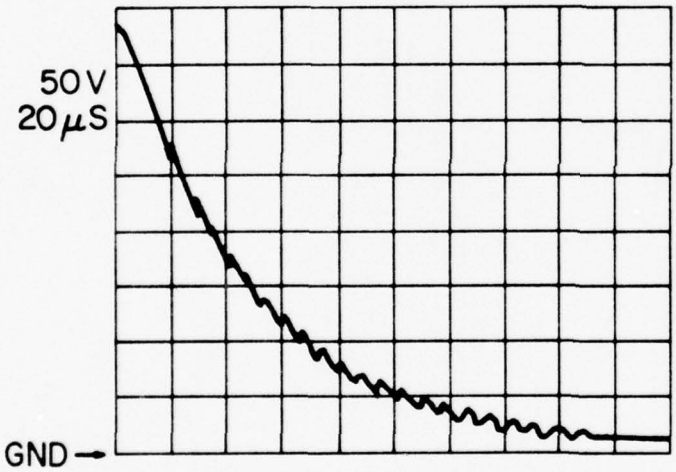

Fig. 4.13b. The output waveform from the triggering pulse amplifier, under no load condition. The scope was self-triggered. Pulse height 385 V.

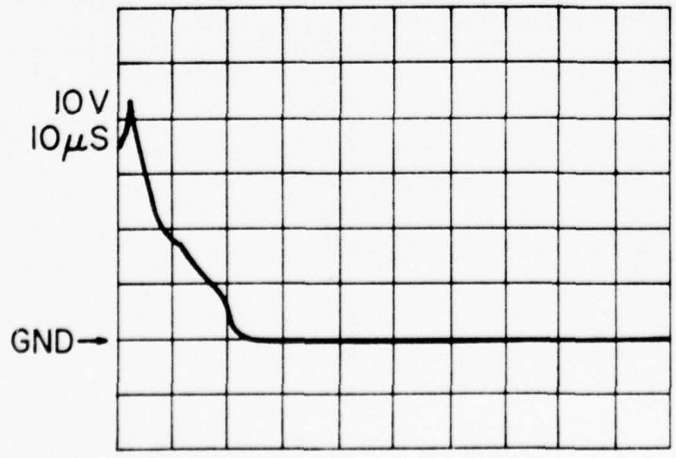

Fig. 4.13c. The output waveform from the triggering pulse amplifier, with a hydrogen thyratron tube 5C22 as a load. The scope was self-triggered. Pulse height 46 V.

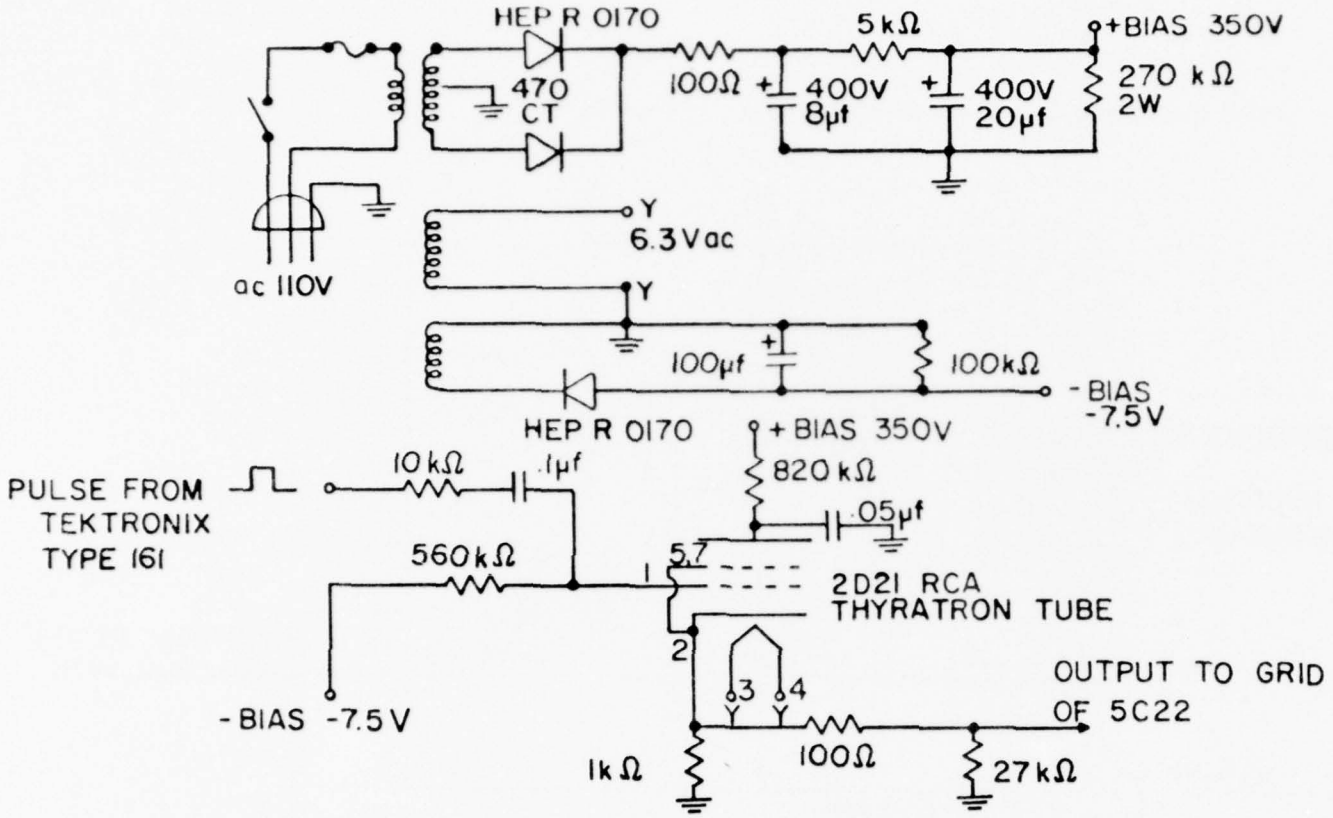

Fig. 4.14. Trigger pulse amplifier circuit.

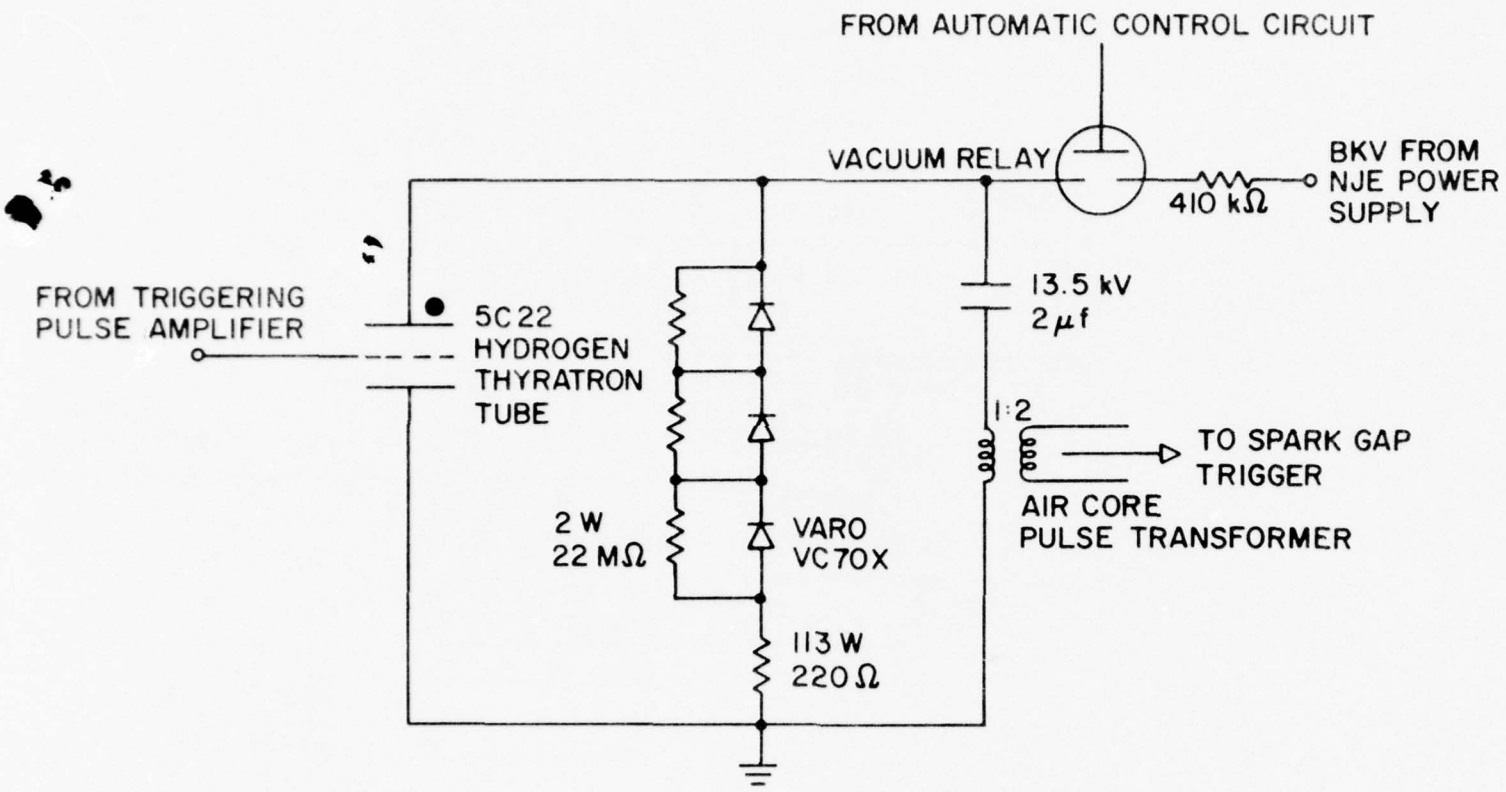

Fig. 4.15. Triggering circuit for the spark gap.

4.3 Plasma Gun

The plasma gun is a pair of coaxial cylinders which guide the plasma sheath to a position where the focus is formed. Several factors have to be considered in designing this gun:

(1) A perforated cathode is needed to prevent any pileup of gas during the acceleration stage of the focus.

(2) The geometry and the dimensions determine the inductance of the gun (see Appendix A). The length of the gun is related to the current collapse time by Eq. (2.9).

(3) The assembly of the gun must be designed vacuum tight to meet the vacuum requirements of the experiment.

(4) The dimensions and types of insulating materials must exceed the self-breakdown, high-voltage conditions.

The plasma gun used in this work was shown in Fig. 4.16. The overall length of the gun was 8.615". The outer electrode consisted of eight 1/2" diameter brass rods arranged in the form of a squirrel cage. This was used as the cathode of the gun. The anode, a solid rod made of OFHC copper, was silver-soldered to a brass plate for mounting and electrical connection. A disc of Elkonite was silver-soldered at the end of the anode so as to reduce the erosion of materials in that area. A piece of plexiglass was used as a dielectric spacer, which separated the anode and the cathode plates. A ceramic insulator was used to provide the surface for electrical breakdown. The anode was bolted tightly to the cathode with the plexiglass sandwiched in between. This arrangement restricted the gun to move as a whole piece during the electrical discharges. Any relative movement between the anode and cathode could crack the ceramic insulator. Also, the bolts were electrically isolated from the anode by the nylon spacers.

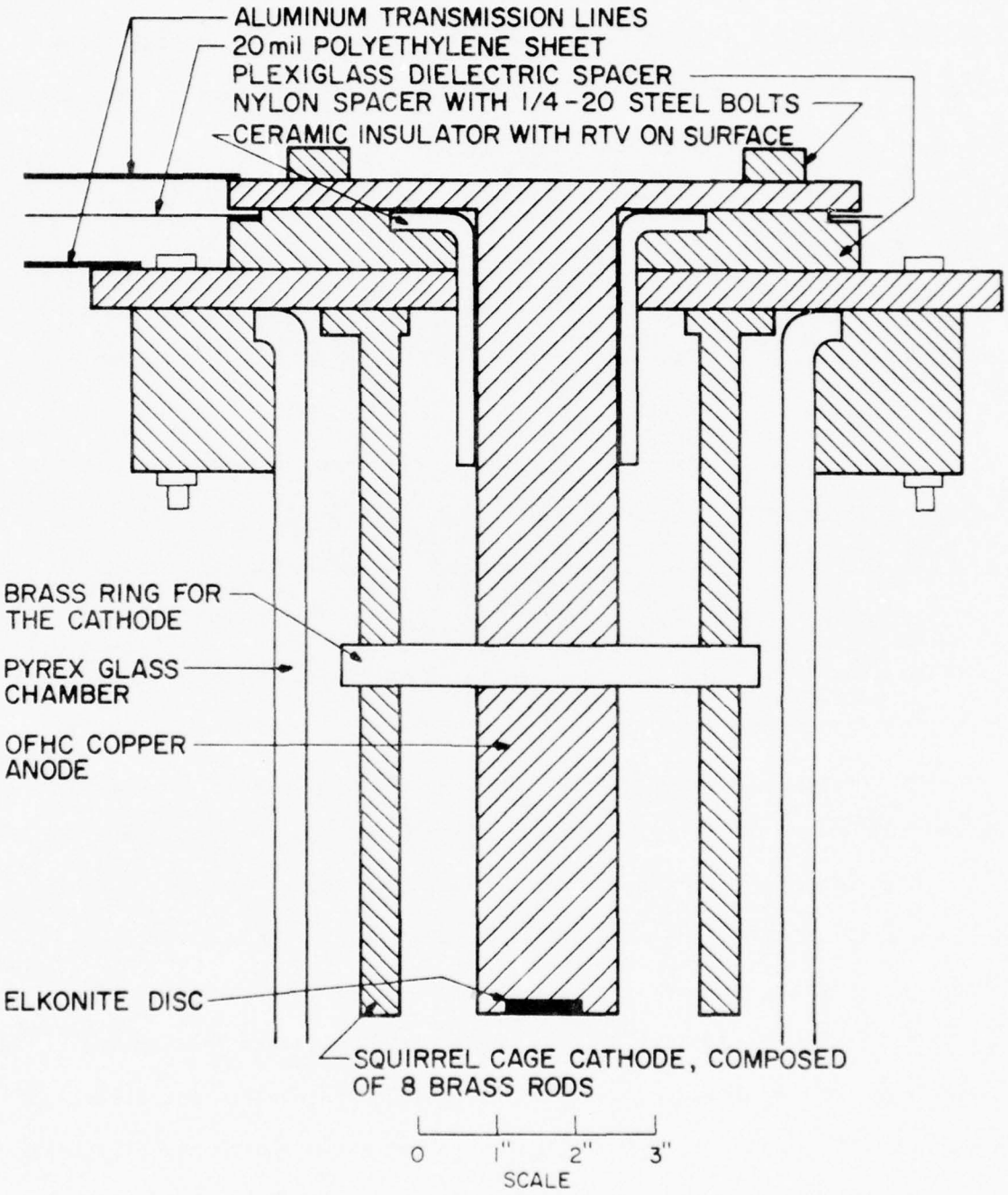

Fig. 4.16. Plasma gun.

Aluminum plates of 1/16" thick were used as transmission lines to connect the electrodes to the spark gap. A polyethylene sheet of 20-mil thickness was placed in between the two plates to prevent any electrical breakdown.

The insulator in the plasma gun provided the surface along which the electrical breakdown took place when the spark gap was switched. This surface was important to develop the parabolic shape of the current sheath, which could not be cylindrical or otherwise the focus would not be formed. An earlier design of the insulator was made of Pyrex glass about 0.1" wall thickness. The flange of the glass insulator was made by flaring out one end of the Pyrex glass tube. However, this flaring process always resulted in nonuniformity of the flange. During the electrical discharges, electrical and mechanical stresses cracked and shattered the insulator into pieces. To eliminate this problem, the insulator was made out of a new material known as grade-A lava (available from American Lava Corporation, Chattanooga, Tennessee). This material was first machined into the right shape and appropriate dimensions before it was fired. The firing process served to drive off the chemically bound water in the ceramic resulting in certain crystalline changes, and the product was then hardened. Because of these chemical changes, there was a 2 percent change in volume. The rate of heating was 200 °C/h and the ceramic material was heated at a maximum temperature of 1050 °C for 30 minutes. The final wall thickness of the insulator was over 1/4". This insulating material had a dielectric constant of 5.3 and dielectric strength 80 V/mil.

When a new ceramic insulator was put into the plasma gun assembly, experimental results showed that the focus was not successfully formed in the first ten or fifteen shots. After the gun was fired a number of times, the experimental data obtained would be consistent. It seemed that this

kind of "conditioning" of the insulator was essential to the formation of the focus. One possible explanation would be that after a number of "break-in" shots, the surface of the insulator would be conditioned enough to shape the current sheath into the required parabolic form.

Flashover was a detrimental problem to the ceramic insulator. This was due to a very high electric field at a sharp corner. The flashover would crack the insulator and then the following discharge blew the cracked insulator into powder. When this problem was identified, the space between the plexiglass and the ceramic insulator was filled with RTV (a silicone rubber product from General Electric). Since then, no cracking of the insulator due to flashover was observed.

The inductance of the plasma gun was determined by its geometry and dimensions. In Appendix A, the inductance per unit length of a gun was estimated. The total inductance of the gun in this experiment was 33.19 nH, as compared to the measured value of 31.6 nH.

4.4 Target

The targets used in this experiment were spherical balls of various materials: aluminum (Z = 13), nickel (Z = 28), OFHC copper (Z = 29), lead (Z = 82), and stainless steel Type AISI 440-C. An X-ray spectral analysis of the stainless-steel composition was shown in Fig. 4.17. The ratio of the K_α lines of chromium (Z = 24) to iron (Z = 26) was 1:2.88. The target balls had a diameter of 1 mm (obtained from the New England Miniature Ball Company, Winsted, Connecticut). The diameter tolerance of these balls was 0.00005", or the tolerance percentage was 0.125. Maximum surface roughness was within three microinches. The surface area of one of these balls was $4\pi r^2 = 1.26 \times 10^{-5}\ m^2$.

An early attempt at positioning the target within the dense focus region dropped the spherical balls into the vacuum system. A particle

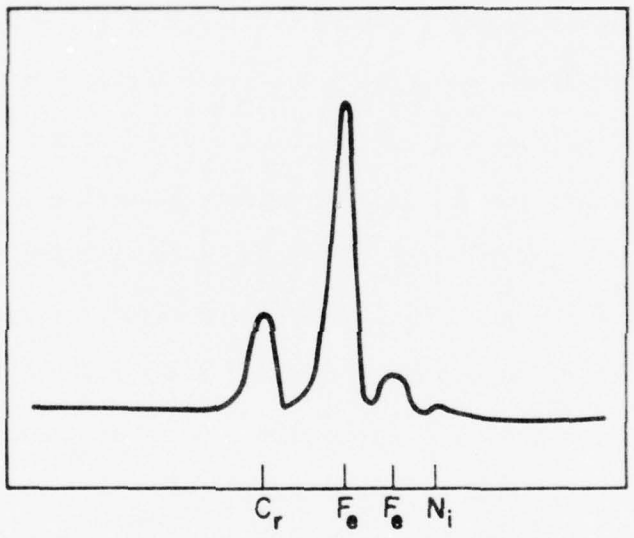

Fig. 4.17. The X-ray spectral analysis of the stainless-steel type AISI 440-C material.

launcher was designed and fabricated for this purpose (Fig. 4.18). The brass plate provided the mechanical support for the pellet reservoir and had a diameter smaller than the spacing between the clamps such that the particle launcher mounted on the plate could be positioned in the X and Y directions with 1/2" adjustments in each way. The pellet reservoir could house 30 pellets of 1 mm diameter size. A shutter made of a thin stainless-steel plate had a hole of 1.3 mm diameter and could be opened by a solenoid. A spring was attached to the shaft in the solenoid and this spring could reset the shutter after each pulse. When the shutter was opened, a pellet was dropped down the tube and passed through a set of optical detectors. An electronic circuit was designed to detect the presence of the target pellet (Fig. 4.19). A light-emitting diode, Motorola MLED 930, was placed 1/2" away from a phototransistor, Motorola MRD 450. When a particle passed in between the set of semiconductors, part of the light from the LED was blocked and thus a negative pulse of about 100 mV was generated by the phototransistor. This pulse was further amplified by the operational amplifiers to give a 5 V positive pulse. This pulse was then used to synchronize the discharge of the capacitor bank such that the pellet would be in the proper position when the dense plasma focus was formed. However, when this particle launcher was tested in the trial runs, the semiconductors were destroyed by the electromagnetic pulses from the discharges, making this approach impracticable.

A different method for positioning the particle was illustrated in Fig. 4.20. Plates with slots were used to provide adjustments of 1/2" in both X and Y directions. A threaded rod could be adjusted in the Z-direction and a brass bellow was soldered to the rod to provide the vacuum seal. The end of this rod was bolted together with an aluminum plate which

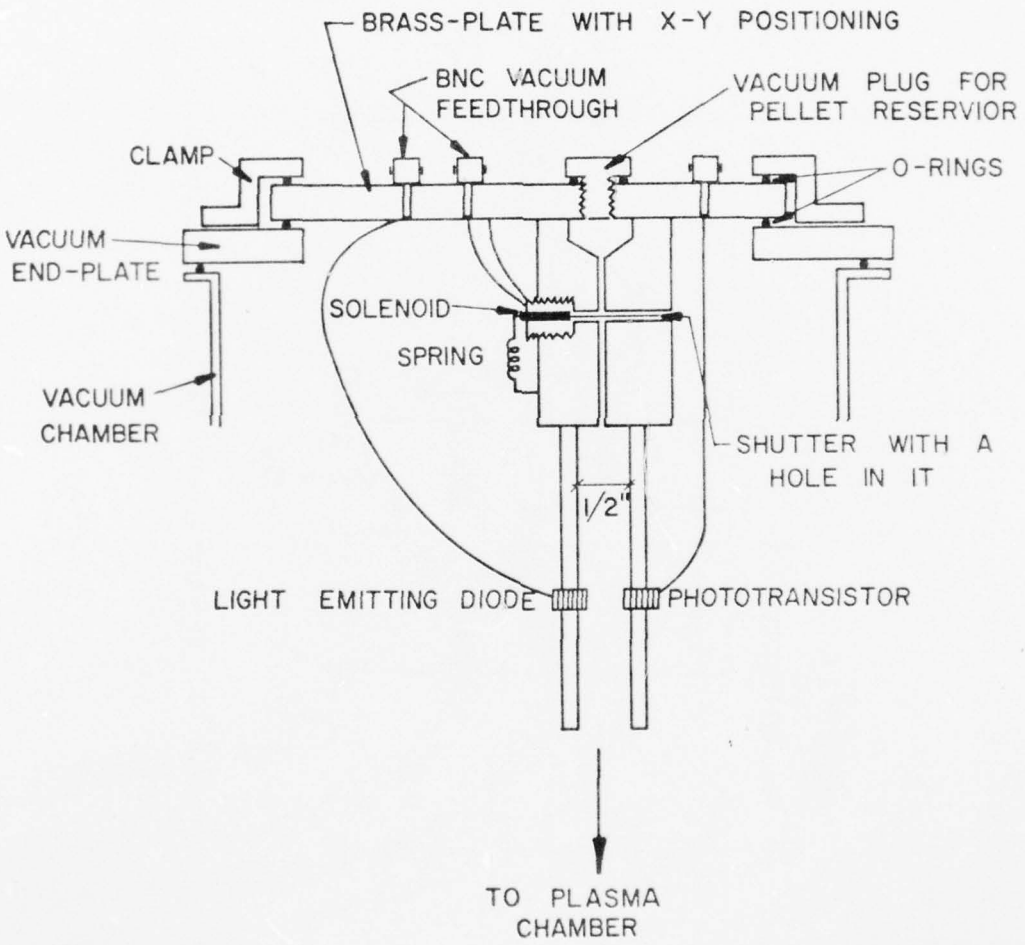

Fig. 4.18. The solid pellet launcher.

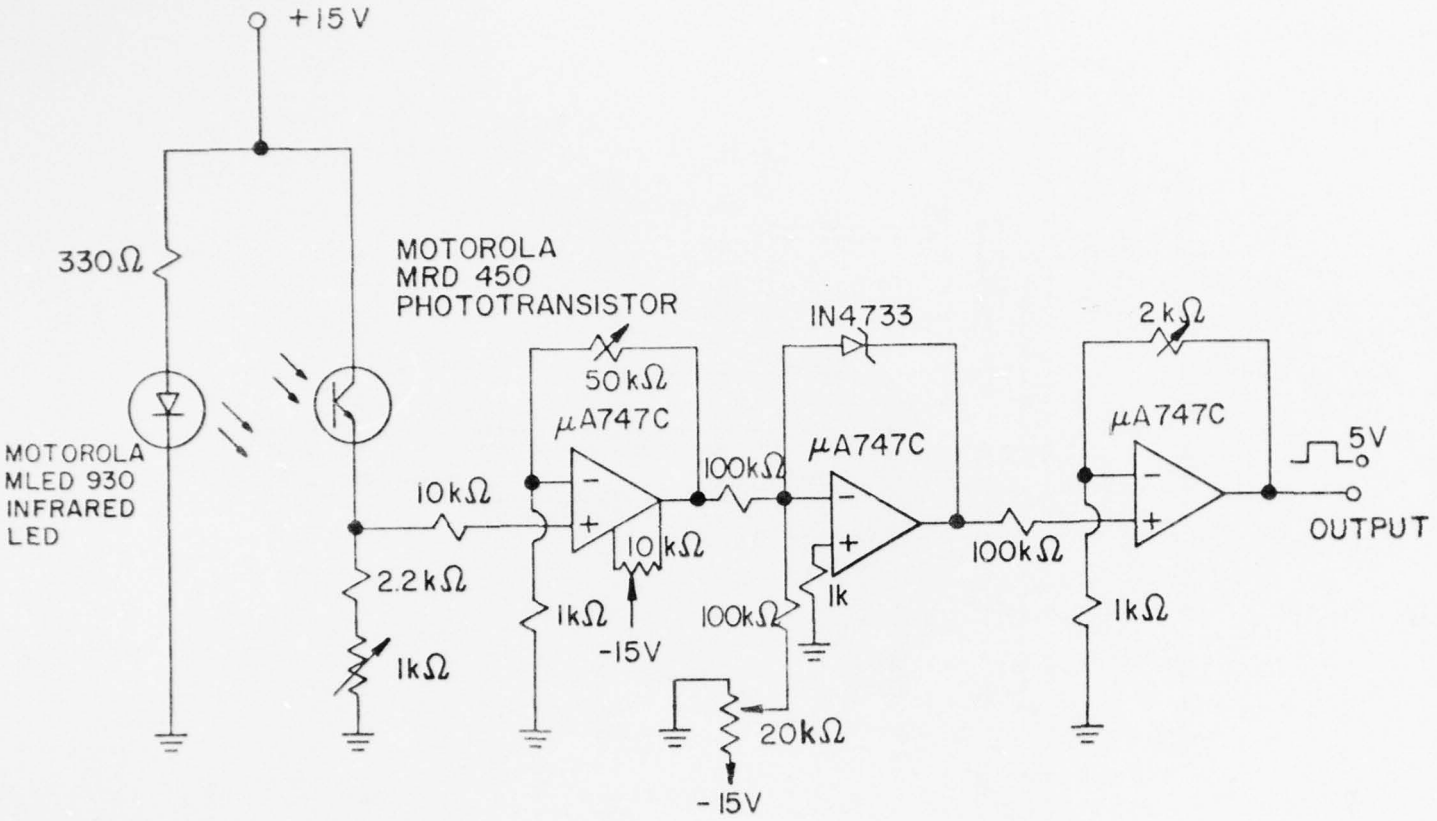

Fig. 4.19. Electronic circuit for the optical detector.

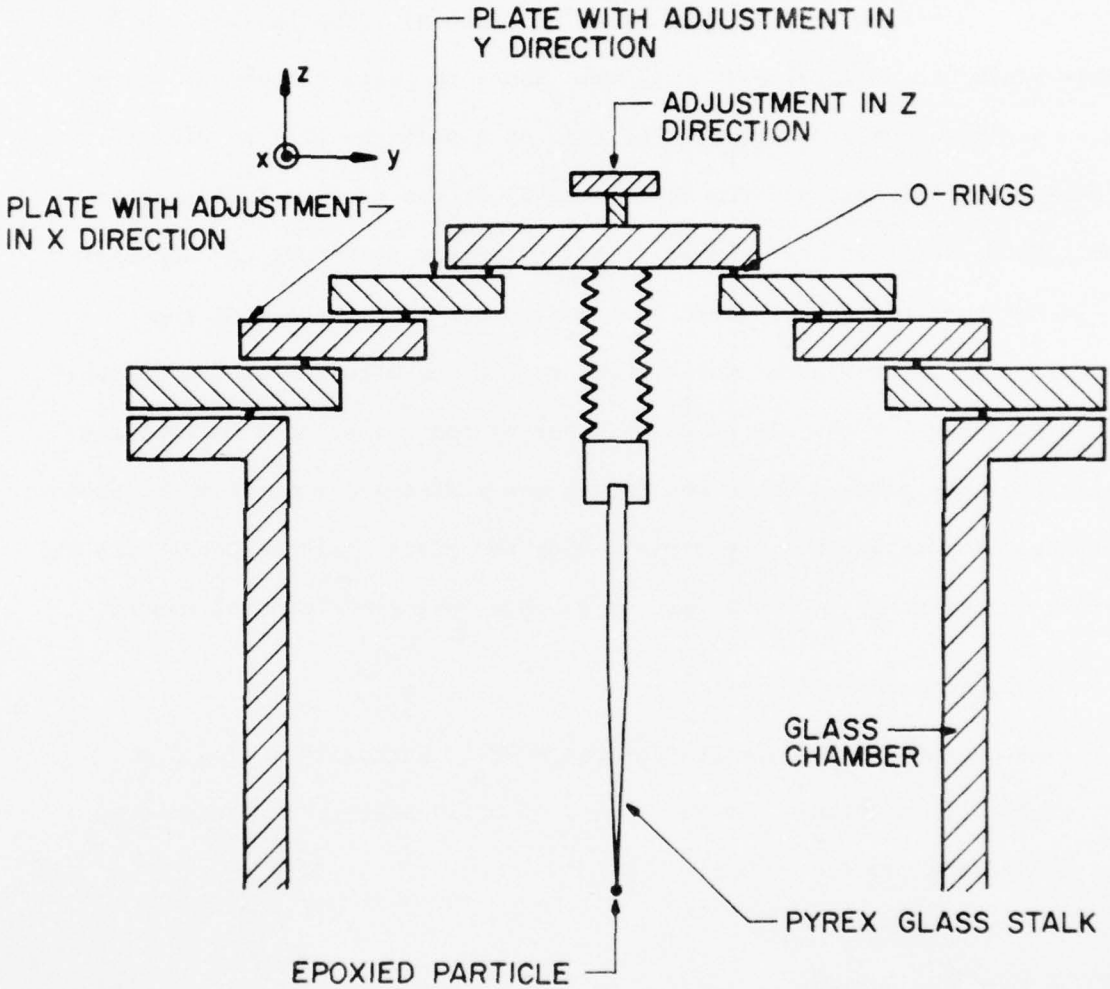

Fig. 4.20. Particle support.

was epoxied to a Pyrex glass stalk. The glass stalk was made by pulling a heated glass rod and later was cut to the required length. The target, a spherical ball, was glued to the tapered end of the stalk with as little epoxy as possible. The epoxy material used was TORR-SEAL (a low vapor-pressure epoxy from Varian, Palo Alto, California). The tapered end of the glass stalk had a diameter $\sim$ 0.12 mm. Hence the area of the end of the glass stalk was only 1.5 percent of that of a particle of 1 mm diameter. A He-Ne laser (Model 155 from Spectra-Physics) was used to indicate the particle position in the chamber. This alignment procedure was necessary to insure that all targets were in the same position throughout the experiment. The position of the focus region was measured on the optical pictures taken for the electrical discharges and was about 5 mm from the surface of the anode. Hence the target was positioned 5 mm from the anode surface. Throughout the experiment, when the glass stalk together with the target was swept away, a new target was then installed for replacement.

4.5 Diagnostic Instrumentation

The diagnostic instrumentation employed in this work included a Rogowski coil, a voltage divider, a set of solid-state X-ray detectors, and a Polaroid camera.

4.5.1 Rogowski coil

A Rogowski coil was essential to measure both the magnitude of the discharge current in the plasma and the waveform, which was important for tuning the system to obtain the focus. The basic principle of this instrument was to measure the rapidly time-varying magnetic induction associated with the large and pulsed current in the plasma. This time-changing magnetic field would generate an electromotive force $-\frac{d\phi}{dt}$, where ϕ was the magnetic flux in the coil. The Rogowski coil was shown in Fig. 4.21 and its equivalent circuit in Fig. 4.22.

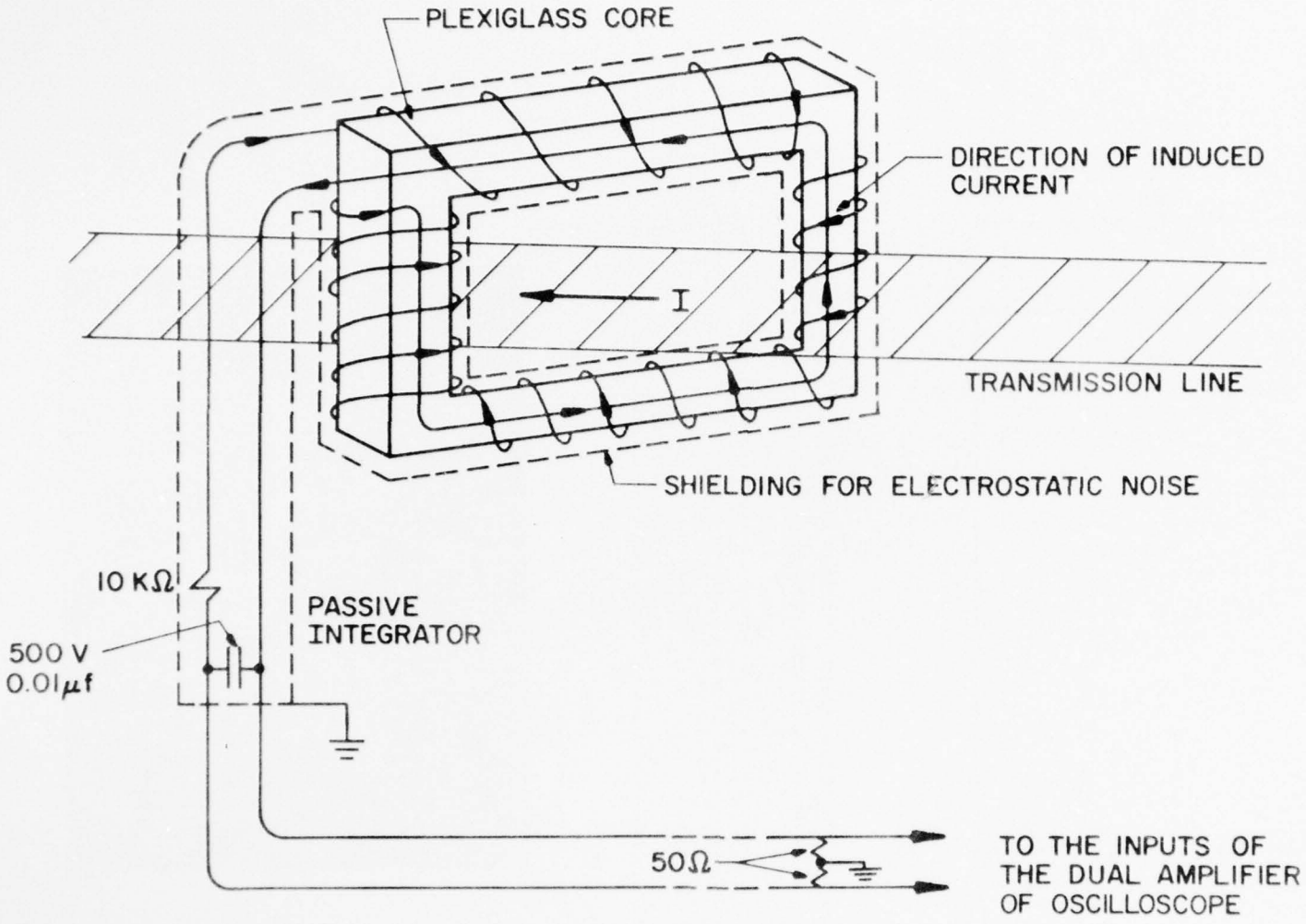

Fig. 4.21. Rogowski coil for current measurement.

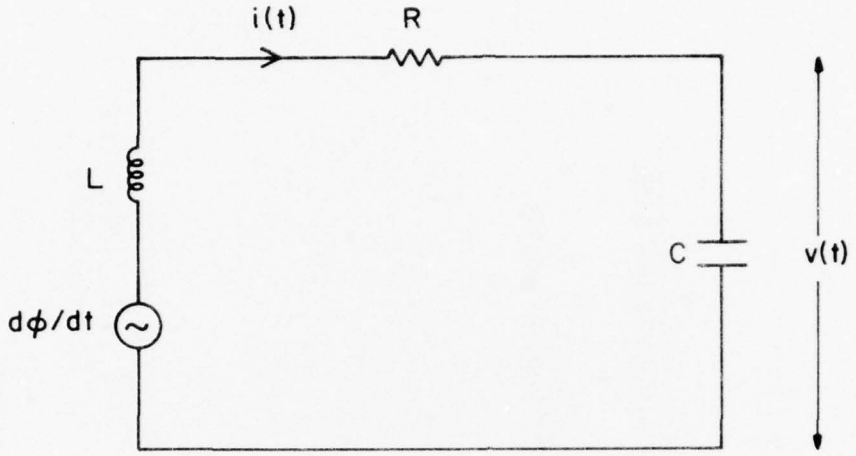

Fig. 4.22. The equivalent circuit diagram for the Rogowski coil and an RC integrator.

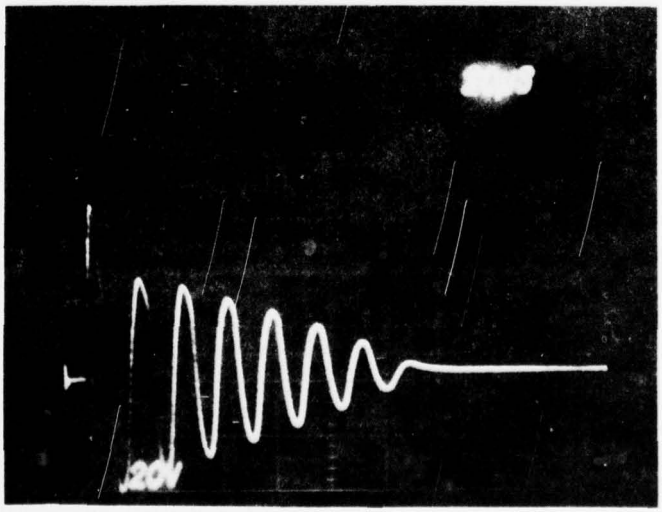

Fig. 4.23. Current waveform from a shorted capacitor for the calibration of the Rogowski coil.

In Fig. 4.22, the circuit equation was

$$\frac{d\phi}{dt} = L\frac{di}{dt} + Ri + \frac{1}{C}\int_0^t i(\tau)\, d\tau$$

where $i(\tau)$ = current flowing in the circuit

R = resistor of the integrator

C = capacitor of the integrator

L = inductance of the coil.

If $R >> \omega L$,

$$\frac{d\phi}{dt} \approx Ri + \frac{1}{C}\int_0^t i(\tau)\, d\tau$$

where ω = highest significant frequency component of ϕ and for $t << RC$,

$$i(t) \approx \frac{1}{R}\frac{d\phi}{dt} \quad .$$

Therefore, the output voltage was essentially

$$v(t) = \frac{1}{C}\int_0^t i(\tau)\, d\tau = \frac{\phi(t)}{RC} \quad . \tag{4.1}$$

As the magnetic flux was proportional to the main current I(t),

$$\phi(t) = KnI(t) \tag{4.2}$$

where n = number of turns of the wire on the coil

K = constant depending on the geometry of the coil and the current distribution.

Combination of Eqs. (4.1) and (4.2) gave

$$v(t) = \frac{Kn}{RC}\, I(t) \tag{4.3}$$

or

$$v(t) = K'I(t) \tag{4.4}$$

where K' = new proportional constant of the coil and the integrator.

The above conditions required that $R >> \omega L$ and $t << RC$. These indicated large values for R and C. However, Eq. (4.3) showed that the output voltage signal was inversely proportional to the RC product and hence compromised values of R and C must be chosen.

In this experiment, the core of the Rogowski coil was made of plexiglass which essentially had the relative permeability of 1. Thirty-three turns of gauge number 30 wire were evenly spaced around the core. One end of the coil winding wire was threaded back through the turns of the coil to the initial end so that the flux which threaded the major opening of the core would not thread any portion of the measuring circuit. This arrangement would insure that the signals measured were only due to those currents passing through the core. On top of the wire, copper tapes were used to wrap around the core but a slit was cut longitudinally along the copper layer so as to eliminate any induced current in the tapes. This layer of copper was grounded and functioned as an electrostatic shielding against any possible capacitive coupling to large voltage fluctuations. Twenty-mil thick teflon tapes were put on top of the copper to provide electrical insulation between the grounded copper shielding and the current-carrying transmission line. An integrator which consisted of a resistor and a capacitor was chosen to satisfy the design criteria and was housed in a grounded box. The output voltage from the capacitor was transmitted by two coaxial cables to the inputs of a dual amplifier on the Tektronix oscilloscope, Type 555. Both inputs were terminated with 50 Ω resistors to match the characteristic impedance of the cables.

The inductance of the Rogowski coil was given by

$$L = \frac{\mu_0 n^2 A}{S} \tag{4.5}$$

where μ_0 = permeability of free space

A = cross-sectional area of the core

S = axial length of the core.

The physical dimensions were

$$\mu_0 = 4\pi \times 10^{-7} \text{ H/m}$$

$$A = 8.0645 \times 10^{-5} \text{ m}^2$$

$$S = 4.51 \times 10^{-1} \text{ m}$$

$$n = 33$$

$$\therefore L = 0.2448 \times 10^{-6} \text{ H} \quad .$$

The period of the interested signal was T = 2 μsec or $\omega = \frac{2\pi}{T} = \pi \times 10^6$

$$\therefore \omega L = 0.769 \quad .$$

R was picked to be 10 kΩ and C as 0.01 μF at 500 V. Or, $RC = 10^{-4}$. Therefore, $R >> \omega L$ and $RC >> T$ were satisfied.

Calibration of the Rogowski Coil

The Rogowski coil was calibrated by using it to measure the shorted current from a capacitor of known capacitance C, and charged to known voltage V. The current waveform was then displayed on a storage oscilloscope. A typical waveform was shown in Fig. 4.23. The ringing period, T, was due to the inductance and capacitance of the capacitor. From Fig. 4.23,

$$I(t) = I_0 \sin \omega t$$

and

$$v(t) = v_0 \sin \omega t \quad .$$

Therefore,

$$K' = \frac{v_0}{I_0} \quad . \tag{4.6}$$

Equating the total charge on the capacitor to the charge discharged in half-period,

$$Q = CV = \int_0^{T/2} I_0 \sin \omega t \, dt = \frac{I_0 T}{\pi}$$

or

$$I_0 = \frac{CV\pi}{T} \, . \tag{4.7}$$

As T and v_0 were measured from Fig. (4.23), and knowing C and V, K' could be calculated from Eqs. (4.6) and (4.7).

4.5.2 Voltage divider

In order to measure the high-voltage pulses associated with the plasma discharges, a voltage divider was required to attenuate the magnitude of such pulses to a value safe enough for the oscilloscope on which the voltage waveforms were displayed. In this work, a capacitive divider was designed for this purpose because an "open" input impedance was required to prevent loading of the circuit being monitored. This capacitive divider measured the voltage waveform at the breech of the plasma gun and was clipped on the transmission lines such that the divider elements were placed immediately at the measurement sensing location. Such an arrangement was necessary to achieve an "open" input impedance without reflection distortions due to input cable under fast pulse conditions.

Figure 4.24 showed the capacitive divider employed in this experiment. The central copper rod, the teflon dielectric, and the floating brass cylinder formed the high-voltage capacitor, C_1. The floating cylinder, the 3-mil mylar sheet, and the grounded brass electrode formed the low-voltage capacitor, C_2. These two capacitors were constructed in shielded coaxial type to reduce noise induction from the high-power pulse circuit. Teflon and mylar were used as the dielectrics because of their low voltage and

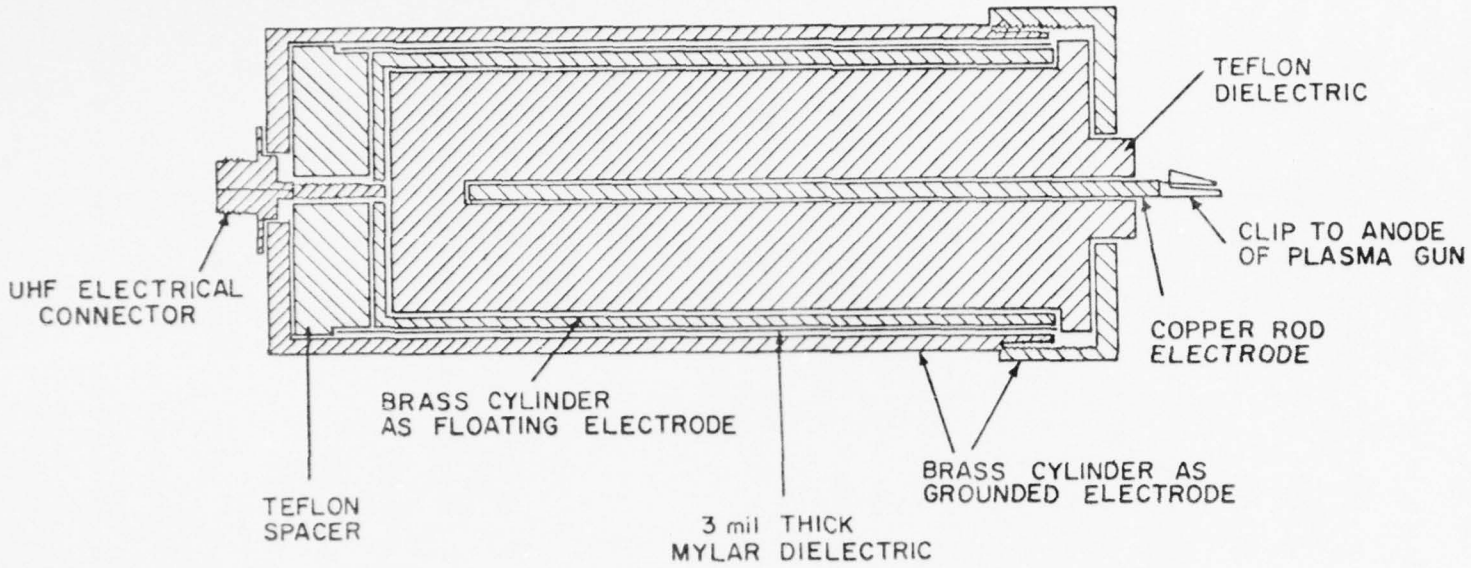

Fig. 4.24. Coaxial voltage divider.

temperature coefficients, and independence of frequency. These dielectric properties were ncessary to preserve the best risetime response and to avoid any large scale shifts in the attenuation factor.

The input and output connections of this capacitive divider were shown in Fig. 4.25. The output voltage signal from the floating electrode was fed into a resistor R_0 (50 Ω), equal to the characteristic impedance Z_0 of the cable which transmitted the signal to the oscilloscope. This matching technique permitted only one reflection for fast pulses, during which time the cable looked like a resistor equal to its characteristic impedance and then appeared as a capacitor. The attenuation factor of this capacitive divider was:

$$\text{Attenuation factor} = \frac{\text{input voltage}}{\text{output voltage}} = \frac{C_1 + C_2}{C_1}$$

C_1 = high-voltage capacitor

C_2 = low-voltage capacitor.

Using the coaxial cylindrical capacitor approximation, the estimated values for C_1 and C_2 were 14.1 pF and 6.59 nF, respectively. The experimental values of C_1 and C_2 at 500 kHz were 14 pF and 6.6 nF, respectively, as measured with a vector impedance meter (Model 4800A, by Hewlett-Packard). Hence, the attenuation factor of this divider was 472.43.

4.5.3 X-ray detector

A solid-state semiconductor has several advantages over other radiation detectors for X-rays. Taylor [37] and Dearnaley [38] suggested that the semiconductors have these advantages:

(1) higher resolution because the photon energy required to produce an ion-electron pair is much lower than that for other detectors,

(2) linear response over a larger energy range,

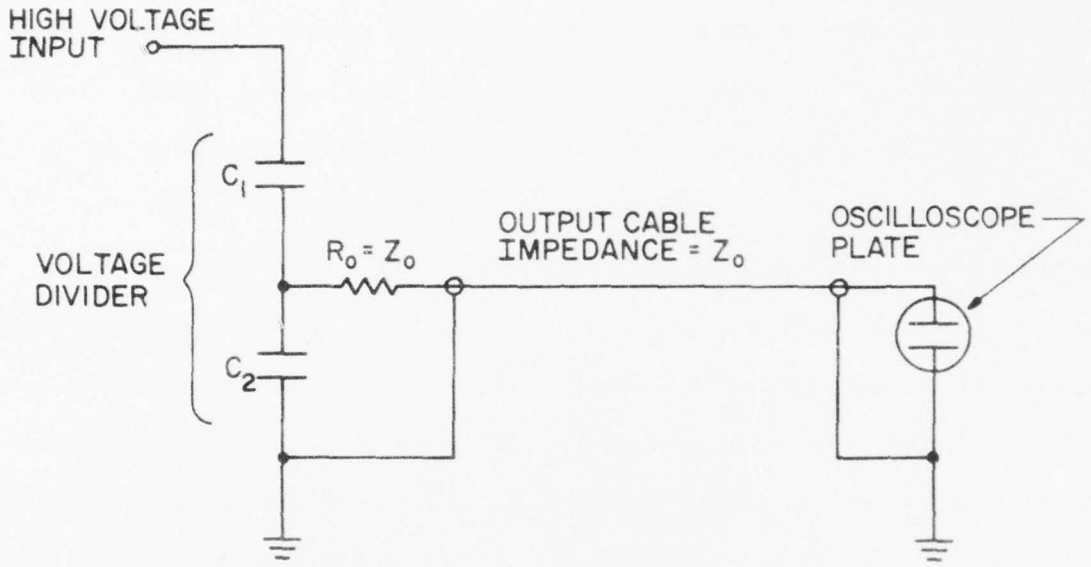

Fig. 4.25. Schematic diagram of the connections of the capacitive voltage divider.

AD-A037 354 ILLINOIS UNIV AT URBANA-CHAMPAIGN CHARGED PARTICLE RE--ETC F/G 20/9
X-RAY EMISSION FROM THE INTERACTION OF A MACROSCOPIC PARTICLE W--ETC(U)
OCT 76 K F YEUNG, C D HENDRICKS AF-AFOSR-2643-74
UNCLASSIFIED CPRL-1-76 AFOSR-TR-77-0130 NL

2 OF 2
AD A037 354

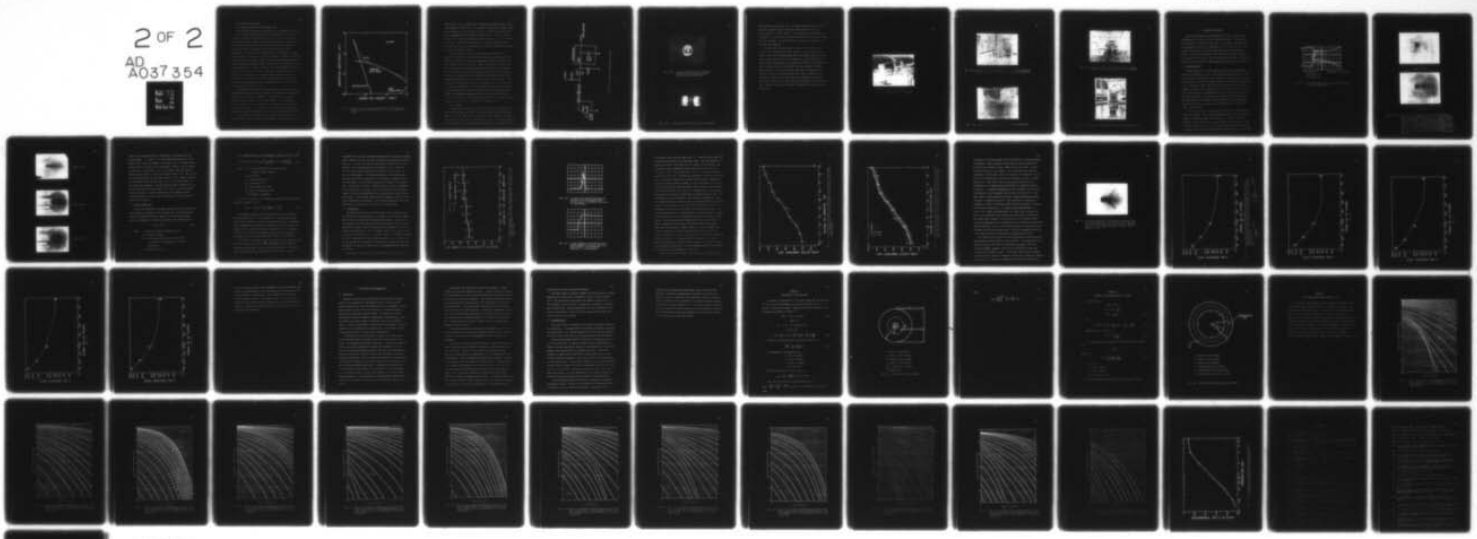

END

DATE FILMED
4-77

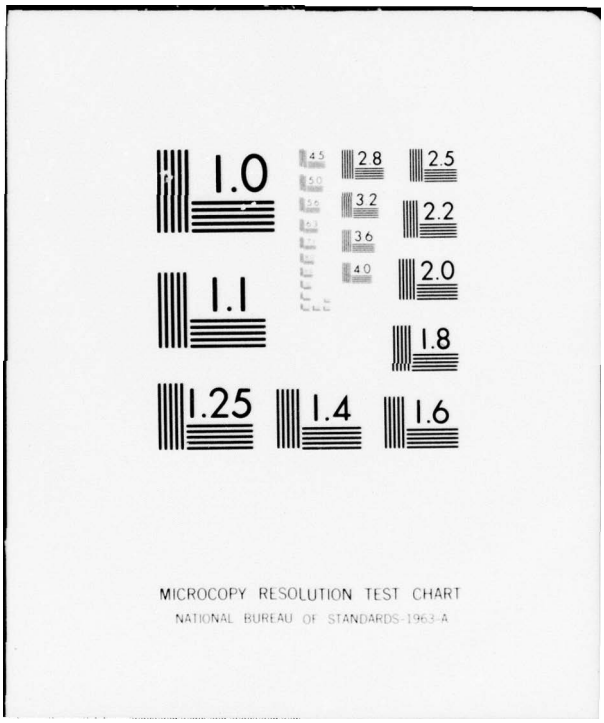
1.0
1.1
1.25
1.4
1.6
1.8
2.0
2.2
2.5
2.8
3.2
3.6
4.0
4.5
5.0
5.6
6.3
MICROCOPY RESOLUTION TEST CHART
NATIONAL BUREAU OF STANDARDS-1963-A

(3) faster pulse risetime,

(4) relative simplicity and convenient size,

(5) and higher density which enables them to stop energetic particles.

In the energy range between a few keV to 50 MeV, most of the interactions of X-rays with matters are due to one of the three processes: photoelectric effect, Compton effect, and pair production. In Fig. 4.26, the absorption coefficients of silicon due to different processes are plotted vs. energy. At energy below 50 keV, photoelectric effect predominates. In this process, a photon gives all its energy to a bound electron, which uses part of the energy to overcome its binding to the atom and takes the rest as kinetic energy. The electron-hole pair generated is then collected by an applied electric field across the p-n junction of the semiconductor, and an electrical pulse is obtained proportional to the energy lost by the photon. Because of the high excitations that can be produced by the collisions, the average energy required to produce an electron-hole pair is greater than the energy separation of the bands. For silicon the average energy per electron-hole pair is 3.66 eV and the energy separation is only 1.11 eV.

The semiconductor used as a pulsed X-ray detector in this work was a double-diffused PIN silicon detector (Model No. 100-PIN-125, from Quantrad Corporation, Los Angeles, California). This detector had an area of 100 mm^2; sensitive depth 125 μm; entrance window ∿ 1 μm; and negative biasing voltage of 200 V. According to the manufacturer's specification sheet, the efficiency of this detector was at maximum value for photon energy below 10 keV and dropped to only 1 percent for energy above 45 keV.

In the experiment, two detectors were placed side by side in the plasma chamber. Each semiconductor was monitored by an electronic circuit,

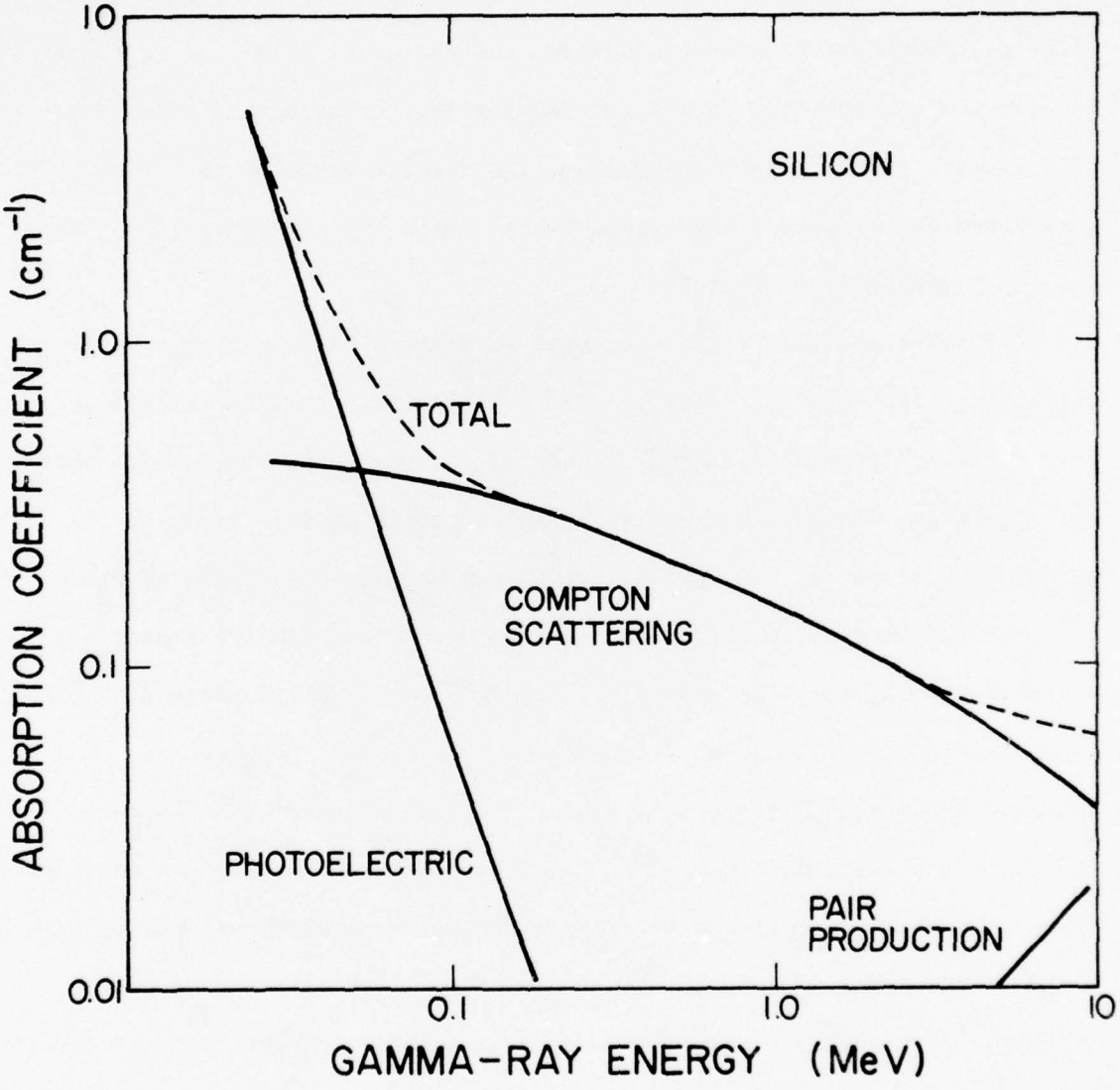

Fig. 4.26. Partial and total absorption coefficients for gamma rays in silicon, from data in Grodstein, G. W., N.B.S. Circular 583 (1957).

shown in Fig. 4.27. A negative 200 V supplied the biasing voltage to the semiconductors, and the 1 kV, 0.1 μF capacitor blocked this biasing voltage from the input of the oscilloscope. The 50 Ω resistor matched the cable which transmitted the signal pulse from the detector. The 1 kΩ resistor and the 2.2 μF capacitor formed the passive integrator with a time constant of 2.2 msec. Without this integrator, the circuit measured the time-resolved X-ray output of the plasma focus. With the integrator, the signal was the time-integrated output.

Different metallic foils were used as filters for the X-ray detectors. The metallic foils used were beryllium, aluminum, nickel and gold (obtained from A. D. Mackay Incorporated, New York, New York). The foil thickness was only a few mils. These foils placed in front of the detectors blocked off the optical light from the focus and also shielded the semiconductors from any eroded materials emitted from the plasma gun electrodes. Figure 4.28a showed a damaged detector with a two-mil thick aluminum filter which was used in the trial runs of the experiment. This detector was placed along the axis of the plasma gun and at a distance of 4.5' from the anode surface. The eroded materials from the gun electrodes pierced through the foil and were deposited on the semiconductor surface. Figure 4.28b compared a damaged semiconductor (left) with a good one (right). In order to avoid such damages, the detectors were then placed at 90° to the gun axis and at a distance of 6" from the axis.

4.5.4 Camera

A Polaroid Land camera, Model 195, and Polaroid black-and-white film Type 107, speed 3000, were used to take the optical pictures of the dense plasma focus. The camera was set next to the plasma chamber and focused at the plasma gun anode surface. Neutral density filters up to neutral density 16 were stacked on the camera lens such that the optical emissions from the

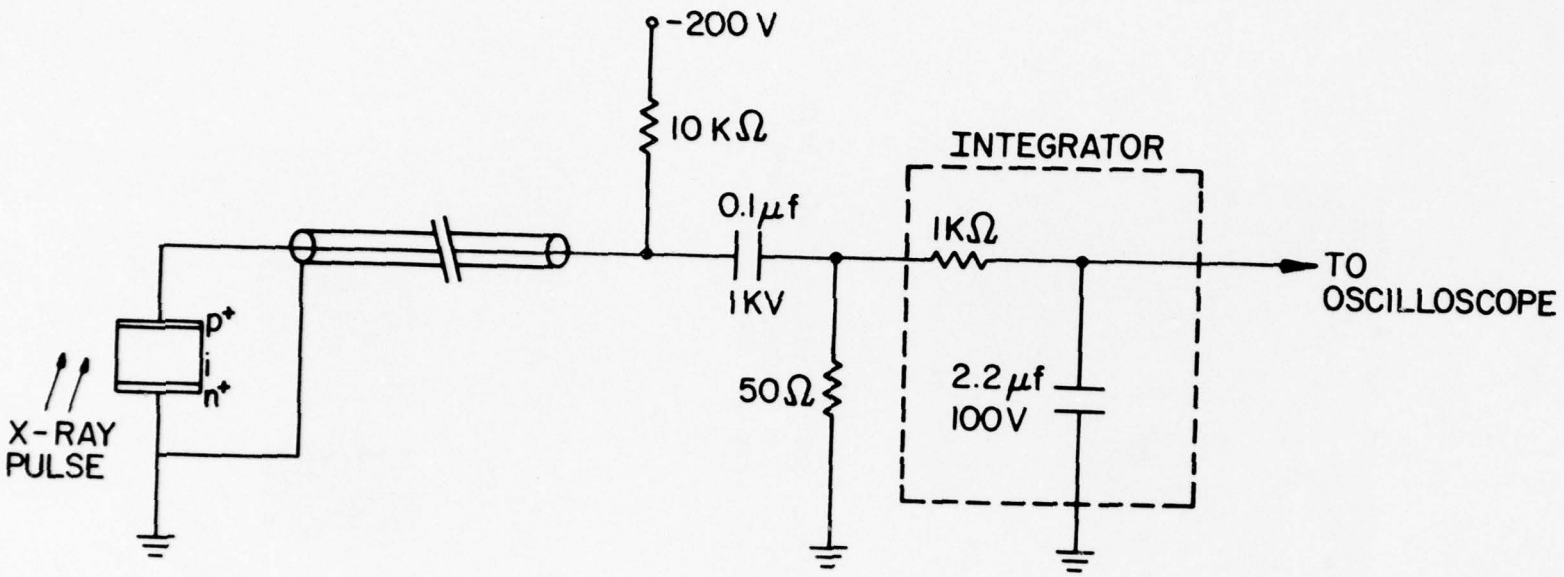

Fig. 4.27. Circuit for measuring x-ray pulses.

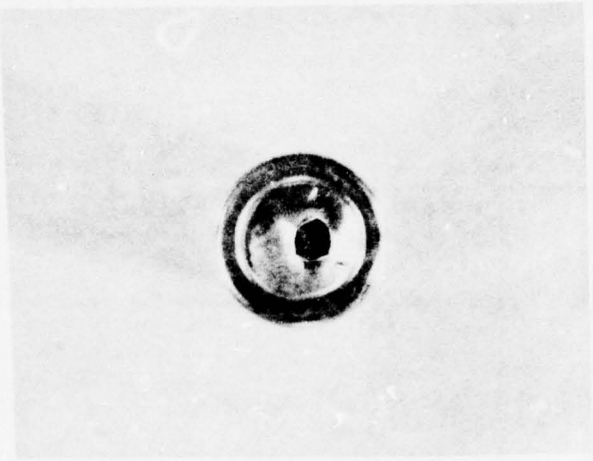

Fig. 4.28a. A silicon detector with a 2 mil thick aluminum filter, damaged by eroded materials from gun electrodes.

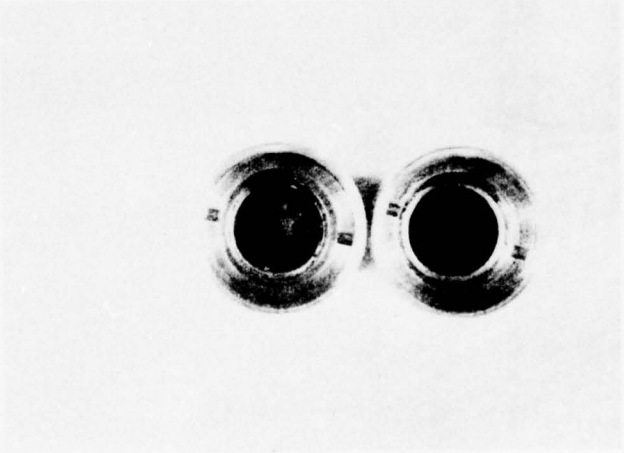

Fig. 4.28b. A damaged detector (left) and a good one (right).

focus would not saturate the film. The camera shutter was set at the B mode and a pneumatic cable release was used to manually control the picture taking at a remote distance. The camera shutter was opened only a fraction of a second before the capacitor bank was fired and closed right after the discharge. The optical pictures of the focus obtained in this way were time-integrated.

The experimental instrumentation is shown in Figs. 4.29 to 4.33. In Fig. 4.29, the high-voltage power supply is in the background, the capacitor bank and the plasma chamber are in the middle, and the overhead cables lead to the screen room for diagnostics. Figure 4.30 shows the capacitor bank and the spark gap connected to the head of the plasma gun and the voltage divider at the breech of the gun. Figure 4.31 shows a wooden box built to cover the capacitor bank when the experiment was running. This was a precaution against any possible explosion of the capacitors. Figure 4.32 is a top view of the plasma gun at the breech. The voltage divider is on the left side and the Rogowski coil on the right side. Figure 4.33 shows the electronic instrumentation housed inside the screen room.

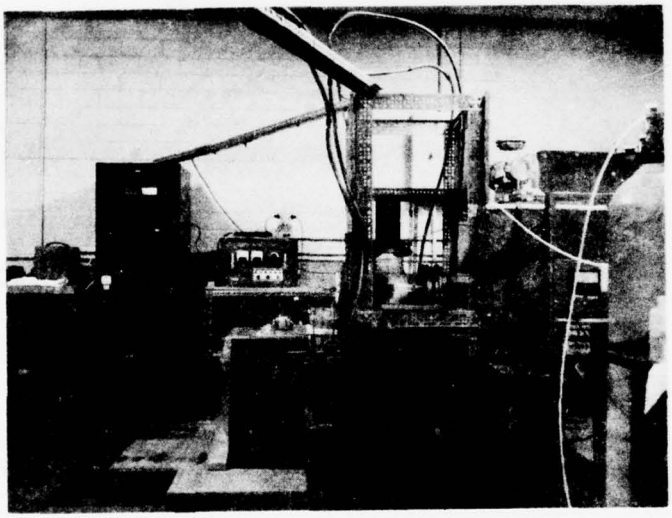

Fig. 4.29. Dense plasma focus experiment.

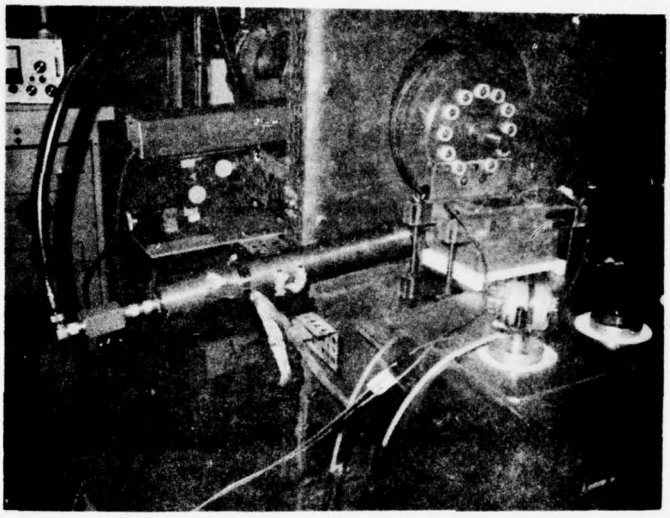

Fig. 4.30. Connections of the spark gap with the head of the plasma gun and the capacitor bank. The voltage divider is on the left.

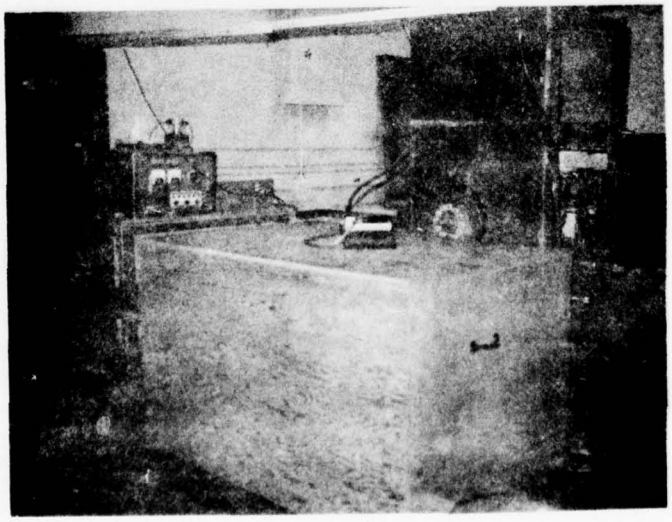

Fig. 4.31. Capacitor bank covered with wooden box during operation.

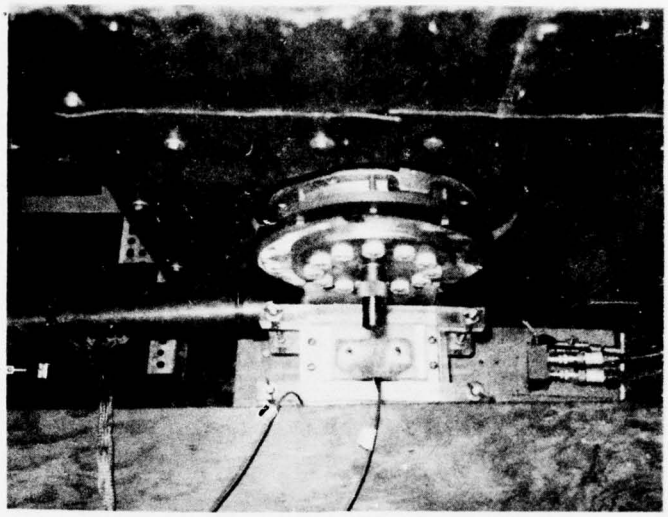

Fig. 4.32. Top view of the breech of the plasma gun. Voltage divider on the left and Rogowski coil on the right.

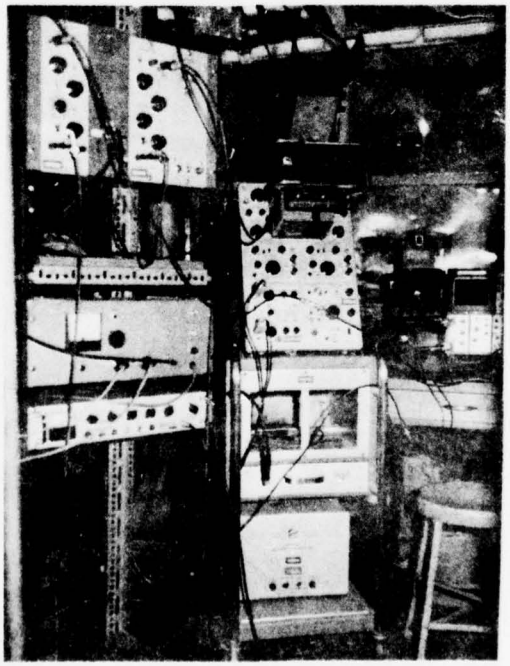

Fig. 4.33. Electronic instrumentation housed inside the screen room.

5. RESULTS AND ANALYSIS

Like any other plasma focus experiment [11], [12], [15], [23], the reproducibility of the data in this experiment was poor. Occasionally, the shot-to-shot variation was very large. In this work, ten data points were obtained for each set of conditions, but, out of the ten, only five points with the higher values were used in analyzing the experimental results. This was done because we were interested in changes in maximum X-ray yields from the focus. These five points were averaged to obtain the mean value, and the spread of these points was represented by an error bar.

5.1 System Operation

Various factors like voltage, pressure, inductance and capacitance affect the formation of a focus. These parameters were adjusted to obtain the focus while a Rogowski coil and a capacitive voltage divider were used to measure the current and voltage waveforms of the discharge, respectively. Fig. 5.1 shows the current (upper trace) and voltage (lower trace) waveforms of the plasma focus, operating at 1 torr pressure and at 19 kV. The dip in the current was accompanied with a voltage spike and occurred when the focus was formed. The decrease in current was due to pinching, and the large change of inductance with time accounted for the voltage spike. The discharge current, measured by the calibrated Rogowski coil, was $\sim 400 \times 10^3$ A at 19 kV.

In the trial runs, the focus machine was operated at various pressure levels and voltages. For the machine employed in this work, the focus was formed in the pressure range from $\sim$ 0.5 torr to $\sim$ 2 torr. The time-integrated optical pictures of the dense plasma focus were taken by using a Polaroid camera, Fig. 5.2 a-e. All five pictures were taken at the same f - number, f/45, with total neutral density filters N.D.16. The streaking

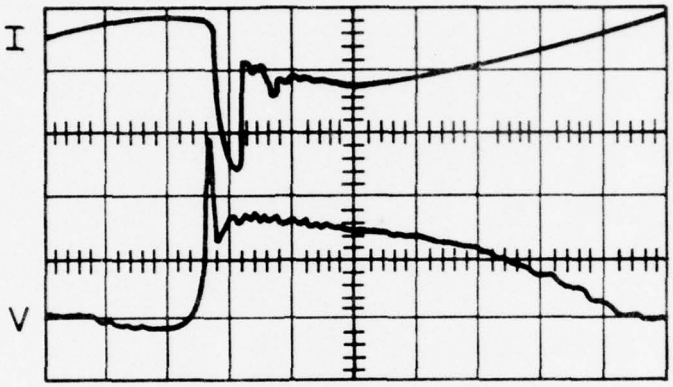

Vertical scale:
5 V/division for I
50 V/division for V

Time scale: 0.5 V/division

Fig. 5.1. The current (upper) and voltage (lower) waveforms of the dense plasma focus.

Fig. 5.2 (a).

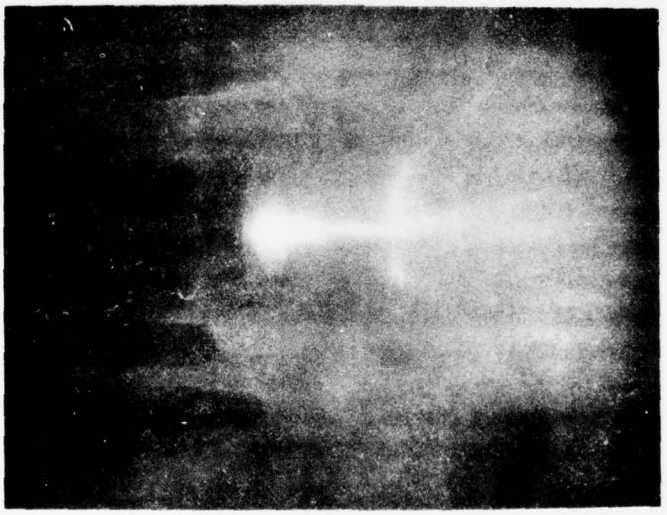

Fig. 5.2 (b).

Fig. 5.2 a-e. Time-integrated optical pictures of the DPF, taken by a Polaroid camera. Plasma gas : H_2 + 4.7% Argon. The flare in the picture was due to refraction at the glass wall of the plasma chamber. (a) & (b) operating voltage at 9 kV, pressure 1 torr; (c) voltage at 12 kV, pressure 1 torr, (d) voltage at 16 kV, pressure 1 torr; (e) voltage at 16 kV, pressure at 3.5 torr. The optical pictures show that the higher the voltage, the better the focus formation. At 9 kV, Fig. (a) & (b), the focus was formed sporadically. In Fig. (e), the pressure was high, at 3.5 torr, and no focus was formed.

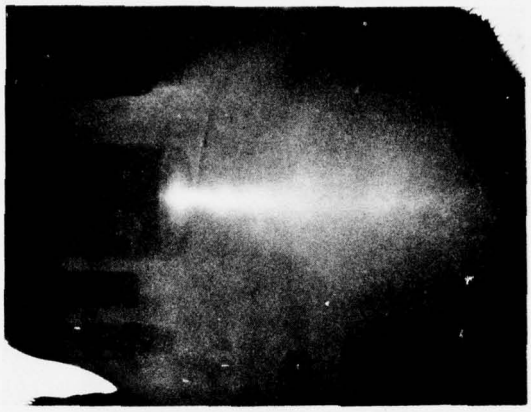

Fig. 5.2 (c).

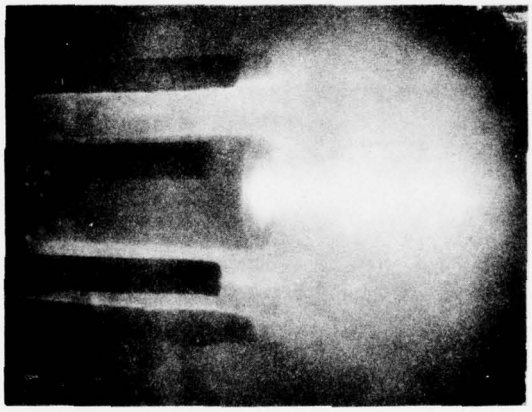

Fig. 5.2 (d).

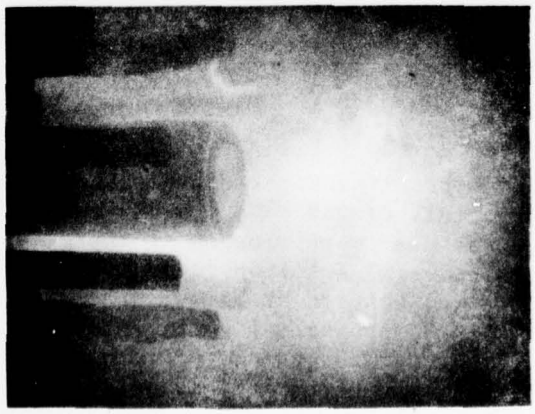

Fig. 5.2 (e).

lines in the pictures were due to refraction at the glass wall of the plasma chamber. In Figs. 5.2 a-d, the machine was operated at 1 torr pressure and a focus was obtained. But in Fig. 5.2e, the plasma chamber pressure was 3.5 torr and no focus was formed. Instead, only a discharge was observed. In both Figs. 5.2a, b, the coaxial tubes were operated under the same pressure, 1 torr, and the same voltage, 9 kV. But the focus was formed sporadically at this lower voltage. As the voltage, or energy, of the capacitor bank increased, Figs. 5.2c, d, the focus seemed to be more stable and consistent. The total optical output, as observed in the pictures, increased with the voltage. The trial-run results indicated that the best data, in terms of consistency, were obtained when the pressure level was $\sim$ 1 torr. Hence, all the data in this work were obtained at this pressure.

5.2 Electron Temperature

The electron temperature of a dense plasma focus can be estimated by measuring the X-ray emission from the plasma with X-ray detectors with filters of different thickness. When an X-ray beam passes through a filter, its intensity is attenuated according to the exponential law

$$I/I_0 = e^{-\xi(\lambda)x} \tag{5.1}$$

where I = intensity transmitted through the foil

I_0 = incident intensity

$\xi(\lambda)$ = absorption coefficient of the foil and is a function of the wavelength of the incident photon

x = thickness of the foil.

For a thermal plasma, the electromagnetic emission is given by [39]

$$dI(\lambda) = 6.01 \times 10^{-30}\, gN_e \sum_i \left(n_i Z^2\right) T_e^{-1/2}\, \lambda^{-2} \exp\left(-\frac{12.4}{\lambda T_e}\right) \qquad (5.2)$$

where $dI(\lambda)$ = power emitted per unit volume at wavelength λ, W/cm^3 -angstrom

g = Gaunt factor

n_e = electron density, cm^{-3}

n_i = ion density, cm^{-3}

Z = atomic number of the ions

T_e = electron temperature in keV

λ = wavelength in angstroms.

If Eqs. (5.1) and (5.2) are combined, the intensity of the radiation transmitted through a foil is

$$dI(\lambda) \propto \lambda^{-2} \left(T_e\right)^{-1/2} \exp\left[-\frac{12.4}{\lambda T_e} - \xi(\lambda)x\right] . \qquad (5.3)$$

A numerical integration of Eq.(5.3) was performed by Elton [40] at the Naval Research Lab., CDC 3870 computer over a photon energy range from 0.1 keV to 1000 keV for various electron temperatures. A normalized total transmission is obtained by the integral of Eq. (5.3) divided by the integral over the incident Bremsstrahlung radiation ($x = 0$), Appendix C. A ratio of the normalized transmissions through filters of different thicknesses is plotted against temperature in Fig. C-13, Appendix C.

In this work, two silicon detectors were placed side by side and were covered by beryllium filters of 2 $\left(9.6\ mg/cm^2\right)$ and 5 $\left(24\ mg/cm^2\right)$ mil thicknesses, respectively. These beryllium windows shut off the optical light from the detectors and also attenuated the X-rays. The time-

integrated X-ray signals from these detectors were only relative in magnitudes. However, the ratio of these two signals was compared with those in Fig. C-13. At 19 kV, the value of the ratio was between 0.532 to 0.617. Therefore, the corresponding electron temperatures were 1.06 keV and 1.45 keV, and the mean temperature was estimated to be 1.15 keV. In Fig. 5.3, both graphs of the electron temperature of the dense plasma focus and the electron temperature of a lead particle, diameter 1 mm, in the dense plasma focus were plotted against the voltage of the capacitor bank. In this figure, there is a slight increase in electron temperature as the bank energy is increased. But the two curves show no noticeable change in the electron temperature when a lead particle is placed in the focus region. The variations between the two temperature curves are well within experimental uncertainties. The electron temperature is the same regardless of the presence of a particle in the focus region.

5.3 X-ray Results

The silicon detectors and the filters used in this experiment were not calibrated on an absolute scale. Therefore, only the relative magnitudes of the X-ray emissions were measured and compared. Because of the fast response of the semiconductors and the oscilloscope used, the time-resolved X-ray pulses could be measured with the arrangement in Fig. 4.27 without the RC integrator. Fig. 5.4a shows a typical X-ray pulse detected by a silicon detector with a 2-mil beryllium filter. The operating voltage was 16 kV. The duration of this pulse was about 0.5 usec. In Fig. 5.4b, the time-integrated X-ray pulse is displayed and its magnitude represents, relatively, the total X-ray emitted for all wavelengths and the life time of the focus.

The relative X-ray output from a dense plasma focus is plotted vs.

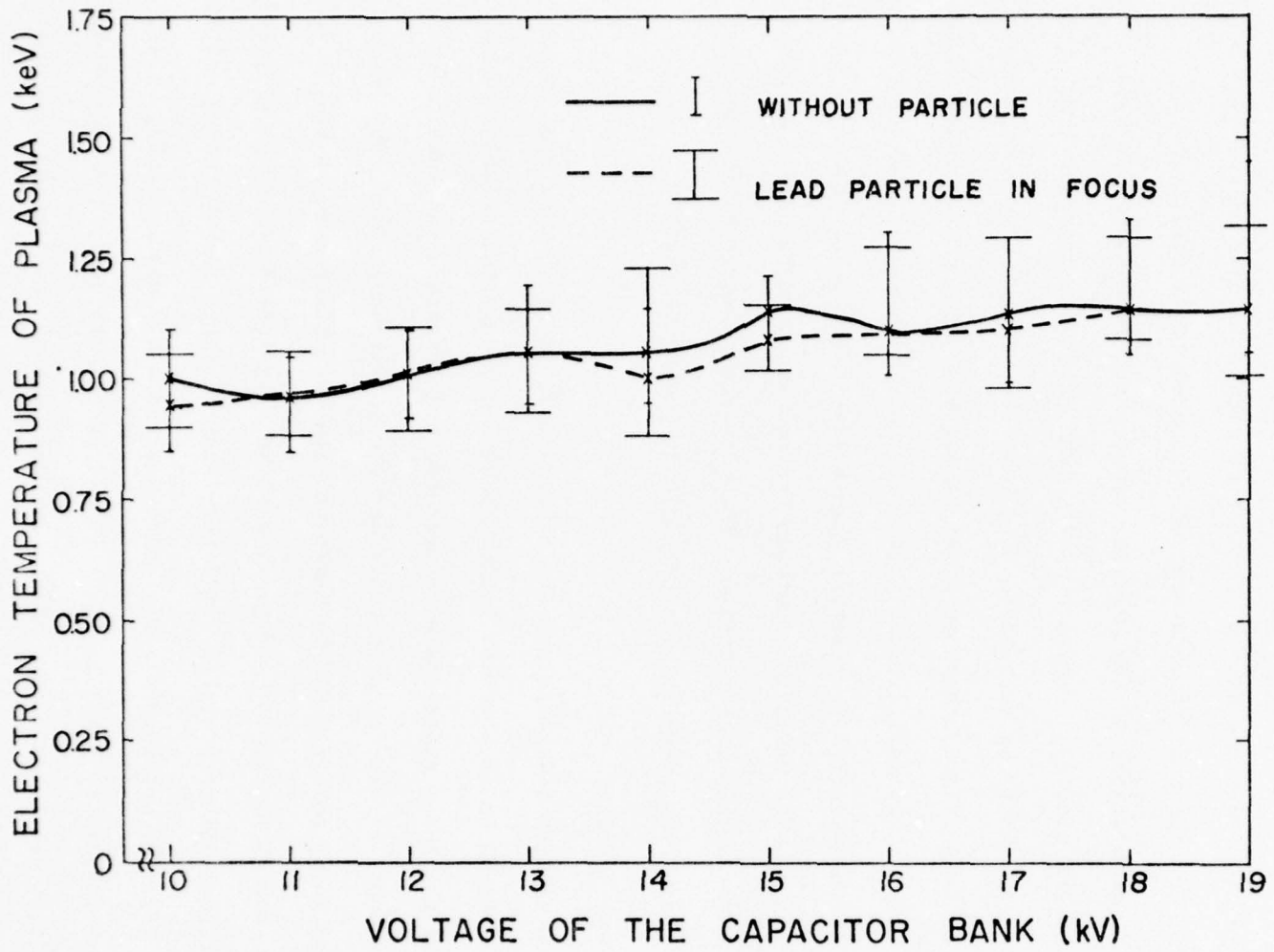

Fig. 5.3. Electron temperatures of the dense plasma focus (solid curve) and of a lead particle in the plasma focus (dotted curve) plotted vs. the voltage of the capacitor bank.

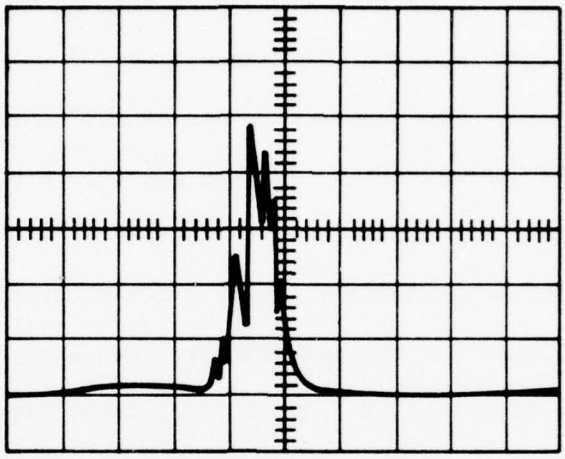

Fig. 5.4a. A typical time-resolved X-ray pulse as detected by a silicon semiconductor. Vertical scale: 1 V/division; time scale: 0.5 μsec/division.

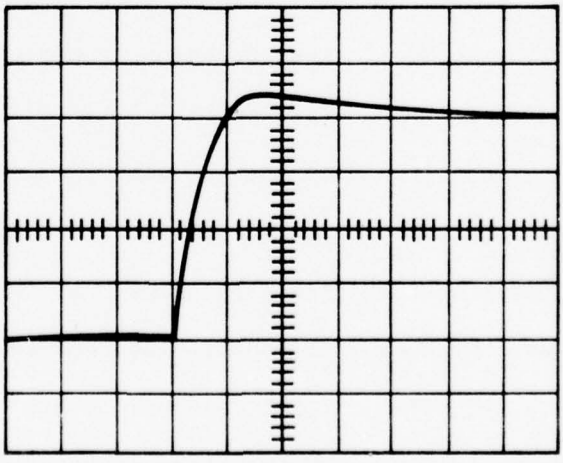

Fig. 5.4b. A time-integrated X-ray pulse giving the relative magnitude of total X-ray output. Vertical scale: 100 MV/division; time scale: 10 μsec/division.

the voltage of the capacitor bank in Fig. 5.5. These data were taken with a silicon detector with a 2-mil beryllium window. The graph shows an increase of the total X-ray output with the voltage of the capacitor bank. The relative output magnitude increases from 252 units at 10 kV up to 477 units at 19 kV. The increase factor is 1.89. Previous experimental results [12], [15], [23] show that the percentage of bank energy converted into X-ray energy is between 0.01 percent and 0.05 percent, depending on the machine and the operating voltage. If the focus machine in this work converts 0.02 percent of the bank energy, then the total X-ray emissions at 10 kV and 19 kV are 0.435 J and 1.57 J, respectively, and the increase factor will be 3.61 which is about twice the measured value of 1.89. The discrepancy is due to two factors: the anisotropic distribution of the X-ray radiation and the variation of the X-ray spectrum with the operating voltage. The distribution of the X-ray emission from a focus device is anisotropic [11] and the pattern varies with the operating voltage. The radiation distribution is a strong function of the acceleration of charged particles which is, in turn, affected by the electric field in the focus region. The X-ray spectrum also changes with the operating voltage. At higher voltages, more hard X-rays are produced because more charged particles are accelerated to higher energies. At lower voltages, more X-rays are produced by thermal Bremsstrahlung and result in the soft region. The detector efficiency of the solid state detectors is nonlinear with photon energy. The charge-generation efficiency of the silicon detectors decreases as the photon energy increases. This factor accounts for the smaller increase factor of 1.89 as measured because the detectors are more efficient in measuring the soft X-rays.

In Fig. 5.6, the mean values of the different X-ray outputs from the

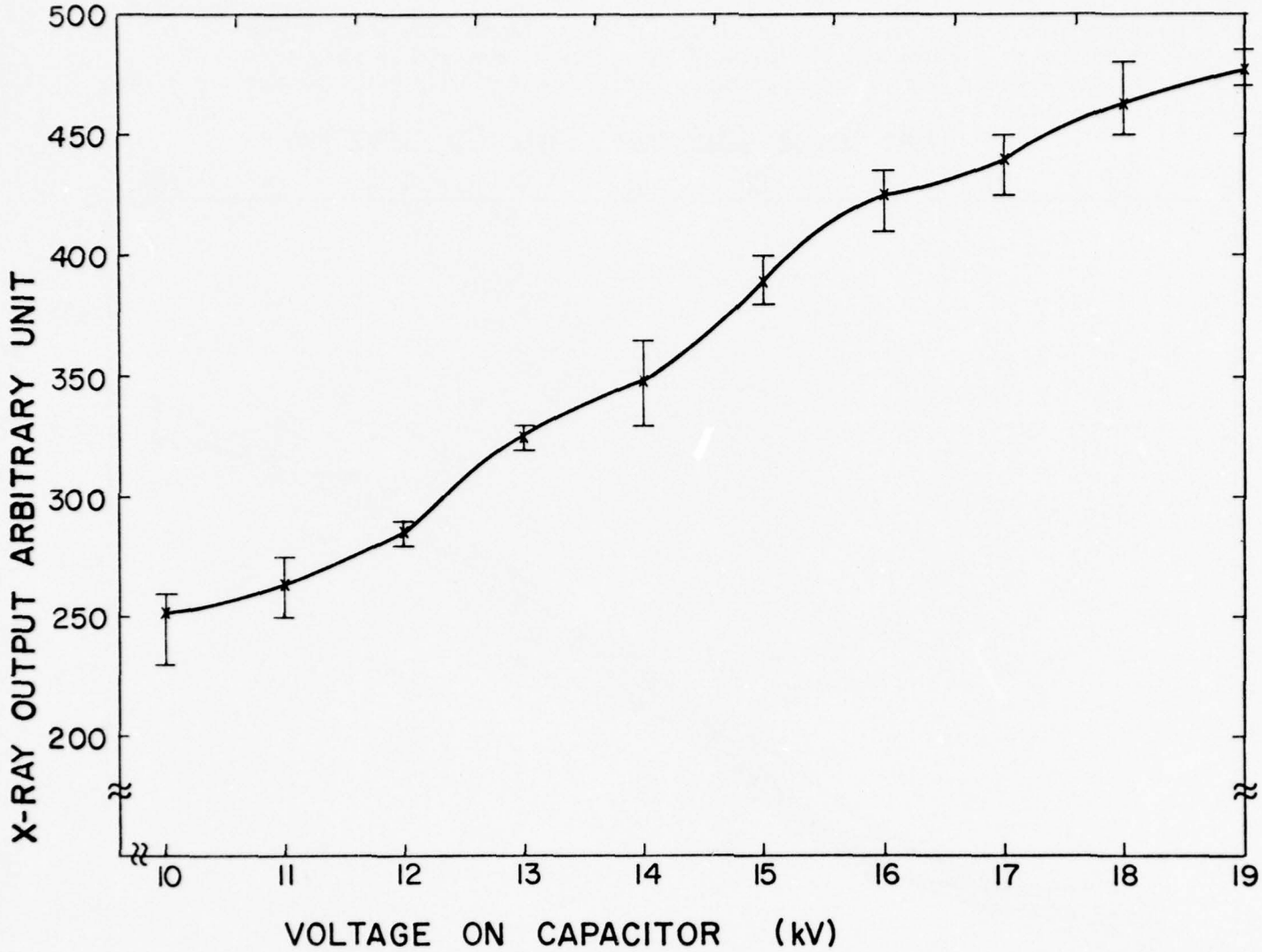

Fig. 5.5. The relative X-ray output from a dense plasma focus plotted vs. the voltage of the capacitor bank. Data were taken with a silicon detector with a 2-mil beryllium window.

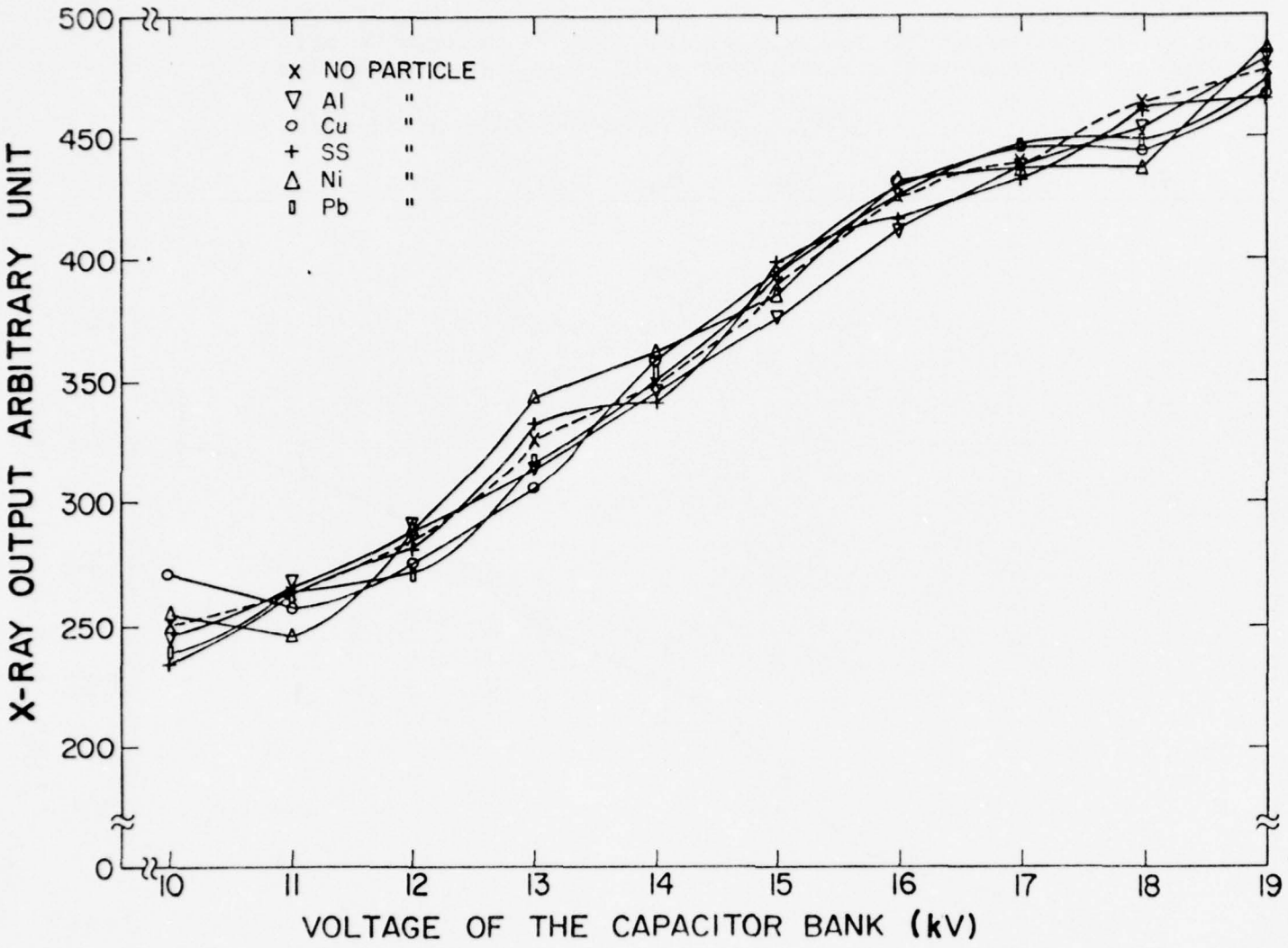

Fig. 5.6. The relative X-ray outputs from the interaction of the dense plasma focus with particles of different materials plotted vs. the voltage of the capacitor bank. Data were taken with a silicon detector with a 2-mil beryllium window.

interaction of the dense plasma focus with particles of various materials are compared. Besides stainless steel particles, target materials of 99 percent pure aluminum, nickel, copper and lead were used. All particles had a size of 1 mm diameter. The curves show that, within the experimental uncertainties, there is no change in the relative X-ray outputs due to plasma-particle interaction as compared to those of a dense plasma focus. This result does not follow the prediction of X-ray enhancement due to plasma-particle interaction, as reported previously in Chapter 3. A possible explanation is that the energy of the capacitor bank employed in this experiment was low, only 7.85 kJ at 19 kV. This small amount of energy might not be able to generate enough high energy electrons to bombard the particle. This situation is a "starvation" phenomenon in which no extra high energy electrons are present to bombard the additional target area. If a higher energy capacitor bank, e.g. 100 kJ, and a shorter discharge time, i.e., lower L and C values, were used in this experiment, more energetic electrons would be produced as more energy were available to be converted into the electrons' kinetic energy, and enhancement of X-ray emissions due to focus-particle interaction should be observed. Fig. 5.7 is an optical picture of a lead particle interacting with the dense plasma focus. The vertical glowing line was due to the light reflected from the particle-supporting glass stalk.

The relative X-ray outputs from the plasma-particle interactions were measured with different metallic foils as filters. The thicknesses of the filters used were 0.002 inch $\left(9.6\ mg/cm^2\right)$ for beryllium, 0.0003 inch $\left(2.025\ cm/cm^2\right)$ for aluminum, 0.0001 inch $\left(2.3\ mg/cm^2\right)$ for nickel, and 0.00004 inch $\left(2\ mg/cm^2\right)$ for gold. At different capacitor bank voltages, the relative X-ray emissions transmitted through these filters are compared in Fig. 5.8 a-e. Because the transmission coefficient of materials for

Fig. 5.7. The optical picture of a lead particle interacting with the dense plasma focus. The vertical glowing line was due to the light reflected from the particle-supporting glass stalk. Operating conditions : voltage, 19 kV; pressure, 1 torr.

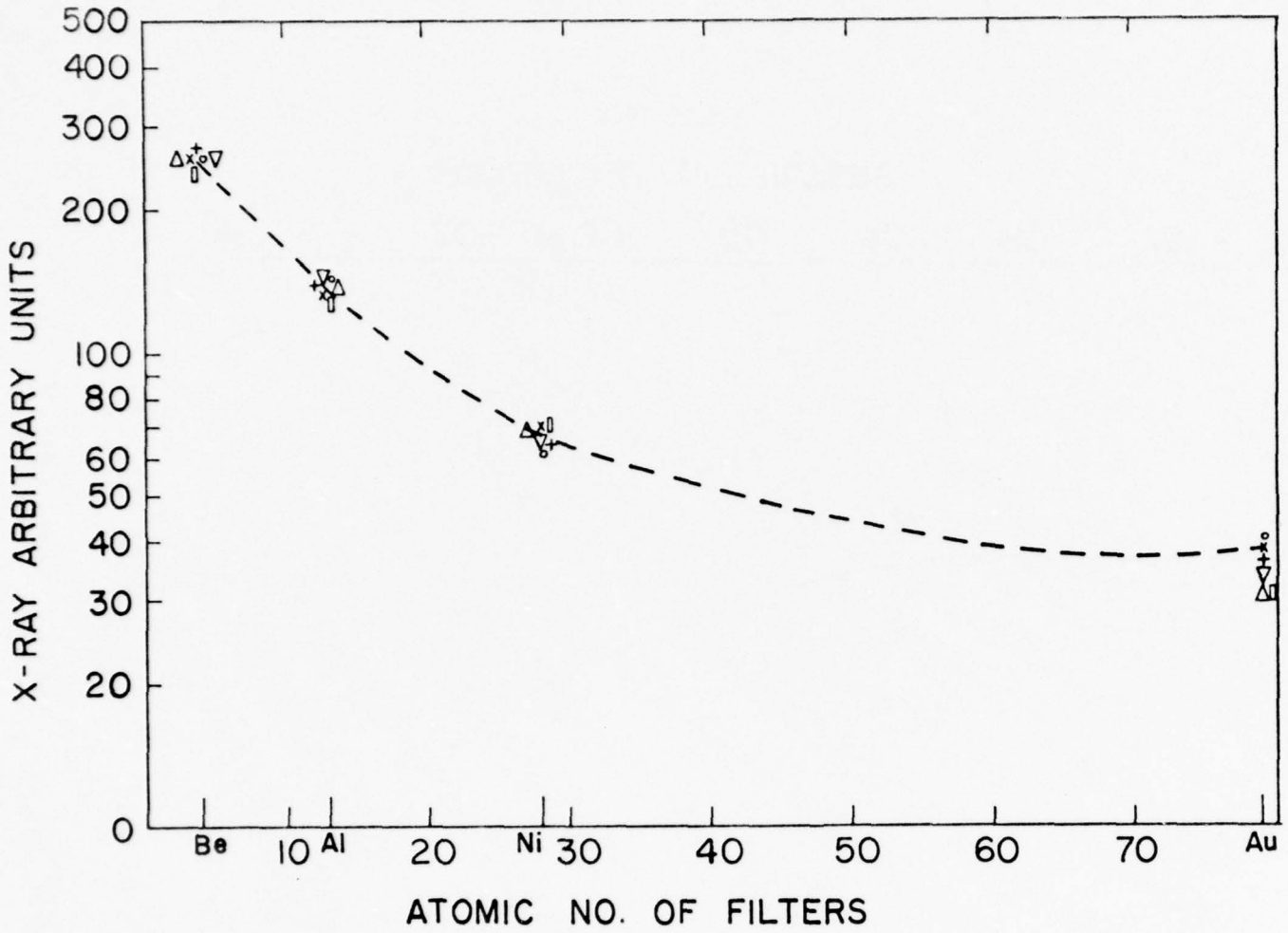

Fig. 5.8a

Fig. 5.8 a-e. X-ray from the interactions of plasma focus with different particles plotted versus the atomic number of the metallic filters used. Capacitor bank voltage was 11 kV in (a), 13 kV in (b), 15 kV in (c), 17 kV in (d), and 19 kV in (e).

Key: X no particle
∇ aluminum "
Δ nickel "
o copper "
+ stainless steel "
▯ lead "

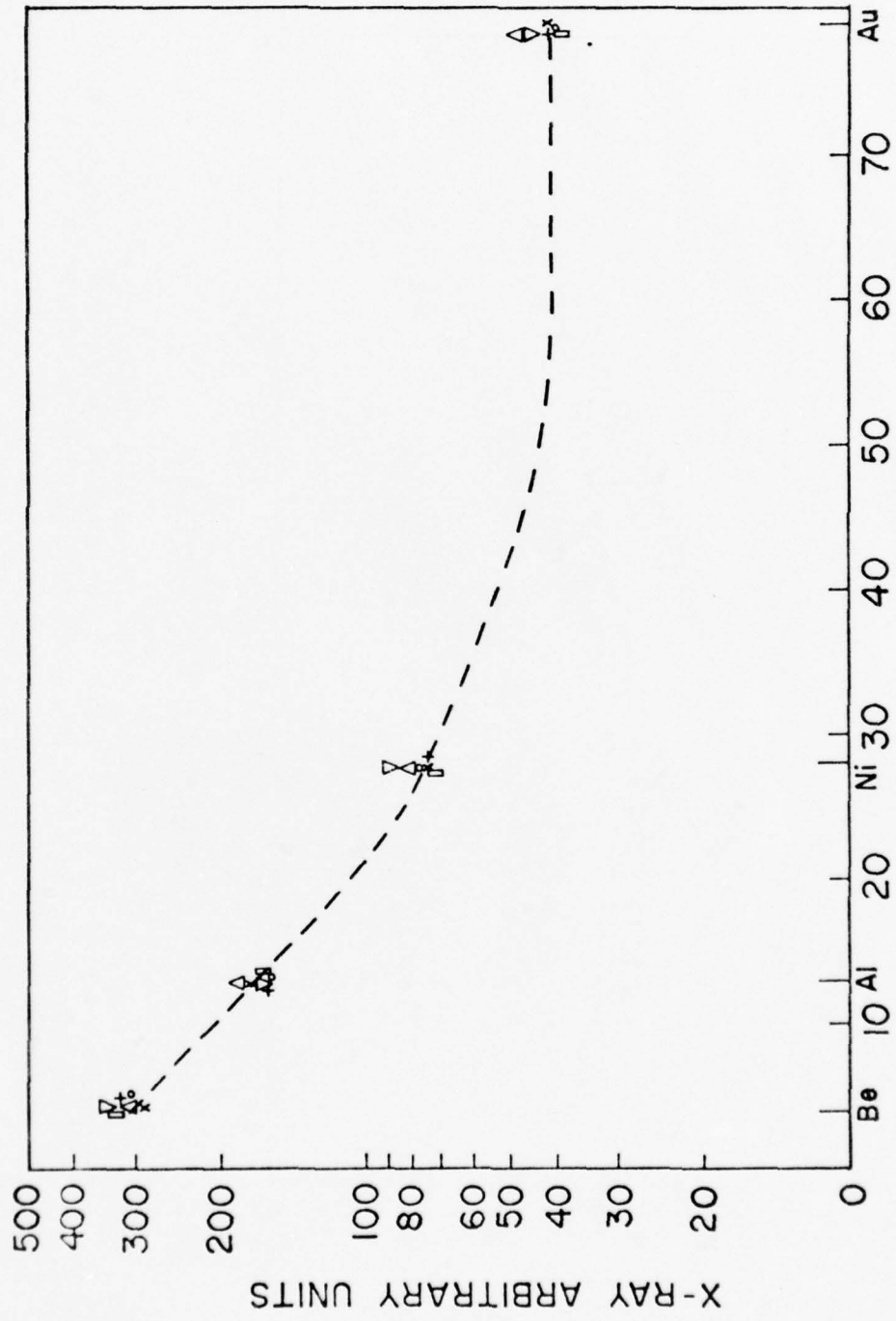
X-RAY ARBITRARY UNITS
500
400
300
200
100
80
60
50
40
30
20
0
Be
10
Al
20
Ni
30
40
50
60
70
Au
ATOMIC NO. OF FILTERS

Fig. 5.8b

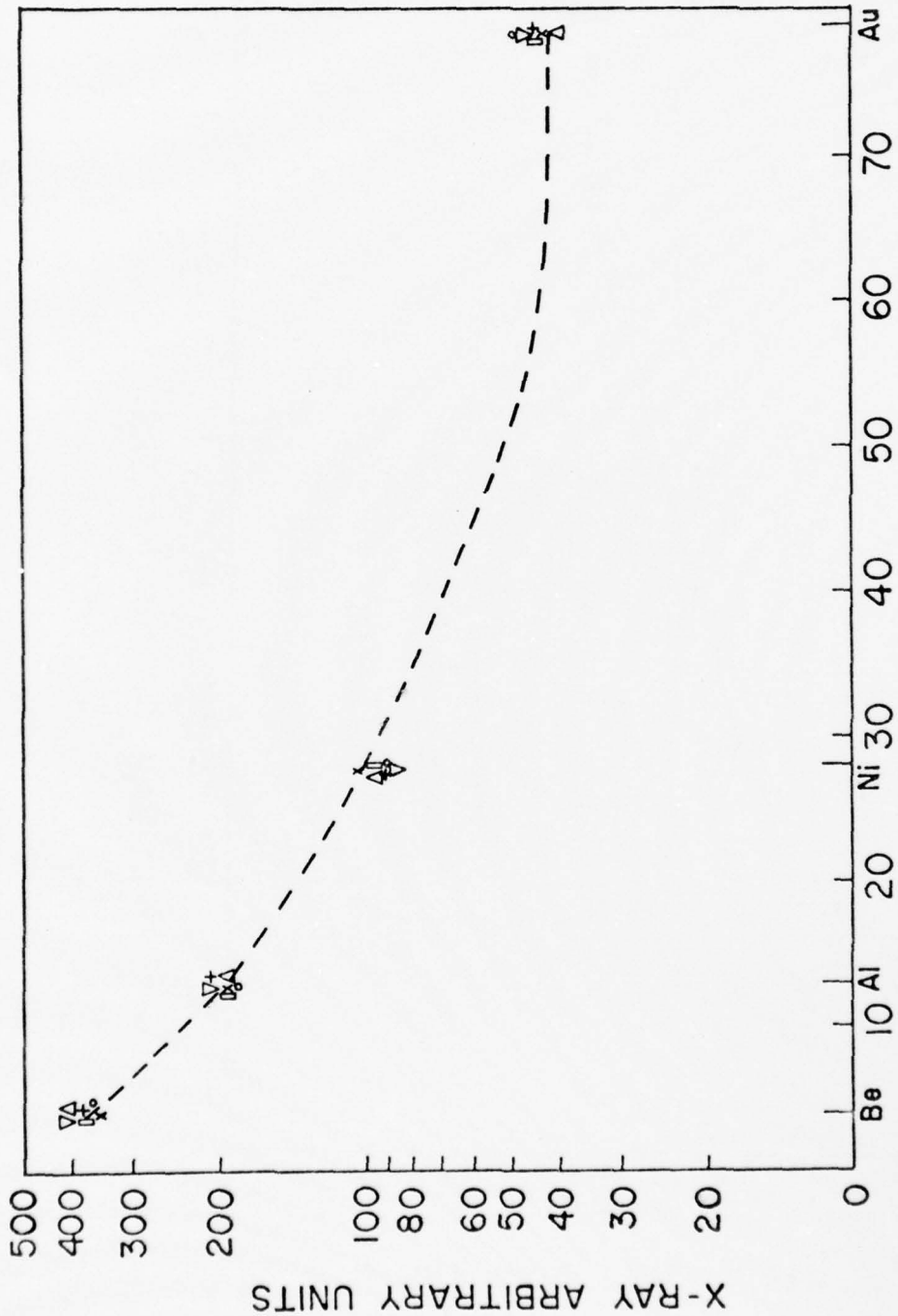
X-RAY ARBITRARY UNITS
500
400
300
200
100
80
60
50
40
30
20
0
Be
10
Al
20
Ni
30
40
50
60
70
Au
ATOMIC NO. OF FILTERS

Fig. 5.8c

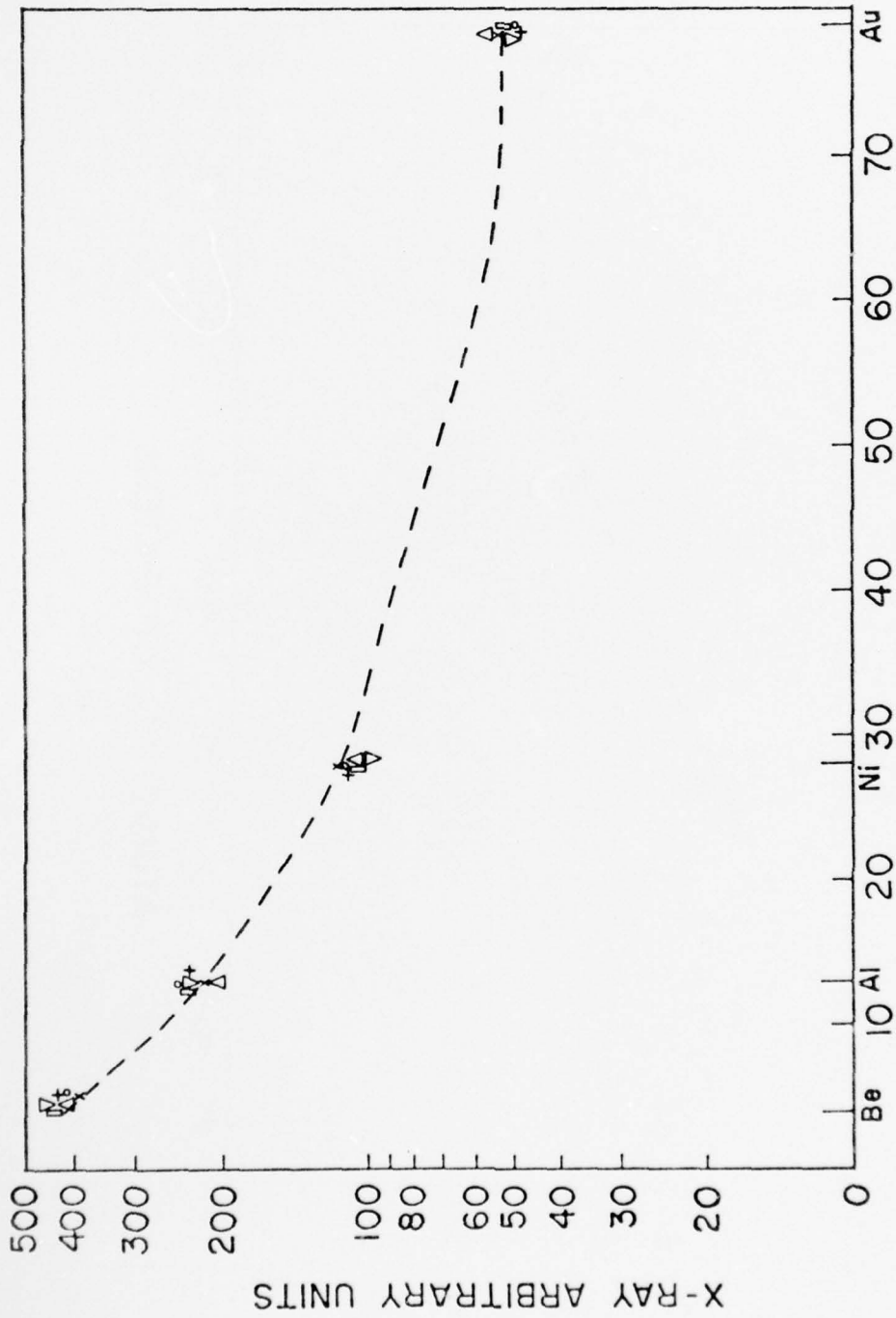
X-RAY ARBITRARY UNITS
500
400
300
200
100
80
60
50
40
30
20
0
Be
10
Al
20
Ni
30
40
50
60
70
Au
ATOMIC NO. OF FILTERS

Fig. 5.8d

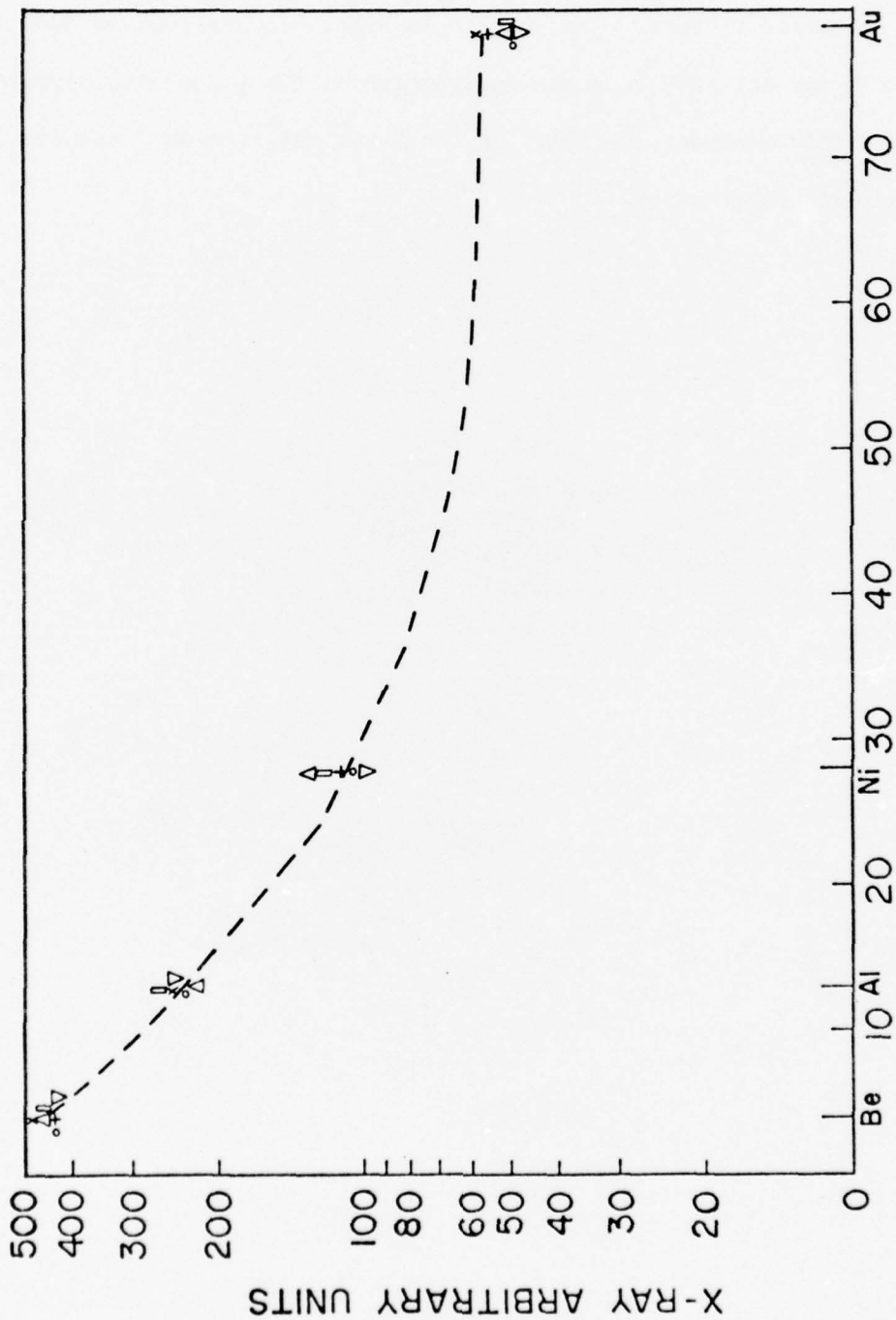
X-RAY ARBITRARY UNITS
500
400
300
200
100
80
60
50
40
30
20
0
Be
Al
Ni
Au
10
20
30
40
50
60
70
ATOMIC NO. OF FILTERS

Fig. 5.8e

X-rays is a strong function of the wavelength of the incident photon, any change in the composition of the X-ray spectrum will be reflected by the relative change in the magnitudes of the transmitted X-rays through different metallic filters. The results in Figs. 5.8 a-e show no such change for X-ray emission from the interaction of the focus with different particles. This excludes any shift in the X-ray spectrum as a result of plasma-particle interaction.

6. CONCLUSION AND RECOMMENDATIONS

6.1 Conclusion

Recently the interest in dense plasma focus has greatly increased because of the possibility of developing the device into an intense, pulsed radiation source of X-rays and neutrons for test purposes. Various experimenters [6], [15], [28], have tried to scale up their radiation intensities by using large capacitor banks. Yet Mather's [2] experimental results show that besides the engineering problems associated with the machine as the bank voltage or capacitance goes up, the intensity cannot be scaled up indefinitely by increasing the bank energy. This work proposed a new, alternative way to enhance the X-ray radiation by using a macroscopic particle to interact with a plasma focus.

A theoretical study was carried out to predict the relative amount of X-ray increase when a macroscopic particle was placed in the focus region. Two assumptions were made in this study: the particle essentially had the same physical dimensions throughout the lifetime of the focus because of enormous hydrodynamic pressure compressing any ablated neutral cloud onto the particle; and the electrons were thermalized to assume a Maxwellian distribution. Most of the X-ray radiation from a focus was due to the electron bombardment of the anode surface and was accounted for by the thick target Bremsstrahlung theory. According to this theory, the X-ray emission was proportional to the first power of the atomic number, Z, of the target material, but not to the square of Z as in the thermal Bremsstrahlung case. The percentage of X-ray enchancement expected was calculated and tabulated in Table 3.1 for various particle materials and sizes.

An experiment was conducted to test this new approach. A dense plasma focus device was designed and built. However, because of budgetary and time limitations the device was not optimized as predicted by theoretical studies of electrical parameters. The capacitor bank did not deliver the maximum available current because of the limitation of the system's ringing frequency. The large inductance associated with the capacitors was critical to the current rise time. In addition, transmission line and high voltage switch inductances proved to be limiting factors on current rise time and circuit ringing frequency. Yet the 400×10^3 A current at 19 kV was high enough to produce the plasma focus in a pressure range between 0.5 torr to 2 torr.

The electron temperature of the focus is estimated to be 1.15 ± 0.3 keV by measuring the X-ray emissions through beryllium foils of different thickness. This value is in good agreement with that of other focus experiments.

The results of this work show that the total X-ray emission from this dense plasma focus are not enhanced by placing a macroscopic particle in the focus region. Based on the thick target Bremsstrahlung theory, theoretical study predicts the possibility of X-ray enchancement by such an arrangement. However experimental results show no change in the total X-ray emissions from such plasma-particle interaction. An explanation is the low energy bank employed in this experiment, only 7.85 kJ at 19 kV. Not enough high energy electrons were generated by this small amount of energy. This "starvation" phenomenon provided no extra high energy electrons to bombard the additional target area. If a higher energy capacitor bank and a higher ringing frequency system were used, more energetic electrons would be produced, and enhancement of X-ray emissions due to

focus-particle interaction should be observed.

Also there appears no apparent change in the X-ray spectra of various plasma-particle interactions, as measured by using different metallic foils. This observation is different from Johnson's results [23]. In his experiment, atomic particles of tungsten were introduced to interact with a plasma focus. His data showed that there was no increase in the total X-ray output but a shift of the X-ray energy from the hard X-ray region to the soft X-ray region.

6.2 Recommendations

More effort should be expended to investigate the plasma focus-particle interaction. An optimal plasma focus machine should employ capacitors of low inductance, e.g., Aerovox capacitors of 10 nH, and low capacitance for faster current rise time, and of high voltage for high bank energy.

Engineering techniques should be developed to drop particles freely into the focus region. An earlier attempt in using a photoelectronic detector had been unsuccessful because of the interference of the electromagnetic pulse associated with the gaseous discharge. The present technique of supporting the particle by a glass stalk is not the best solution because the presence of the stalk may affect the current sheath at the collapse stage. Yet the small variation in the electron temperature indicates that the plasma focus was not significantly affected by a particle in the focus region. A possible technique is to use a laser beam to detect the particle. Yet the requirements on the accuracy of particle-positioning and system synchronization demand no trivial solutions.

Better diagnostic methods are required to provide more informative experimental results. The Ross filter technique [15] can provide better resolutions in the X-ray spectrum measurement. The absolute X-ray

intensity can be measured by using K-edge filters with solid state detectors. Knowing the characteristic functions of the filters and detectors, and the response from the experimental data, the excitation (the X-ray detected) can be unfolded by the computer program, PHOTOCAL, developed at Livermore Laboratory [41]. Other time-resolved instruments like an ultrafast X-ray streak camera [41] with subnanosecond resolution and an optical streak camera are essential to provide the time history of the focus-particle interaction process.

APPENDIX A

INDUCTANCE OF THE PLASMA GUN

To estimate the inductance of the coaxial plasma gun, the structure of the gun can be approximated as two coaxial cylinders, Fig. A-1. A current I flows into the paper. Applying the Maxwell's equation to find the magnetic intensity at position r,

$$\oint \vec{H}(r) \cdot d\vec{\ell} = I = 2\pi r H(r). \tag{A.1}$$

$$L_{gun} \equiv \frac{\phi}{I} .$$

$$\text{and } \phi = \int \vec{B} \cdot d\vec{A} = \oint \mu_0 \vec{H}(r) \cdot d\vec{A} .$$

$$\text{As } d\vec{A} = \ell dr\hat{\theta}$$

$$\therefore \phi = \int_a^b \mu_0 \vec{H}(r) \cdot \ell dr\hat{\theta} = \frac{\mu_0 I \ell}{2\pi} \int_a^b \frac{dr}{r} = \frac{\mu_0 I \ell}{2\pi} \ln\left(\frac{b}{a}\right) . \tag{A.2}$$

Therefore, the inductance per unit length of the gun is

$$\frac{L_{gun}}{\ell} = \frac{\mu_0}{2\pi} \ln\left(\frac{b}{a}\right) \text{ H/m} . \tag{A.3}$$

The dimensions of the plasma gun are:

$$b = 1.9" = 0.04826 \text{ m}$$

$$a = 0.89" = 0.02261 \text{ m}$$

$$\ell = 8.615" = 0.21882 \text{ m}$$

$$= 4\pi \times 10^{-7} \text{ H/m} .$$

The total inductance of the gun, L_{gun}, is

$$L_{gun} = \frac{\mu_0 \ell}{2\pi} \ln\left(\frac{b}{a}\right) \text{H} = 33.19 \times 10^{-9} \text{ H} .$$

Also, the time derivative of the gun inductance is

$\dot{L}_{gun} = \frac{L_{gun}}{t_p} = \frac{L_{gun}/\ell}{t_p/\ell} = \frac{L_{gun}}{\ell} \times v_s$, where v_s = velocity of the current in m/sec.

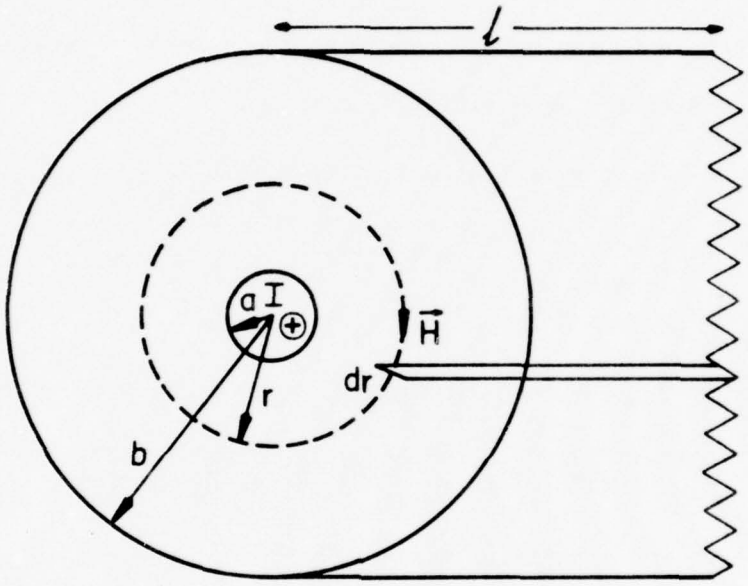

a = radius of inner cyline

a = radius of inner cylinder

b = radius of outer cylinder

ℓ = length of the cylinders

L_{gun} = inductance of the gun

ϕ = magnetic flux

Fig. A.1. Inductance of coaxial cylinders.

Thus,

$$\dot{L}_{gun} = \left(\frac{E^2}{\mu_0 \rho_0}\right)^{1/4} \frac{\mu_0}{2\pi} \ln\left(\frac{b}{a}\right) \text{ H/sec} . \qquad (A.4)$$

APPENDIX B

ELECTRIC FIELD BETWEEN COAXIAL CYLINDERS

With Gauss' law,

$$\int \vec{D}(r) \cdot d\vec{A} = Q \ .$$

$$D(r) = \sigma(r) = \frac{Q}{2\pi r \ell}$$

$$\text{or} \quad E(r) = \frac{Q}{2\pi\varepsilon_0 r \ell} \ . \tag{B.1}$$

Since

$$V = -\int_a^b E(r)dr = \int_b^a \frac{Q}{2\pi\varepsilon_0 r \ell}\, dr = \frac{Q}{2\pi\varepsilon_0 \ell} \ln\left(\frac{a}{b}\right) \ . \tag{B.2}$$

Combining Eq. (B.1) and (B.2),

$$E(r) \approx \frac{V}{r \ln\left(\frac{a}{b}\right)} \ . \tag{B.3}$$

To calculate the average electric field between the two cylinders, take

$$r \approx \frac{a + b}{2} \ .$$

Therefore,

$$E_{avg} = \frac{V}{\left(\frac{a + b}{2}\right) \ln\left(\frac{a}{b}\right)} \ . \tag{B.4}$$

If V = 15 kv

a = 0.89" = 0.0226 m.

b = 1.9" = 0.0483 m.

$E_{avg} = 5.582 \times 10^5$ V/m.

Fig. B.1 shows the electric field between the coaxial cylinders.

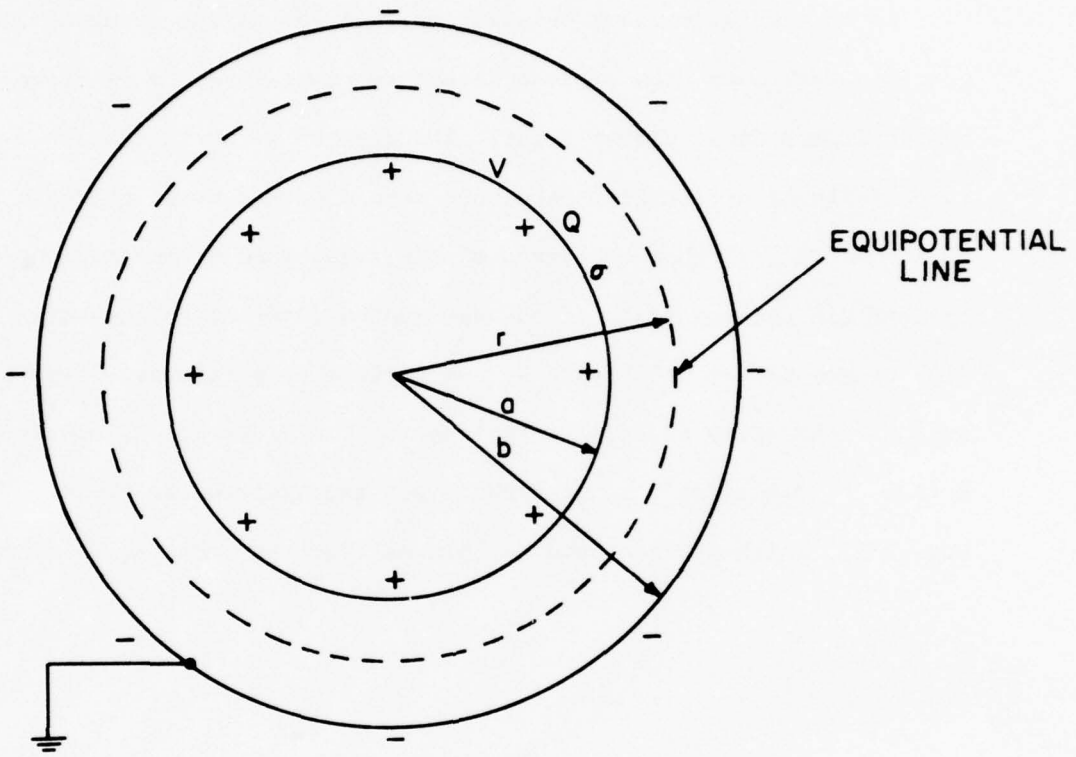

a = radius of inner cylinder

b = radius of outer cylinder

ℓ = length of the cylinders

V = voltage between the cylinders

Q = total charge on the inner cylinder

σ = surface charge on the inner cylinder

Fig. B.1. Electric field between the coaxial cylinders.

APPENDIX C

X-RAY TRANSMISSION THROUGH METALLIC FOILS

In this work, various metallic foils of beryllium, aluminum, nickel, and gold were used with silicon detectors to measure the relative X-ray output from a dense plasma focus. The data of X-ray transmission through these foils of different thicknesses were obtained from reference 40. Figs. C-1 to C-12 show the ratio of the integrated Bremsstrahlung emission transmitted through foils of the designated material to the total incident flux versus filter thickness, D, for various temperatures. From Figs. C-1 and C-2, the ratio of ordinate values for two different thicknesses, 24 mg/cm^2 and 9.6 mg/cm^2, is plotted versus temperature, as shown in Fig. C-13, which is then used for plasma electron temperature determination.

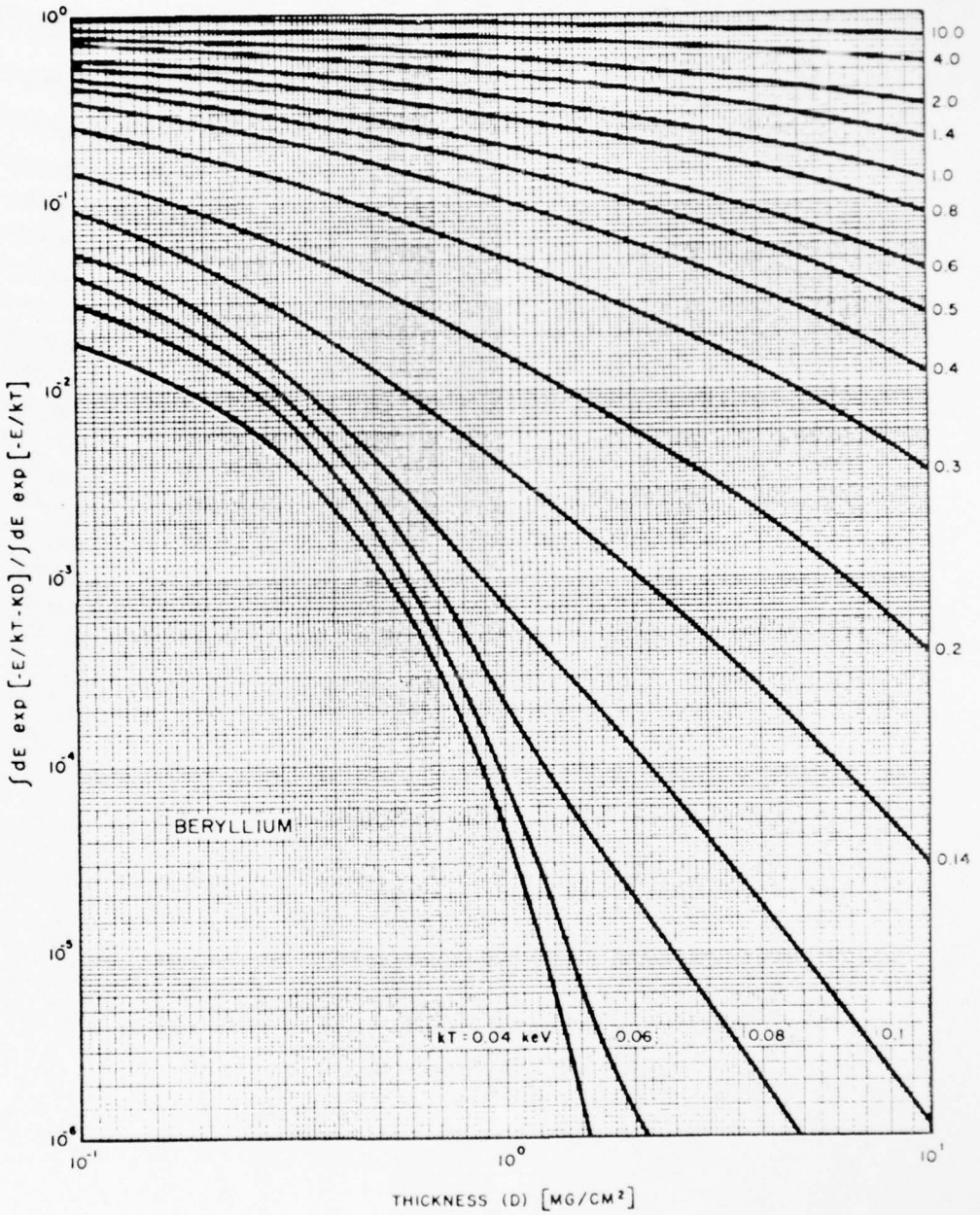

Fig. C-1. Ratio of the integrated Bremsstrahlung emission transmitted through foils of the designated material to the total incident flux vs. foil thickness, D, for various temperatures.

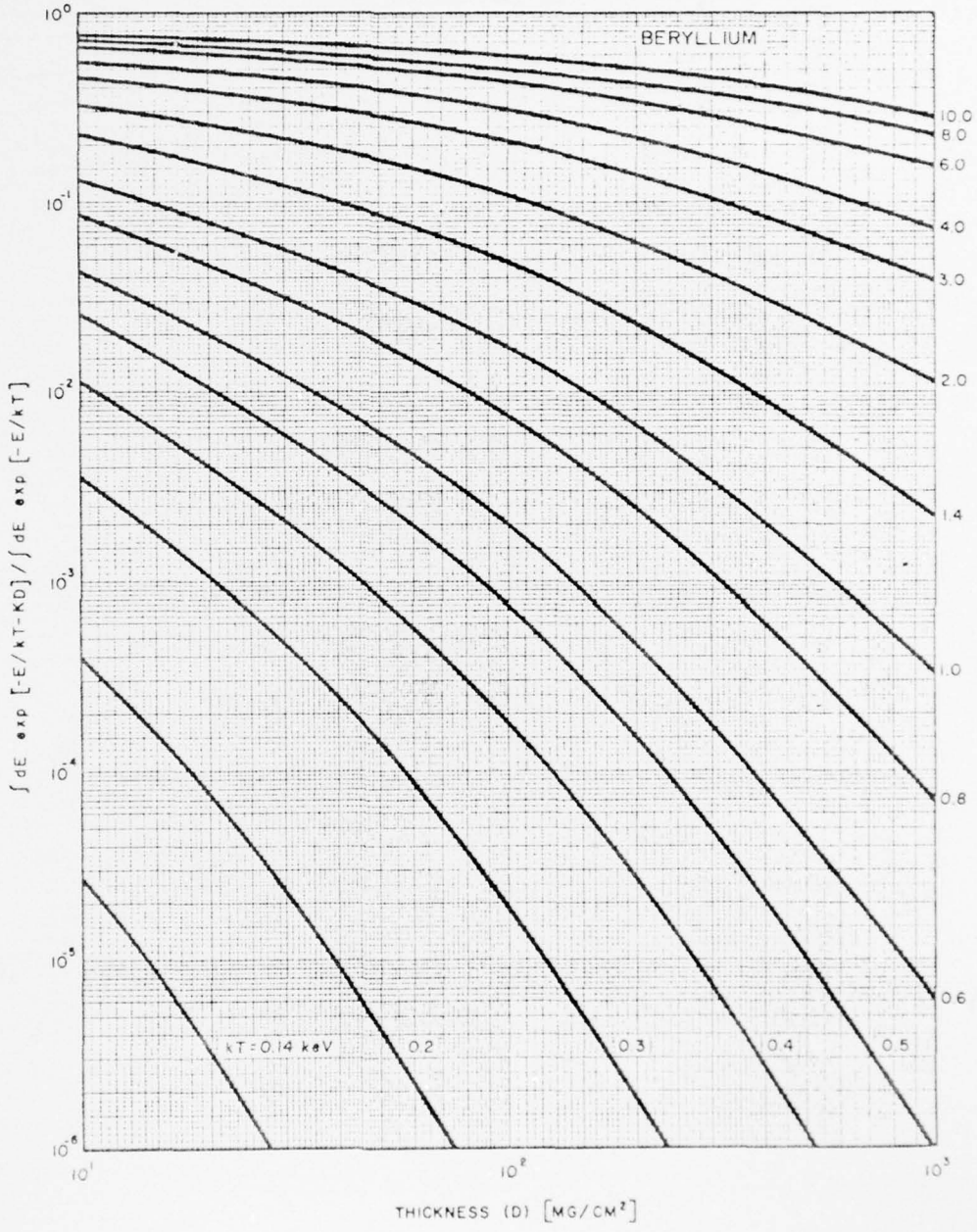

Fig. C-2. Ratio of the integrated Bremsstrahlung emission transmitted through foils of the designated material to the total incident flux vs. foil thickness, D, for various temperatures.

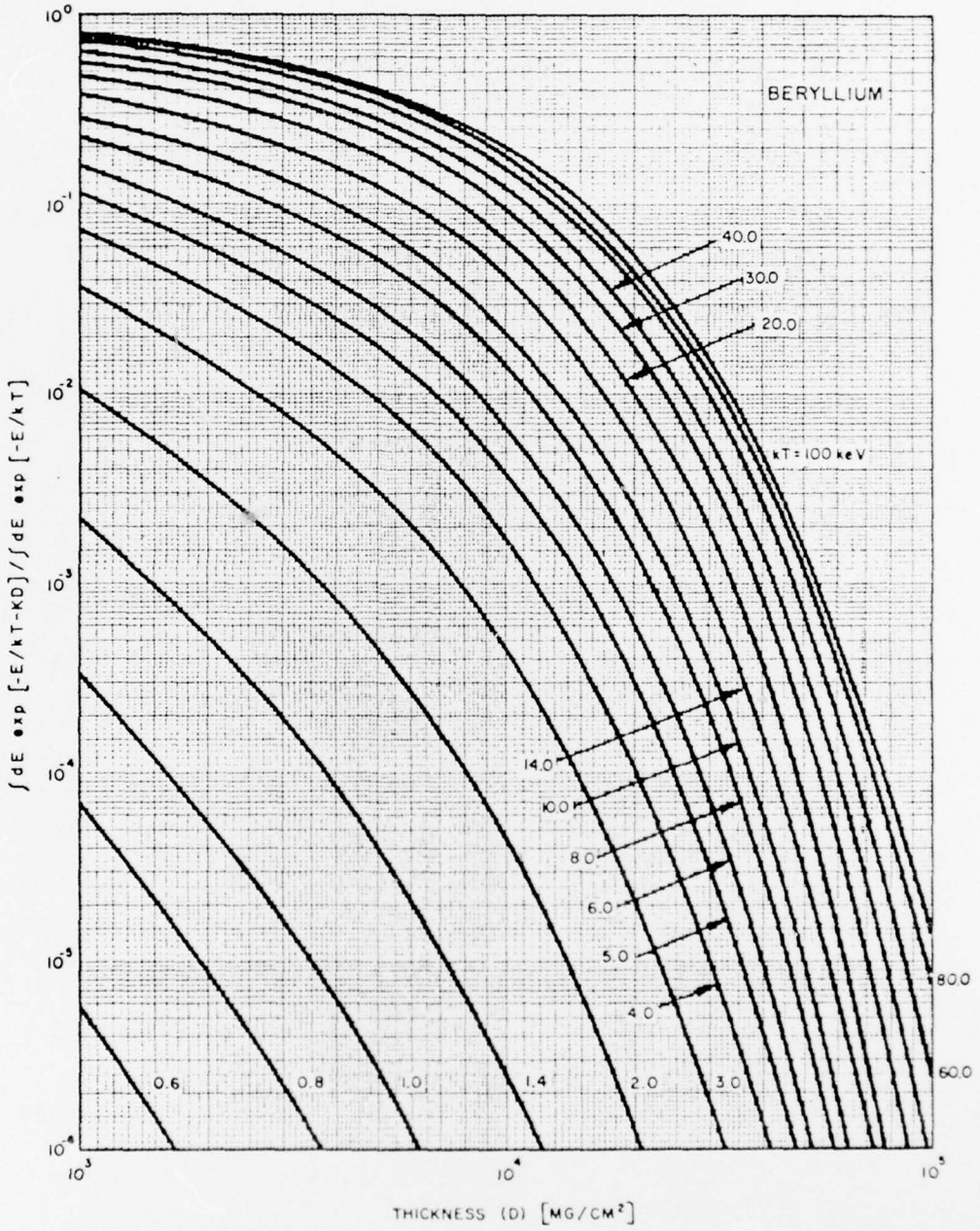

Fig. C-3. Ratio of the integrated Bremsstrahlung emission transmitted through foils of the designated material to the total incident flux vs. foil thickness, D, for various temperatures.

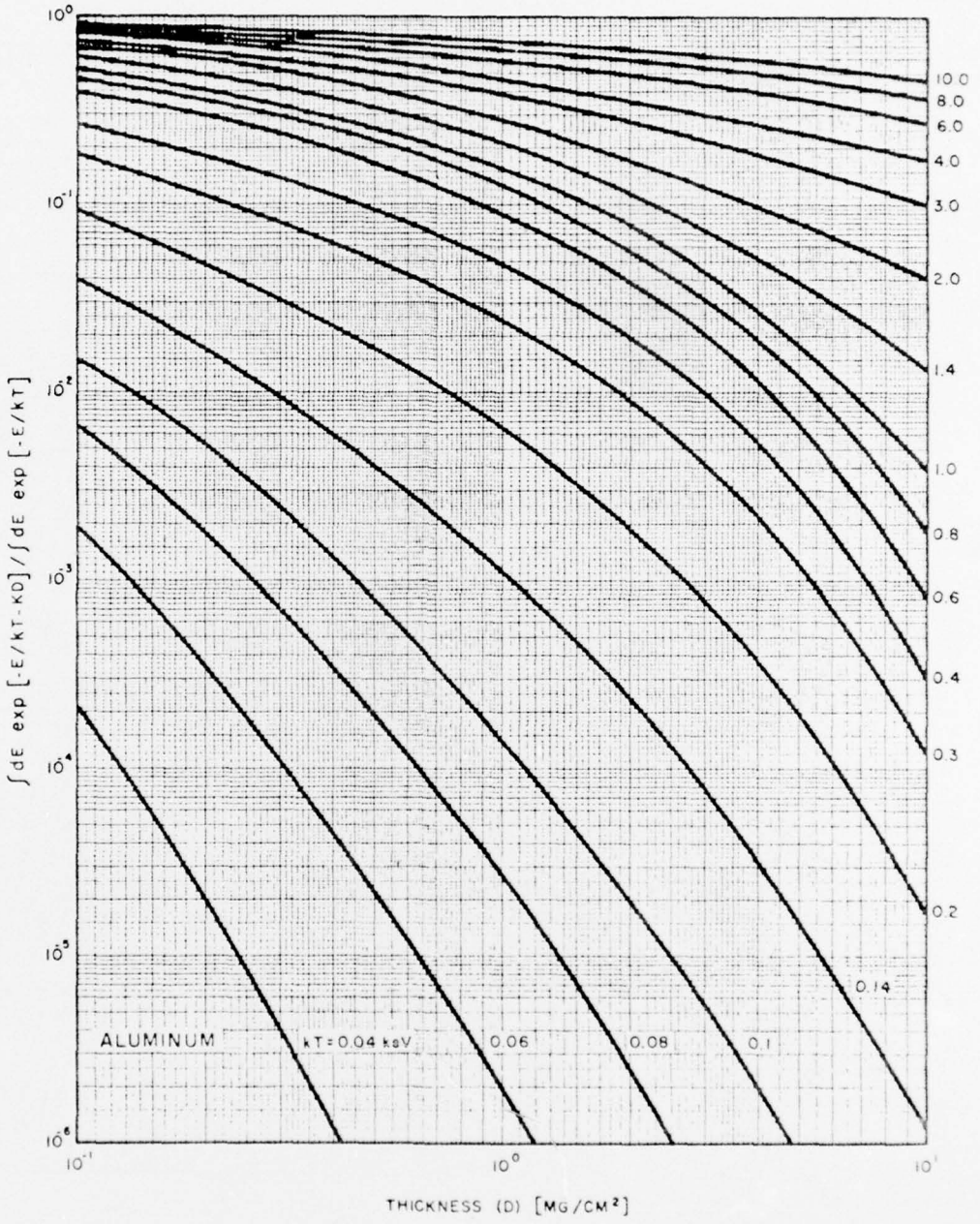

Fig. C-4. Ratio of the integrated Bremsstrahlung emission transmitted through foils of the designated material to the total incident flux vs. foil thickness, D, for various temperatures.

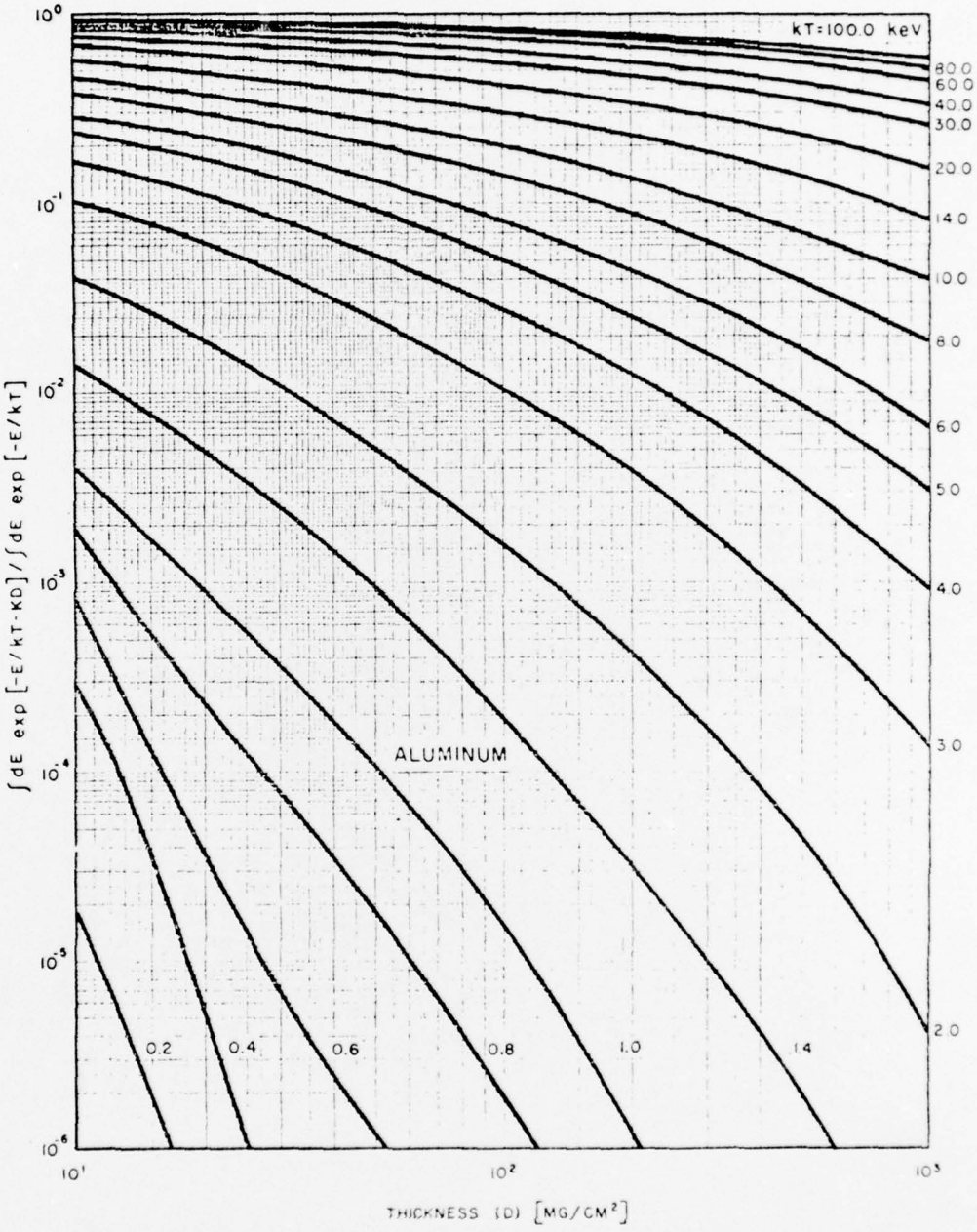

Fig. C-5. Ratio of the integrated Bremsstrahlung emission transmitted through foils of the designated material to the total incident flux vs. foil thickness, D, for various temperatures.

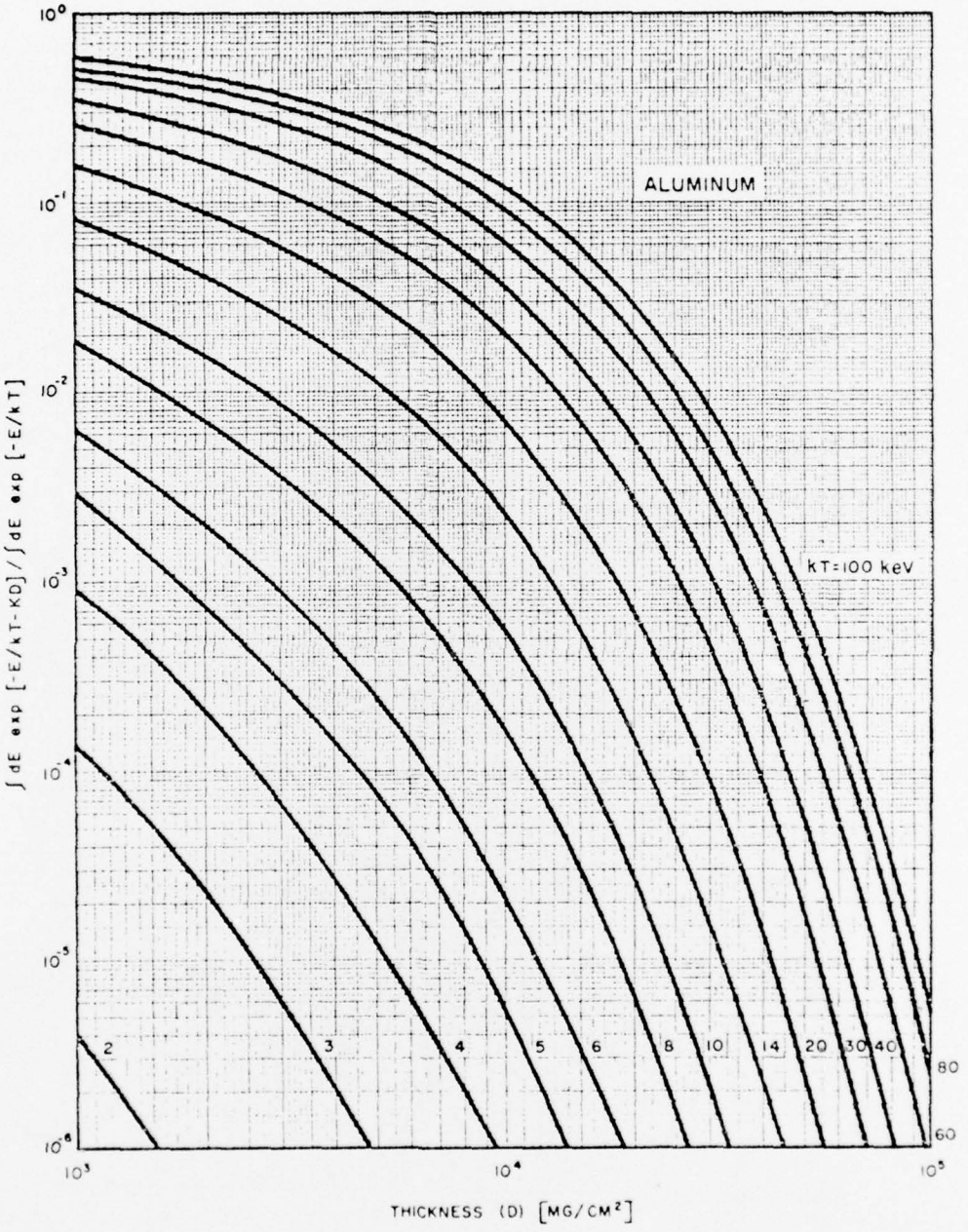

Fig. C-6. Ratio of the integrated Bremsstrahlung emission transmitted through foils of the designated material to the total incident flux vs. foil thickness, D, for various temperatures.

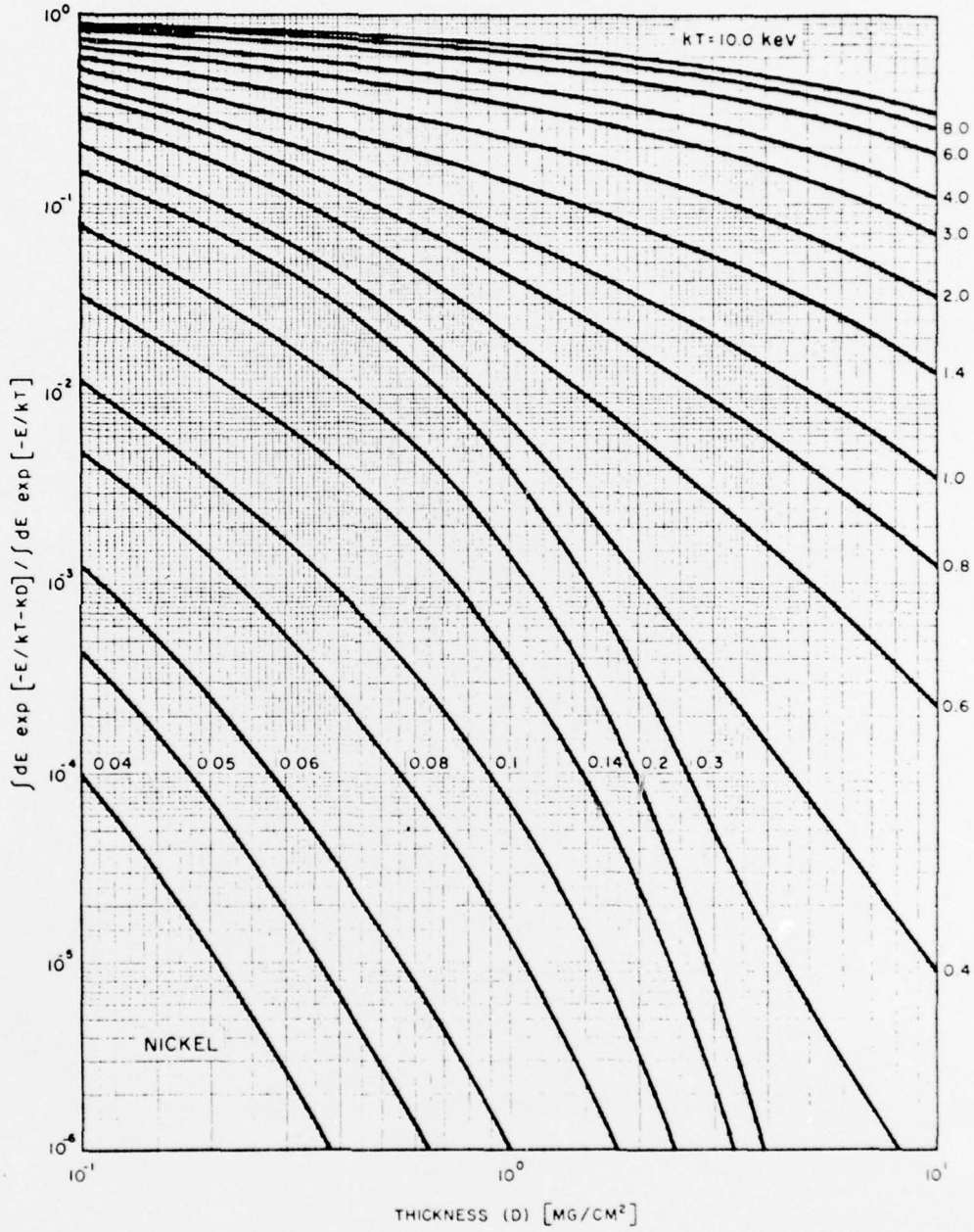

Fig. C-7. Ratio of the integrated Bremsstrahlung emission transmitted through foils of the designated material to the total incident flux vs. foil thickness, D, for various temperatures.

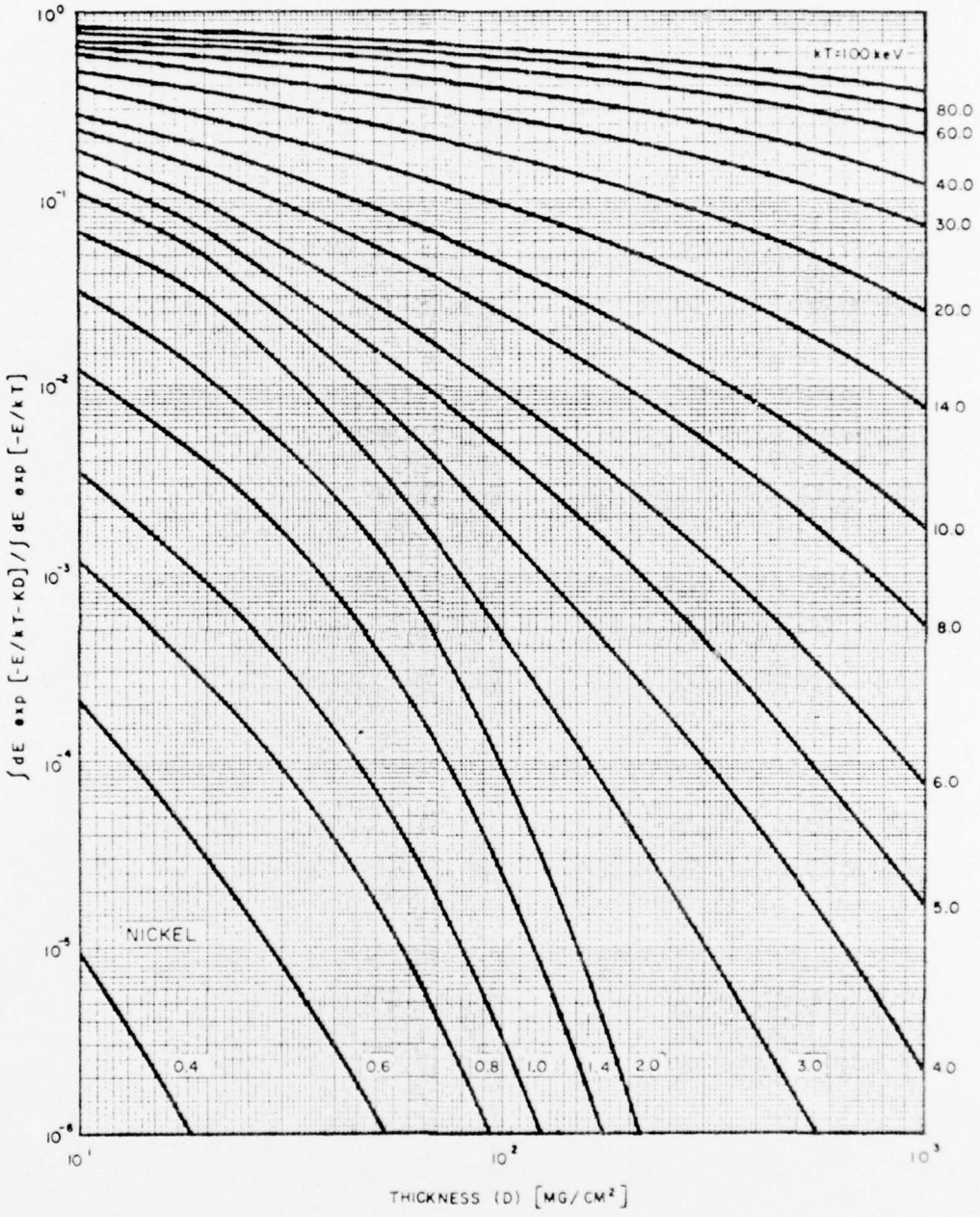

Fig. C-8. Ratio of the integrated Bremsstrahlung emission transmitted through foils of the designated material to the total incident flux vs. foil thickness, D, for various temperatures.

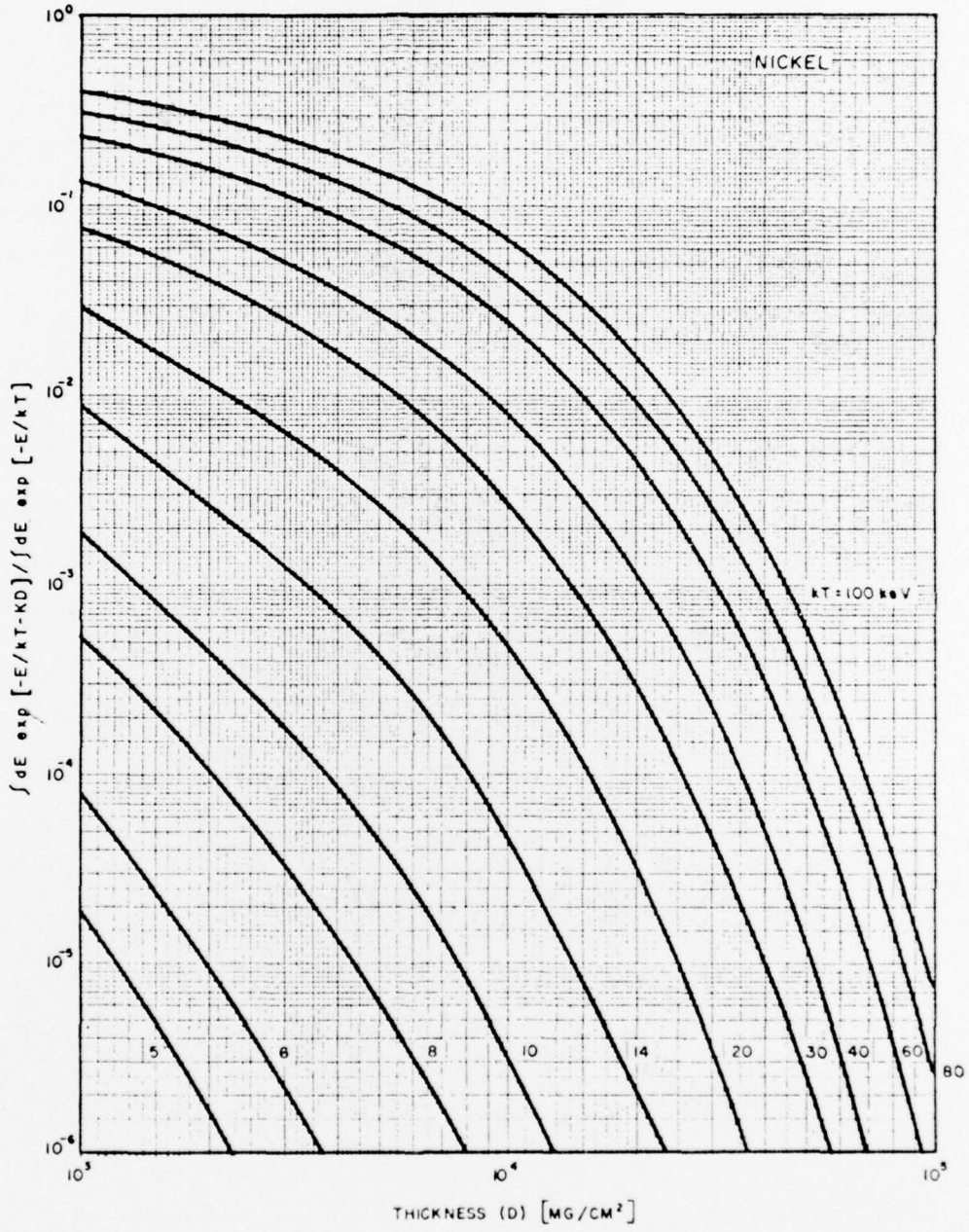

Fig. C-9. Ratio of the integrated Bremsstrahlung emission transmitted through foils of the designated material to the total incident flux vs. foil thickness, D, for various temperatures.

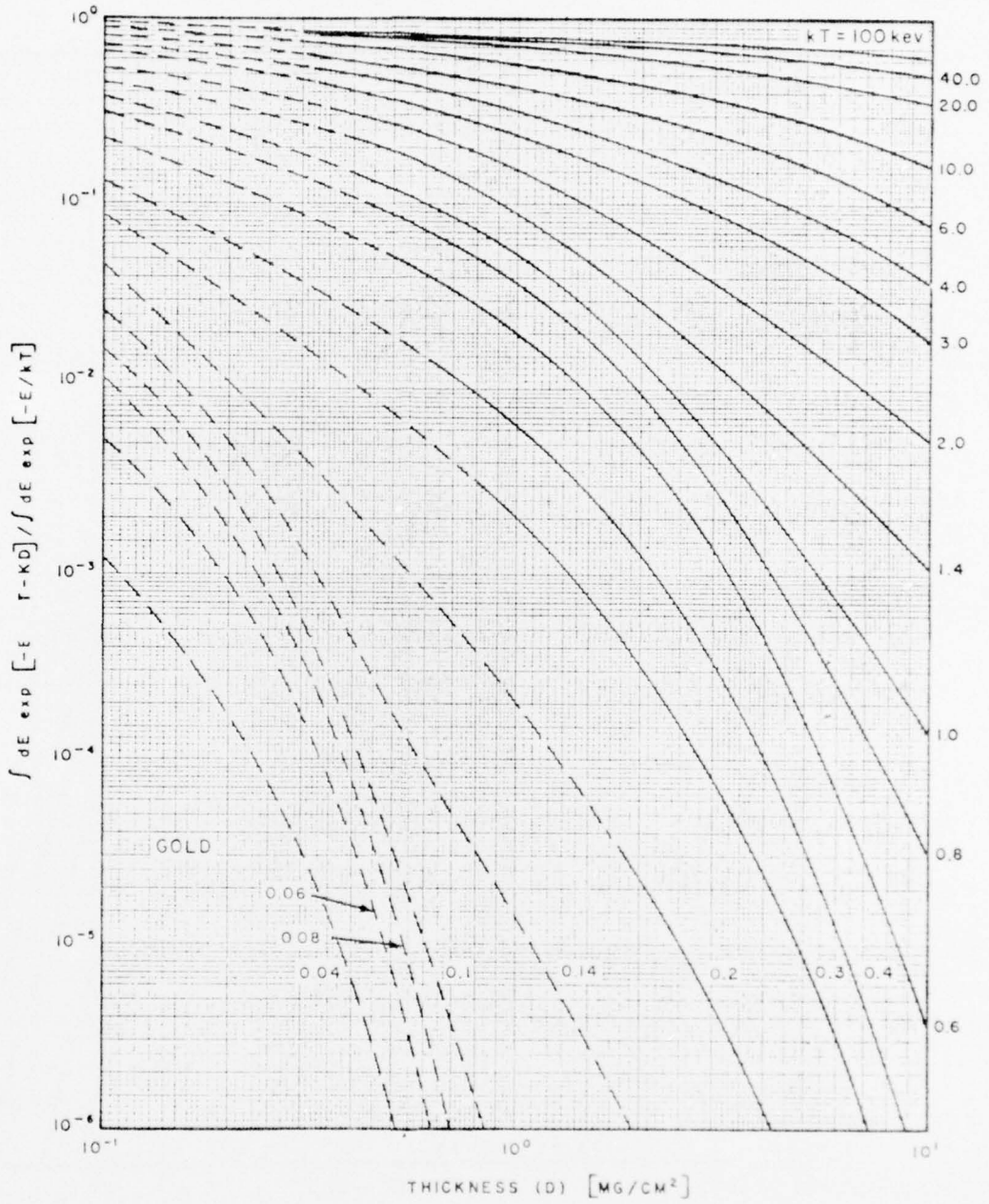

Fig. C-10. Ratio of the integrated Bremsstrahlung emission transmitted through foils of the designated material to the total incident flux vs. foil thickness, D, for various temperatures.

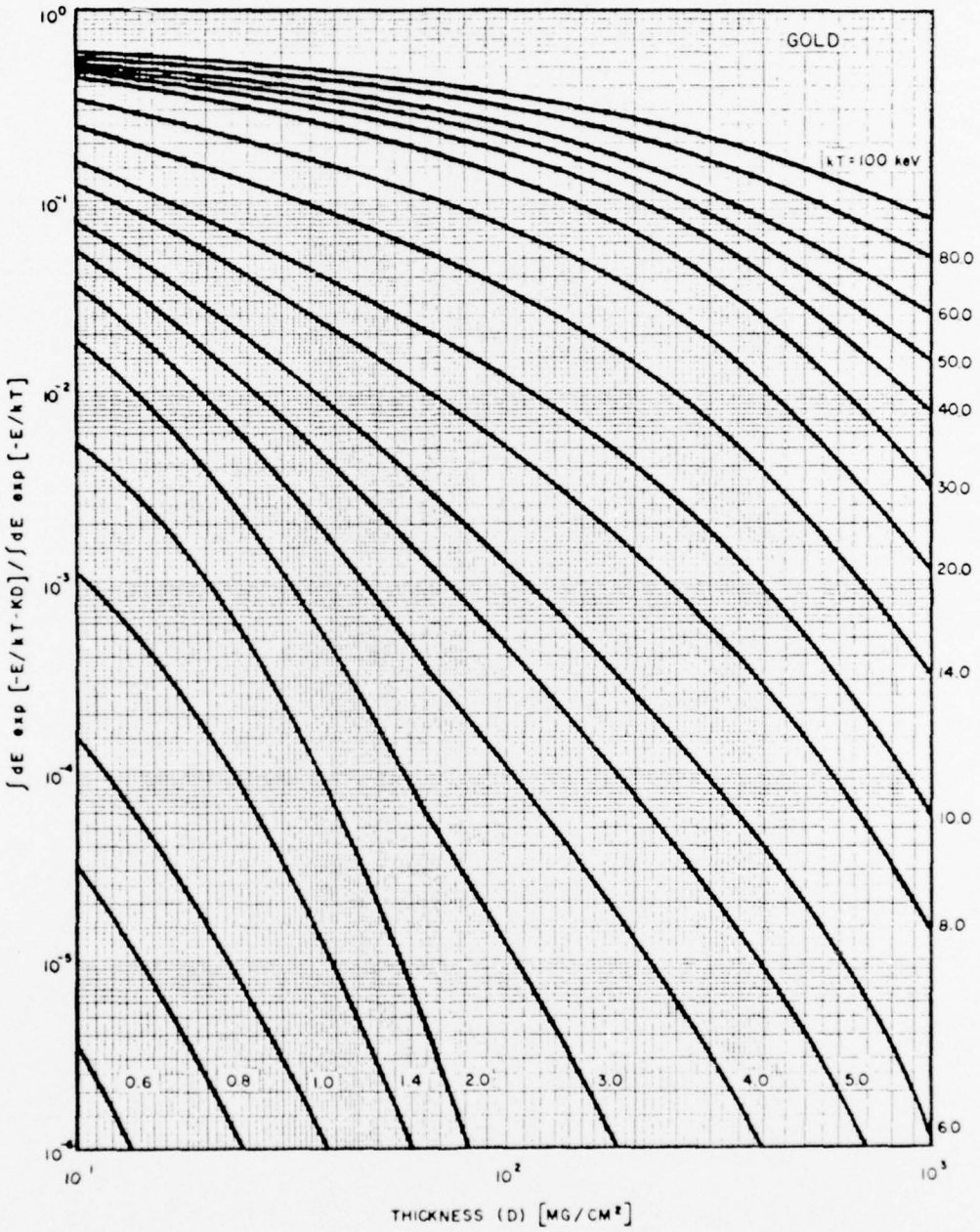

Fig. C-11. Ratio of the integrated Bremsstrahlung emission transmitted through foils of the designated material to the total incident flux vs. foil thickness, D, for various temperatures.

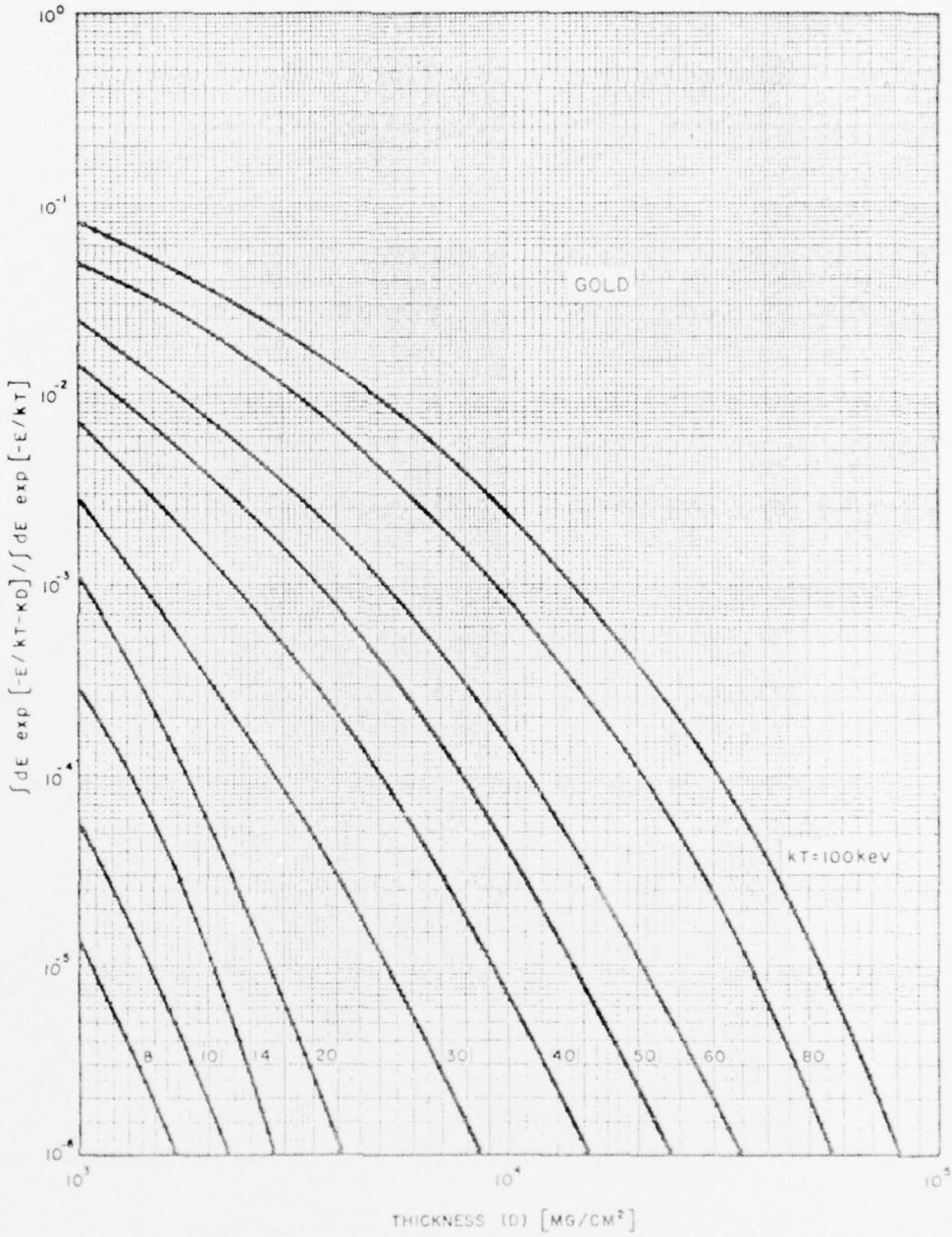

Fig. C-12. Ratio of the integrated Bremsstrahlung emission transmitted through foils of the designated material to the total incident flux vs. foil thickness, D, for various temperatures.

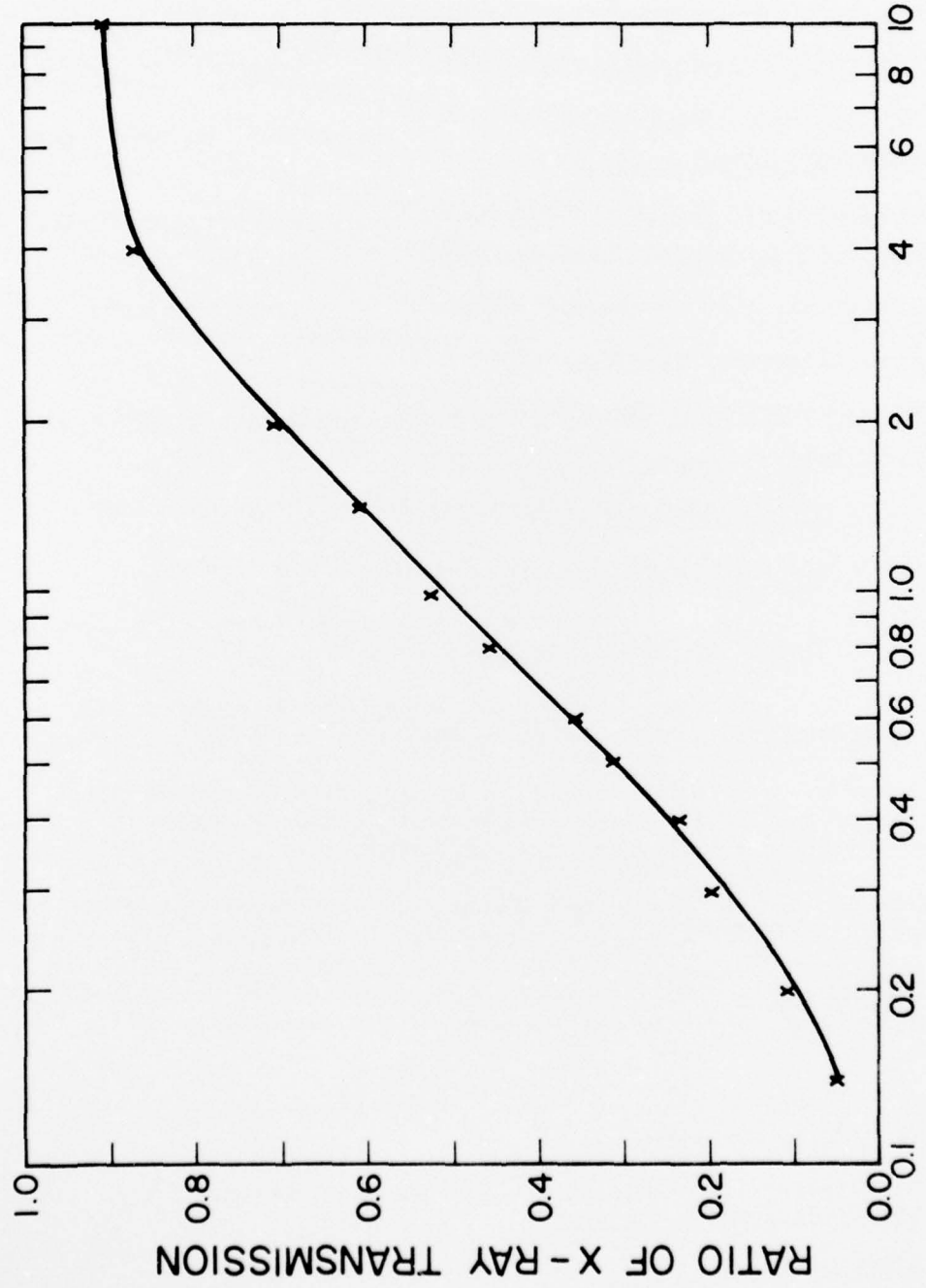

Fig. C-13. The ratio of X-ray transmissions through beryllium filters of 24 mg/cm^2 and 9.6 mg/cm^2 vs. electron temperature.

REFERENCES

[1] J. W. Mather, Phys. Fluids Suppl. 7, 5-28 (1964).

[2] J. W. Mather, Phys. Fluids 8, 366 (1965).

[3] P. P. Petro, N. V. Filippov, T. I. Filippova, and V. A. Khrabrov, in Plasma Physics and the Problems of Controlled Thermonuclear Reactions, M. A. Leontovich, ed. (Pergamon Press, New York, 1960), Vol. 1V, p. 198.

[4] N. V. Filippov, T. I. Filippova, and V. P. Vinogradov, Nuclear Fusion Suppiement Part 2, 577 (1962).

[5] D. J. Nagel, "X-ray Emission from High Temperature Laboratory Plasmas," Advances in X-Ray Analysis (Plenum Press, New York, 1971), Vol. 18.

[6] O. Zucker et al., "The Design of a Repetitively Pulsed Megajoule Dense-Plasma Focus," Lawrence Radiation Laboratory Report UCRL-51872, Livermore, California, (August, 1975).

[7] B. J. Eastlund and W. C. Gough, USAEC Report No. WASH-1132, (1969) (unpublished).

[8] D. J. Rose, Culham Laboratory Memorandum No. 82, (1968) (unpublished).

[9] L. Spitzer et al., USAEC Report NYO-6047, (1954) (unpublished).

[10] S. L. Gralnick, Report No. 58, Plasma Laboratory, School of Engineering and Applied Science, Columbia University, New York, (1973).

[11] J. W. Mather, in Methods of Experimental Physics, H. A. Griem and R. H. Loveberg, eds. (Academic Press, New York, 1970), Vol. 9, Part A.

[12] N. J. Peacock, M. G. Hobby, and P. D. Morgan, Proc. Fourth Conf. Plasma Physics and Controlled Nuclear Fusion Research, Madison CN-28/D-5 (International Atomic Energy Agency, Vienna, 1972).

[13] M. Rosenbluth and R. Garwin, Los Alamos Sci. Lab. Report LA-1850, Loa Alamos Scientific Lab., Los Alamos, New Mexico, (1954).

[14] N. V. Filippov and T. I. Filippova, Plasma Physics and Controlled Nuclear Fusion Research Conference Proceedings, (1965) (IAEA, 1966), Vol. 2.

[15] H. L. L. van Paassen and R. H. Vandre, Phys. Fluids 13, No. 10 (October 1970).

[16] M. J. Bernstein, C. M. Lee and F. Hai, Phys. Rev. Letters 27, No. 13, (September 1971).

[17] E. H. Beckner, J. Appl. Phys. 37, No. 13 (December 1966).

[18] M. J. Bernstein, Phys. Fluids 13, No. 11 (November 1970).

[19] D. E. Potter, Phys. Fluids 14, No. 9 (September 1971).

[20] S. P. Gary and F. Hohl, Phys. Fluids 16, No. 7 (July 1973).

[21] R. S. Post and T. C. Marshall, Phys. Fluids 17, No. 2 (February 1974).

[22] G. Lehner and F. Pohl, Z. Physik 207, 83 (1967).

[23] D. J. Johnson, J. Appl. Phys. 45, No. 3 (March 1974).

[24] D. J. Rose and M. Clark, Plasma and Controlled Fusion (M.I.T. Press, Cambridge, Massachusetts, 1965).

[25] V. S. Imshennik, Nuclear Fusion 13, 929 (1973).

[26] D. C. Gates et al., "Development of a Fusion Neutron Generator," Aerojet-General Nucleonics Report AN1448,(August 1965).

[27] A. H. Compton and S. K. Allison, X-Rays in Theory and Experiment (D. Van Nostrand Company, Inc., New York, 1936).

[28] J. W. Mather et al., "Recent Studies of Dense Plasma Focus," Plasma Physics and Controlled Nuclear Fusion Research (1971), Vol. 1.

[29] D. L. Webster, Phys. Rev. 9, 220 (1917).

[30] E. Wagner and H. Kulenkampff, Z. Physik 23, 503 (1922).

[31] C. A. Foster, Ph.D. thesis, University of Illinois, Urbana, Illinois (to be published).

[32] W. C. Nunnally, M. Kristiansen, and M. O. Hagler, Appl. Phys. Letters 26, No. 9 (1975).

[33] R. A. Gross and B. Miller, "Plasma Heating by Strong Shock Waves," Methods of Experimental Physics (Academic Press, New York, 1970), Vol. 9, Part A.

[34] A. S. Denholm et al., "Review of Dielectrics and Switching," Technical Report No. AFWL-TR-72-88, Energy Sciences, Inc. (February 1973).

[35] S. A. Smirnov, L. A. Makhenko, and A. M. Shendrovich, Instruments and Experimental Techniques, 503-506 (translation)(May-June 1961).

[36] P. I. Shkuropat, Sov. Phys. - Tech. Phys. 11, 779-783 (December 1966).

[37] J. M. Taylor, Semiconductor Particle Detectors (Butterworth Inc., Washington, D.C., 1963).

[38] G. Dearnaley and D. C. Northrop, Semiconductor Counters for Nuclear Radiations (John Wiley & Sons, Inc., New York, 1966).

[39] S. Glasstone and R. H. Lovberg, Controlled Thermonuclear Reactors (D. Van Nostrand Company, Inc., New York, 1960).

[40] R. C. Elton, "Determination of Electron Temperatures Between 50 eV and 100 keV From X-Ray Continuum Radiation in Plasmas," Naval Research Lab. Report 6738, Washington, D.C. (December 1968).

[41] "Laser Program Annual Report - 1974," UCRL-50021-74, prepared by Lawrence Livermore Laboratory, Livermore, California (1974).